UCL Université catholique de Louvain

École polytechnique de Louvain (EPL)

Evaluation of preosteoblast behavior on biomimetic intersected nanotube frameworks for tissue engineering applications

Dissertation presented by
Juliette LOUVEGNY , Mathieu NAUDIN

for obtaining the Master's degree in
Biomedical Engineering

Supervisor(s)
Sophie DEMOUSTIER, Christine DUPONT

Reader(s)
Damien LEFÈVRE, Greet KERCKHOFS , Bernard KNOOPS

Academic year 2017-2018

Abstract

Extensive research in the past few decades has shed light on the role of the extracellular matrix (ECM) in the control of cell functions. By providing a complex combination of physical, chemical and nanotopographical cues to the cells, the ECM influences cell behaviors, such as adhesion, growth or differentiation. These findings have paved the way for the elaboration of new tissue engineering scaffolds and biointerfaces mimicking the ECM by presenting similar cues.

In this context, this master thesis focuses on the response of mouse MC3T3-E1 preosteoblastic cells seeded on nanostructured biointerfaces mimicking the bone ECM. The studied biointerfaces are self-standing hard-templated frameworks, made of intersected rigid polypyrrole nanotubes and functionalized with a biomimetic multilayer coating of collagen (COL) and hyaluronan (HA) through Layer-by-Layer assembly. The nanotubular polypyrrole framework imitates the porous and nanofibrous structure of the bone native ECM and provides mechanical strength while the biomimetic coating, made of constituents present in bone native ECM, offers biomolecular cues to the cells. The elaboration process and the material characterization of the biointerfaces had already been completed in previous research works. The objective of this study was, therefore, to test cell behavior on the designed biointerfaces. The specific effects of the nanostructure and biomimetic (HA/COL)-coating of the biointerfaces were investigated by studying the response of MC3T3-E1 cells on both coated and non-coated polypyrrole nanotube frameworks. Cell adhesion and proliferation after 24 hours of culture on the biointerfaces were assessed by a fluorometric DNA quantification assay and epifluorescence microscopy. The ability to induce osteoblastic differentiation was evaluated after 7, 14 and 21 days, by colorimetric quantification of alkaline phosphatase activity, an early marker of osteoblastic differentiation.

24-h adhesion and proliferation results showed that the polypyrrole nanotube frameworks, both bare and coated, enhanced cell adhesion compared to bare glass substrates. The polypyrrole nanotube frameworks also promoted cell spreading and filopodia formation. The diameter of the polypyrrole nanotubes was found to influence cell adhesion, as frameworks of smaller diameter displayed increased cell attachment. In the absence of fetal bovine serum (FBS), the effect of the biomimetic (HA/COL)-coating was found to depend on the nanostructure of the underlying substrate. It enhanced cell adhesion on coated frameworks of larger diameter nanotubes but slightly attenuated it on frameworks of smaller diameter nanotubes. In the presence of FBS, the effect of the biomimetic coating was masked by the adsorption of a mixture of proteins naturally present in the serum. Osteoblastic differentiation was found to be significantly enhanced on both bare and coated biointerfaces, respectively only after 21 days and after both 14 and 21 days, compared to bare and coated glass substrates.

This study provides a first evaluation of the adhesion, proliferation and differentiation of preosteoblastic cells on newly developed ECM-like biointerfaces. The results reveal the promising potential of such biointerfaces for the control of osteoblastic differentiation. The developed biointerfaces offer a platform for the delivery of signals to cells, with potential applications in cell biology, biomaterials science and tissue engineering.

Acknowledgement

First, we would like to thank both our surpervisors, Professor Sophie Demoustier and Professor Christine Dupont, for their availability, guidance and advice throughout this master thesis.

We are also very grateful to Damien Lefèvre for his availability, day-to-day support and all the time he spent advising us from the beginning to the end of this project.

Next, we would like to thank all the members of the BSMA lab for their kindness and their help when needed. In particular, the chocolates from Saint-Nicolas and the Easter Bunny were much appreciated.

We also extend our sincere thanks to all members of the ISV lab for cell culture for kindly welcoming us in their lab and for their assistance when needed.

Then, we would like to thank Professor Michel Ghislain for our instructive discussion about the alkaline phosphatase.

Finally, thank you to the two other students who were working on their master theses in the BSMA lab, Coraline Henrion and Eve Verpoorten. Sharing our different successes and failures was an efficient and enjoyable way to get support when needed and to go through the year in a cheerful atmosphere.

List of abbreviations

α-MEM	Alpha modified minimum essential medium
AAO	Anodic aluminum oxide
ALG	Alginic acid
ALP	Alkaline phosphatase
AS	Above saturation limit
ATP	Adenosine triphosphate
BD	Below limit of detection
BGP	Bone ψ-carboxyglutamic acid-containing protein
BMSC	Bone marrow stromal cell
BSP	Bone sialoprotein
CHI	Chitosan
CLB	Cell lysis buffer
COL	Collagen
CS	Chondroitin sulfate
DAPI	4′,6-diamidino-2-phenylindole
DPBS	Dulbecco's phosphate buffered saline
ECM	Extracellular matrix
EDC	1-Ethyl-3-(3-dimethylaminopropyl)carbodiimide
EDTA	Ethylenediaminetetraacetic acid
ES	Electrical stimulation
FBS	Fetal bovine serum
GEL	Gelatine

HA	Hyaluronan/hyaluronic acid
HEP	Heparin
HMDS	Hexamethyldisilazane
LB	Langmuir-Blodgett
LbL	Layer-by-Layer
MES	2-(N-morpholino)ethanesulfonic acid monohydrate
NGF	Nerve growth factor
NW	Nanowire
NWN	Nanowire network
OCN	Osteocalcin
OPN	Osteopontin
Osf2	Osteoblast specific factor 2
p-NPP	p-nitrophenylphosphate
PAH	Poly(allylamine hydrochloride)
PBS	Phosphate buffered saline
PC	Polycarbonate
PEG	Poly(ethylene glycol)
PEI	Poly(ethylenimine)
pen/strep	Penicillin streptomycin
PGA	Poly(L-glutamic acid)
PLA	Poly(lactic acid)
PLL	Poly(L-lysine)
PLLA	Poly(L-lactic acid)
PPy	Polypyrrole
PS	Polystyrene
PSS	Poly(styrene sulfonate)
PTH	Parathyroid hormone

PTHrP	Parathyroid hormone-related protein
Py	Pyrrole
RT-PCR	Reverse transcription polymerase chain reaction
SAMs	Self-assembled monolayers
SE	Standard error of the mean
SEM	Scanning electron microscopy
sulfo-NHS	N-hydroxysulfosuccinimide
TCP	Tissue culture polystyrene
TGF-β1	Transforming growth factor-β1

Contents

Abstract i

Acknowledgement ii

List of abbreviations iii

Introduction 1

1 Literature Review 4
- 1.1 Nanofabrication techniques . . . 4
  - 1.1.1 Hard templating . . . 4
  - 1.1.2 Layer-by-Layer (LbL) assembly . . . 9
- 1.2 Mouse MC3T3-E1 cell line as an osteoblastic model . . . 13
  - 1.2.1 Description . . . 13
  - 1.2.2 Proliferation and differentiation . . . 14
  - 1.2.3 Other markers for osteoblastic differentiation . . . 15
  - 1.2.4 Main assays for osteoblastic differentiation markers . . . 17
- 1.3 Major cell-instructive cues . . . 17
  - 1.3.1 Cellular interactions with polypyrrole . . . 17
  - 1.3.2 Effect of nanotopography on cellular behavior . . . 22
  - 1.3.3 ECM surface coatings to control cellular functions . . . 28

2 Materials and Methods 36
- 2.1 Elaboration of the PPy nanotube frameworks . . . 36
  - 2.1.1 Materials . . . 36
  - 2.1.2 Template synthesis of the nanotube frameworks . . . 37
  - 2.1.3 Template removal . . . 38
- 2.2 LbL assembly of the (HA/COL)-coatings . . . 38
  - 2.2.1 Materials . . . 38
  - 2.2.2 LbL deposition procedure . . . 39
  - 2.2.3 Chemical crosslinking . . . 39
- 2.3 Cell culture . . . 40
- 2.4 Cell adhesion and proliferation tests . . . 40
  - 2.4.1 Experimental plan . . . 40
  - 2.4.2 Cell seeding . . . 41
  - 2.4.3 DNA quantification assay . . . 42
  - 2.4.4 Epifluorescence microscopy . . . 43
  - 2.4.5 Scanning Electron Microscopy . . . 44
- 2.5 Cell differentiation tests . . . 45
  - 2.5.1 ALP assay on uncoated PPy nanotube frameworks . . . 45
  - 2.5.2 ALP assay on (HA/COL)-coated PPy nanotube frameworks . . . 48

3 Results and Discussion **50**
3.1 Cell adhesion and proliferation 50
3.1.1 DNA quantification 50
3.1.2 Qualitative evaluation of cell adhesion 53
3.1.3 Cell morphology 58
3.1.4 Cell interactions with the PPy nanotube frameworks 61
3.1.5 Summary and discussion of the cell adhesion tests 67
3.2 Cell differentiation 68
3.2.1 Non-coated PPy frameworks 69
3.2.2 (HA/COL)-coated PPy frameworks 74
3.2.3 Summary and discussion of the cell differentiation tests 78
3.3 Summary of the cellular tests 80

Conclusion and Perspectives **82**

Bibliography **84**

A Complementary information on the cell adhesion and proliferation tests **91**
A.1 Calibration curves of the DNA quantification assay 91
A.2 Detailed results of DNA quantification assay 92
A.3 SEM image artifacts 93
A.3.1 Non coated PPy 40 nm 93
A.3.2 Coated PPy 40 nm 94

B Complementary information on the cell differentiation tests **96**
B.1 Non-coated PPy frameworks 96
B.1.1 Calibration curve for the DNA quantification 96
B.1.2 Information about the calibration curves for the intracellular ALP quantification 96

Introduction

General context

Tissue and organ regeneration is nowadays an important field of study in biomedicine. Loss of organ or tissue arising from traumatic injury or disease can have serious consequences on the health and well-being of the patient. Unfortunately, millions of patients are affected every year [1]. Traditional therapy consists in replacing the damaged or missing tissues by means of an allograft (from a donor) or, when possible, an autograft (from the patient himself). Despite being still the most effective therapeutic approach, grafts present significant drawbacks, such as problems of immunocompatibility, donor shortage or complications at the donor site resulting from the extraction of the graft [1]. To circumvent those drawbacks, extensive research has been carried out in the past thirty years to propose tissue engineering approaches to regenerate the missing or damaged tissues.

Tissue engineering aims at reconstructing the damaged tissues by means of specifically designed three-dimensional scaffolds. To do this, two main approaches can be considered. The first approach consists in seeding stem cells *in vitro* on a scaffold designed such as to promote cell growth and differentiation to form the desired tissue (bone, cartilage, muscle, neural, etc.). The newly-formed tissue can then be implanted to replace the damaged or failed tissue [2]. The second approach consists in implanting the scaffold at the site of the damage in order to directly recruit cells from the body of the patient [2]. The scaffold then acts as a promoter and guide for the regeneration of the damaged tissue *in situ*.

Whether for *in situ* or *in vitro* approach, scaffolds provide the structural basis needed for the formation of the tissue by ensuring mechanical support to the cells. Moreover, chemical and physical signals present at the cell-scaffold interface can be used to trigger certain cell behaviors such as adhesion, proliferation, differentiation and function. Such cues can be of different nature [3, 4]. For instance, in addition to the chemical nature of the biointerface, nano and/or microstructured topography have been shown to significantly influence cell behavior [5]. Finally, bioactive molecules can also be added, such as proteins, growth factors or drugs for instance [4]. The objective and challenge in tissue engineering strategies is to combine those cues such as to induce the desired cell behavior.

To achieve this, the main trend in tissue engineering current research focuses on the imitation of the cells' natural 3D microenvironment, i.e. the extracellular matrix (ECM). This arises from extensive research carried out in the last few decades which has shed light on the influence of the ECM on cellular functions such as adhesion, growth, mobility and differentiation [6]. *In vivo*, the extracellular matrix serves as a natural scaffold for the cells. Not only does it provide the cells with anchorage defining the architecture of the tissue, but it also ensures sufficient mechanical strength for the tissue to withstand *in vivo* loads [4]. Most importantly, the ECM provides a complex combination of cues that can trigger specific cell behaviors [7]. Even if a complete understanding of the cell's complex microenvironment *in vivo* is still lacking,

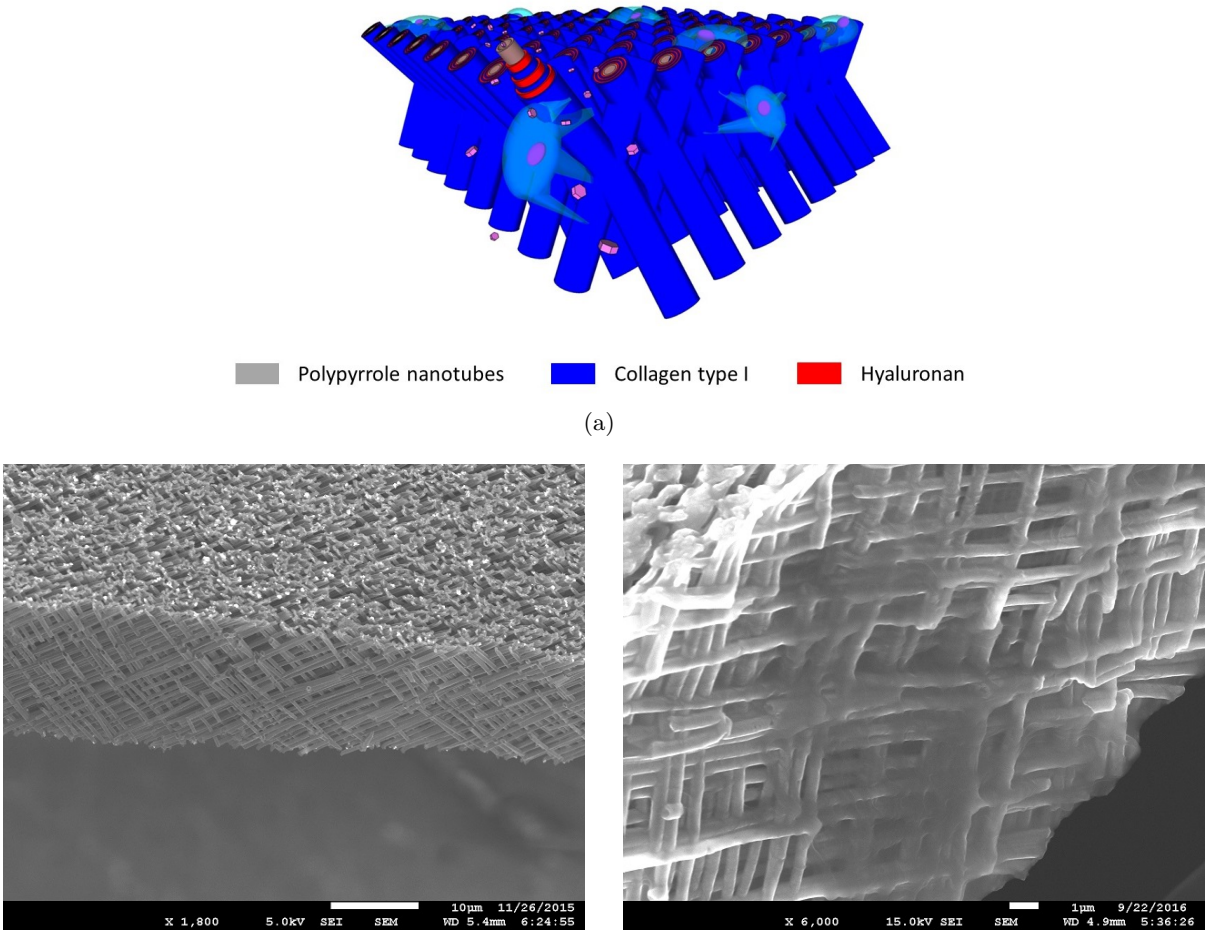
researchers have been able to delineate three main types of information from the ECM that impact cell behavior [6, 7]. First, the ECM communicates with the seeded cells via physical signals such as mechanical cues [6]. Then, the cells also receive specific chemical signals from the ECM-components or entrapped bioactive molecules [6]. Finally, the nanostructure and nanotopography of the ECM itself have also proven to play a significant role in the cellular response [6].

These findings have paved the way for the elaboration of tissue engineering scaffolds mimicking the ECM by providing similar physical, chemical and nanotopographical cues. Natural scaffolds can consist of decellularized tissues, obtained by removing cells and antigens from the extracellular matrix [7]. They present the advantage of preserving the native architecture of the tissue [7]. In addition, such scaffolds also retain some of the proteins, cell adhesion ligands and other bioactive molecules naturally present in the ECM [7]. However, decellularization processes still yield variable results and standard decellularization processes are, therefore, still lacking [8]. Alternatively, scaffolds mimicking the nanostructure of the ECM can be made from natural or synthetic materials using various nanofabrication techniques. Among them, electrospinning is a popular approach to produce submicron polymer fiber mesh and to imitate, therefore, the structure adopted by the fibrous proteins of the ECM [9]. Self-assembly of natural ECM molecules is also possible to obtain a nanofibers network [9]. For synthetic scaffolds, template synthesis has also proven to be a versatile and reliable method to produce nanostructured surfaces [10].

Biointerfaces made from modified and/or structured biological molecules such as collagen or other natural polymers, present the advantage of a good biocompatibility and enhanced cellular interactions [6, 8]. Nonetheless, they can raise issues in terms of mechanical strength because biopolymers are known for having weak mechanical strength [3]. In addition, their properties are not easily adjusted and controlled [3]. In contrast, synthetic materials (polymers, ceramics, etc.) present the advantage that their structure and properties can be controlled more precisely [9]. However, they can be problematic in terms of biocompatibility and they lack the biochemical cues guiding cells fate [8]. For this reason, hybrid scaffolds, combining the biocompatibility and the bioactivity of natural macromolecules with the tunability and the mechanical strength of synthetic materials, are being more and more investigated [8]. Such composite biointerfaces are generally composed of a synthetic material whose surface is modified to be rendered bioactive. This can be achieved either by coating the surface with ECM-components or by covalently linking ECM moieties onto the surface [3]. The synthetic material controls the main structure while the biologically-modified surface improves cell-interaction [9].

Objective of the master thesis

This master thesis is part of the Ph.D. thesis of Damien Lefèvre aiming at developing biointerfaces mimicking the ECM for tissue engineering and regenerative medicine applications. The studied biointerfaces are made from both synthetic and organic materials. A schematic of the biointerfaces is presented in Figure 1(a). Imitation of the porous and fibrous structure of the ECM is achieved by an architecture consisting in a framework of intersected polypyrrole (PPy) nanotubes. The purpose of this core architecture of PPy is also to provide mechanical strength to the biointerface. Polypyrrole nanotubes are then coated with collagen I (COL) and hyaluronan (HA), two major components of natural ECMs, using Layer-by-Layer (LbL) assembly. The objective is to reproduce partially the complex chemical environment of natural ECMs. Scanning electron micrographs of a non-coated and a coated PPy nanotube framework elaborated by Damien Lefèvre are shown in Figures 1(b) and (c) respectively.



(a) (b) (c)

Figure 1: (a) Schematic of the studied ECM-like biointerfaces. The biointerfaces are made of a rigid core composed of a self-standing PPy nanotube framework coated with hyaluronan and collagen type I by LbL assembly. Reproduced from Damien Lefèvre (Powerpoint presentation, 2017). (b) SEM image of a non-coated PPy nanotube framework of 300 nm nanotube diameter. Reproduced from Damien Lefèvre (2016). (c) SEM image of a PPy nanotube framework of 300 nm nanotube diameter coated with 6 (HA/COL)-bilayers. Reproduced from Damien Lefèvre (2016).

In the frame of this larger research project, material characterization of the biointerfaces had already been completed by Damien Lefèvre. Therefore, this master thesis will focus on cellular testing of the biointerfaces, using mouse MC3T3-E1 preosteoblastic cells. Adhesion and proliferation tests will first be performed to evaluate cell attachment on the biointerfaces. Most importantly, differentiation tests will be carried out to assess the ability of the biointerfaces to induce the differentiation of the preosteoblastic cells into mature bone cells. To this aim, the effect of topographical parameters such as the intersected architecture and nanotube diameter on cell attachment and differentiation will be investigated. In addition, the influence of the hyaluronic acid-collagen coating will also be studied.

The present dissertation details the results of this study. First, a review of the literature will be presented in order to give insight both into the nanofabrication techniques used to elaborate the biointerfaces and on the main cues known to influence cellular functions. Then, the materials and methods used in the frame of this study to produce the biointerfaces will be described. The cellular adhesion and differentiation tests performed to characterize the cellular response will also be detailed. The last chapter will be dedicated to the presentation and discussion of the obtained results. Finally, this dissertation will be concluded by a presentation of the main conclusions of this study and of future perspectives for the studied ECM-like biointerfaces.

Chapter 1

Literature Review

In this chapter, the techniques used for the fabrication of the coated PPy nanotube framework, i.e. hard templating and Layer-by-Layer assembly, will be briefly described. Next, the focus will be put on the cellular aspects, which are the main objectives of this thesis. This will be done first by providing background information about the mouse MC3T3-E1 cell line that will be used for the adhesion and differentiation tests. Then, the cell-scaffold interactions will be discussed more extensively by providing a detailed review of the impact of PPy, nanotopography and biomimetic coatings on cellular functions.

1.1 Nanofabrication techniques

As already mentioned in the Introduction, many techniques have been investigated to reproduce the porous and nanofibrillar architecture of native ECM using synthetic materials. Among them, templating has emerged as a convenient and simple method to produce nanotubes [10]. Regarding the biofunctionalization of the scaffold surface, Layer-by-Layer assembly has proven to be a reliable approach to produce biomimetic coatings [11, 12]. In this section, these two techniques used to produce the studied biointerfaces will be briefly reviewed.

1.1.1 Hard templating

First introduced in the 1990s by C.R. Martin, hard templating allows the fabrication of a wide variety of nanomaterials, from 1D nano-items, such as nanotubes or nanorods to two- or three-dimensional nanostructures [10, 13, 14]. It relies on the use of a guide, called the template, to direct the synthesis of the target material [13]. Hard templating is more and more appreciated in nanofabrication for its simplicity, versatility and good control of the obtained nanostructure [10,13]. This method is also general since it has been used successfully on metals, semiconductors and conductive polymers [10]. Therefore, possible applications for this nanofabrication technique are very diversified, going from electronics to biomedical applications such as drug delivery or tissue engineering. In this section, the general principle of hard templating will be reviewed, with an emphasis on the synthesis of nanotubes using nanoporous templates.

1.1.1.1 Principle

One of the main advantages of hard template synthesis is the simplicity of its principle. A rigid nanostructured material, called the template, is used as a guide for the synthesis of nanomaterials, such as nanorods or nanowires [13]. The structure of the template thus dictates the structure of the obtained nanomaterials, allowing a precise control over their morphology [14].

Figure 1.1 illustrates the general principle of the hard templating process. It shows a particular application of hard templating for nanowires synthesis. However, the three steps represented are

generally common to any particular template-synthesis strategy [13]. Overall, the entire process is carried out as follows:

- **Template selection and preparation**
  The first step consists in preparing a template with the appropriate features to synthesize nanomaterials with the desired morphology [13]. In theory, any material with nanostructured features, from nanoporous membranes to colloidal particles, can serve as template [13]. However, the chosen template must meet certain requirements. It must be compatible with the processing conditions and allow wetting of the material that will be deposited [15]. As represented in Figure 1.1, the synthesis of nanotubes or nanowires requires the use of a nanoporous template with cylindrical pores [10, 15]. The use of nanoporous templates is reviewed in more details in the section 1.1.1.2.

- **Template filling**
  The next step after template preparation is the synthesis of the target material in the template [13]. Depending on the target material, several methods to fill the template can be implemented. For instance, conductive nanowires can be synthesized by electrochemical deposition in the pores of a nanoporous template placed on a metal electrode [15]. Other deposition methods include namely, electrophoretic deposition of ceramic and organoceramic materials from a colloidal dispersion or Layer-by-Layer deposition in a porous template to make multi-layered nanotubes [15]. Regarding porous templates, however, the most straightforward approach consists in filling the nanopores directly with a precursor solution [15]. This approach is described in more details in the section 1.1.1.3.

- **Template removal**
  At the end of the template-directed synthesis, the newly formed nanomaterials are still trapped in the template. The last step of the process is, therefore, the removal of the template to free the synthesized nanomaterials [13]. This is most often achieved by a simple dissolution of the template [13]. Other chemical methods, such as etching or calcination can also be used [13]. The chosen method must, however, preserve as much as possible the integrity of the synthesized nanomaterials [13]. Also, the ease of removal is an important parameter to take into account when selecting the template at the start of the process [15].

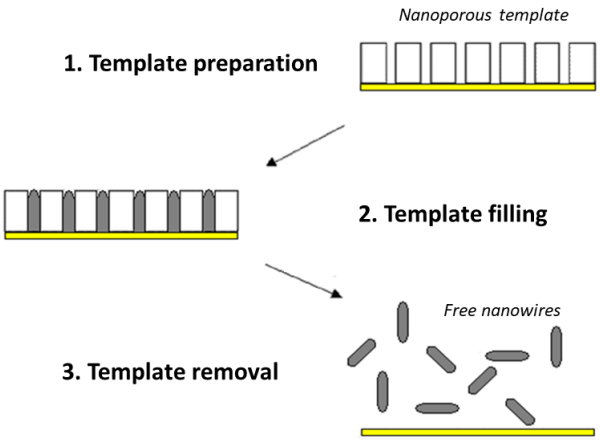


Figure 1.1: Schematic of the templating principle applied to the preparation of free nanowires using a porous template. Adapted from Sisman (2011) [16].

1.1.1.2 Nanoporous templates

As already mentioned in the previous section, the elaboration of 1D nano-objects (nanowires, nanorods or nanotubes) is achieved by using templates presenting cylindrical pores. The two

most common kinds of nanoporous templates used for this purpose are anodic aluminum oxide membranes (AAO) and track-etched polycarbonate (PC) membranes [15]. Both types are nowadays commercially available [13]. Each has its own advantages and disadvantages.

- **Anodic aluminum oxide membranes (AAO)**
  AAO porous membranes (Fig. 1.2) are produced by anodic oxidation of aluminum sheets in sulfuric, oxalic or phosphoric acid [15]. The advantage of AAO templates is that the pores can be arranged regularly along a hexagonal array, thus allowing a uniform pore distribution [15]. In addition, high pore densities (up to $\sim 10^{11}$ pores/cm^2) can be achieved. and pore diameter can be as small as 5 nm [10, 15]. Nonetheless, only a limited range of pore diameters are available commercially [10]. AAO templates also present a high rigidity, which helps preserving the integrity of the grown nanorods [15]. However, their dissolution requires harsh conditions in terms of pH which are not compatible with soft materials [13, 15].

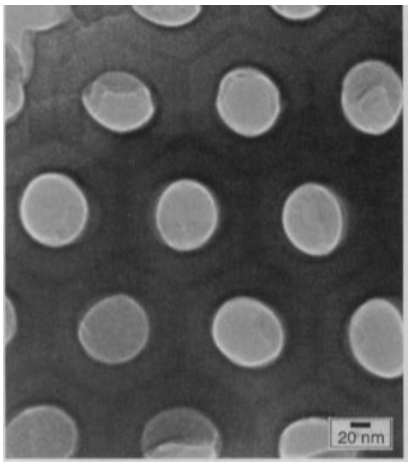


Figure 1.2: TEM image of a microtomed section of a AAO membrane with pores of 70 nm diameter. Reproduced from C.R. Martin (1994) [10].

- **Polycarbonate (PC) track-etched membranes**
  PC nanoporous membranes (Fig. 1.3) are prepared using the track-etching technique. Nanopores are obtained by bombarding a PC film, usually 6 to 20 μm thick, with accelerated energetic heavy ions [17]. Along their way, those ions damage chemical bonds, thus creating linear damaged tracks in the polymer [17]. The damaged tracks are then subsequently chemically etched to make the nanopores [17]. Unlike AAO templates, track-etched membranes have randomly distributed pores, with a maximum density of $\sim 10^9$ pores/cm^2 [15]. Nonetheless, good control of the pore dimensions can be achieved. Indeed, the nanopores formed by this technology are of uniform diameter, ranging from 10 nm to 100 μm [15]. Track-etched membranes with customizable pore dimensions are available commercially. Moreover, PC membranes are also easier to handle than AAO membranes [15]. Template removal is also easier as it can be achieved by pyrolysis or by dissolution with organic solvents such as dichloromethane [15, 18].

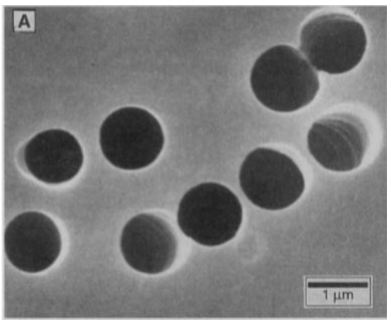


Figure 1.3: SEM image of a PC track-etched membrane with pores of 1 μm diameter. Reproduced from C.R. Martin (1994) [10].

In addition, to 1D nanowires and nanotubes, nanoporous templates can also be used to produce freestanding nanowires networks. Nanowires networks (NWNs) are three-dimensional structures made of a large number of interconnected nanowires [19]. These 3D constructs have been widely investigated by researchers for the past few years, as they integrate in a controlled

and structured manner nanoscale elements in a piece of macroscopic size [19]. Thus, NWNs present the specific properties of nanowires while presenting a large area at the macroscopic scale (up to several cm^2), which facilitates their manipulation and use in a specific application [20].

A promising approach for the synthesis of NWNs is based on track-etched polymer membranes. Figure 1.4 shows the steps for the preparation of NWNs using this type of membrane. Track-etched membranes with intersected nanopores are prepared by irradiating the polymer film several times, each time with a different incident angle for the ion beam [21, 22]. Therefore, the damaged tracks produced by the successive irradiations cross each other at a controlled angle [21]. After chemical etching, a template with intersected nanopores is thus obtained.

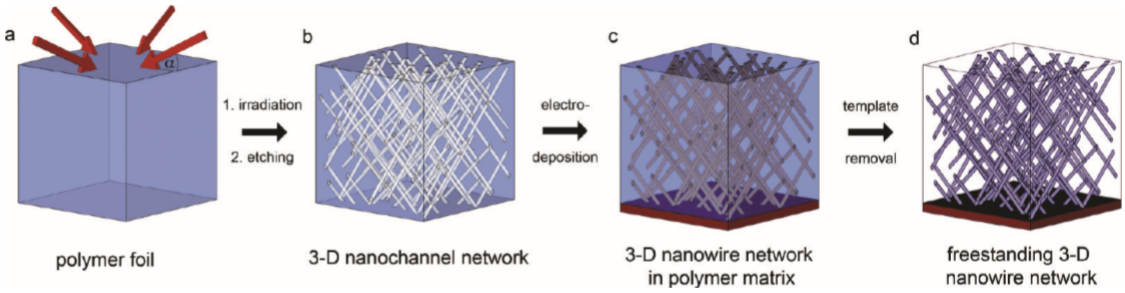


Figure 1.4: Schematic of the preparation of nanowires networks using a track-etched membrane as template. a) Successive irradiations with ion beams of different incident angles α, to create intersected damaged tracks. The damaged tracks are then selectively chemically etched. b) A template with a 3D-porous network is obtained. c) Nanowires are grown in the pores of the template by electrodeposition. d) Template removal to free the nanowires network. Reproduced from Rauber et al. (2011) [21].

Rauber et al. successfully used the PC track-etched templates with intersected pores to make freestanding platinum NWNs by electrodeposition (Fig. 1.4) [21]. Such templates can also be filled with electroless deposition techniques, such as solution filling for example [21]. With this process, networks of several square centimeters with a height up to 60 μm can be achieved. The smallest possible diameter for the nanotubes is of about 10 nm [21]. However, below 35nm, the interconnected nanowires cannot maintain the exact structure imposed by the template and bend upon template removal [21]. Using a similar approach, Piraux and coworkers synthesized mechanically stable and self-standing 3D PPy NWNs by electrochemical polymerization (Fig. 1.5) [22]. The advantage of the track-etched approach is that it allows independent control of the size, shape, composition, interconnectivity and orientation of the nanowires in the network [21]. Complex branching architecture can also be achieved by adjusting the number of irradiations and their orientation [21].

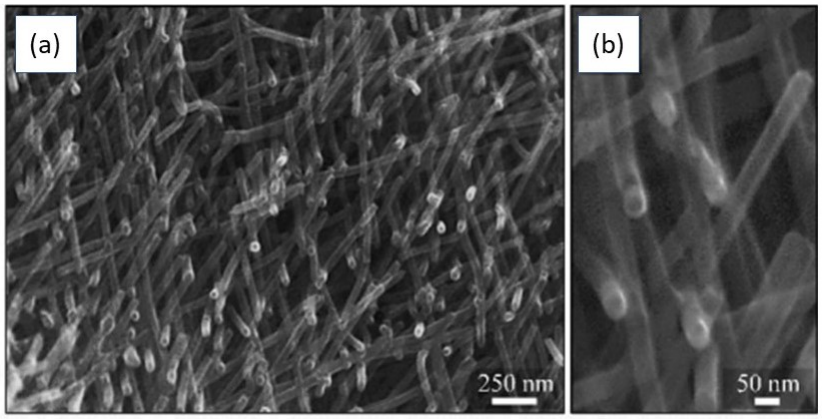


Figure 1.5: SEM images of a 3D PPy nanowire network, synthesized using PC track-etched templates with intersected cylindrical pores of 40 nm mean diameter. Reproduced from Piraux et al. (2016) [22].

1.1.1.3 Solution filling

To make nanowires or nanotubes by template synthesis, the most straightforward method is to fill directly the nanopores either with a precursor solution or with a melt of the target material [15]. However, compared to other techniques such as electrodeposition, complete filling of the pores is difficult to ensure [15]. Moreover, depending on the adhesion of the filling material on the pore walls, filled nanowires or hollow nanotubes are formed. Indeed, if the filling material only weakly adheres to the pore walls, the material starts to form at the center of the pores and, therefore, filled nanowires are obtained [15]. On the other hand, if the filling material has a strong affinity for the pore walls, solidification starts at the walls and continues towards the center. In that case, hollow nanotubes are formed [15].

Despite being less easily controlled than other deposition methods, solution filling has proven to be an effective and easy method to produce nanotubes and nanowires of conductive polymers such as polypyrrole or polyaniline [10,18]. In these cases, the pores are first filled with a monomer solution. Then, an oxidizing agent is added to initiate oxidative polymerization *in situ* [15].

C.R. Martin and coworkers chemically synthesized nanotubes of polyaniline, poly(3-methylthiophene) and polypyrrole by immersing PC track-etched membranes in a solution of the monomer and its corresponding oxidizing agent [10]. They discovered that nucleation and growth of the polymer occur preferentially on the pore walls of PC track-etched membranes [10]. Consequently, hollow nanotubes are formed. The wall thickness of the nanotubes can be controlled by adjusting the time of polymerization. Short polymerization times lead to the formation of thin-walled nanotubes whereas long polymerization times produce thick-walled nanotubes [10]. Two possible reasons have been proposed to explain the formation of nanotubes instead of filled nanowires. First, growth of the polymer occurs preferentially at the pores walls due to electrostatic interactions. Indeed, since the formed polymer is cationic, it adsorbs on the pore walls, which, as a result of the track-etching process, bear anionic sites [10, 18]. Another possible explanation is that diffusion of the reagents in the pores becomes hindered due to the formation of polymer layers on the pore walls [18]. J. Duchet and coworkers also produced polypyrrole nanotubes by chemical synthesis in the pores of a track-etched PC membrane (Fig. 1.6 and 1.7) [18]. As Martin and coworkers, they obtained nanotubes of polypyrrole. Even long polymerization times did not yield completely filled nanowires [18]. However, complete filling could be achieved by performing successive polymerizations [18].

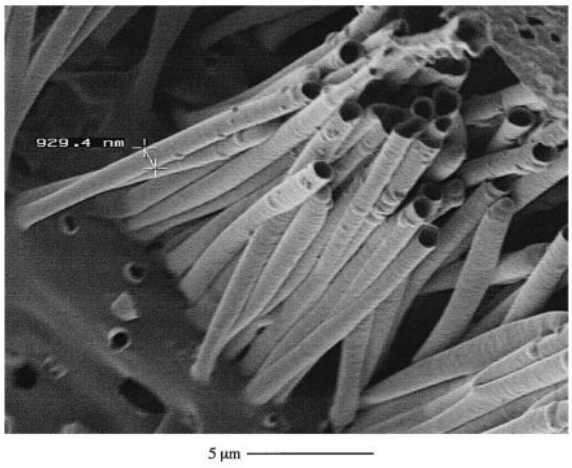


Figure 1.6: SEM image of PPy nanotubes obtained by template synthesis in a PC track-etched membrane. Reproduced from Duchet et al. (1998) [18].

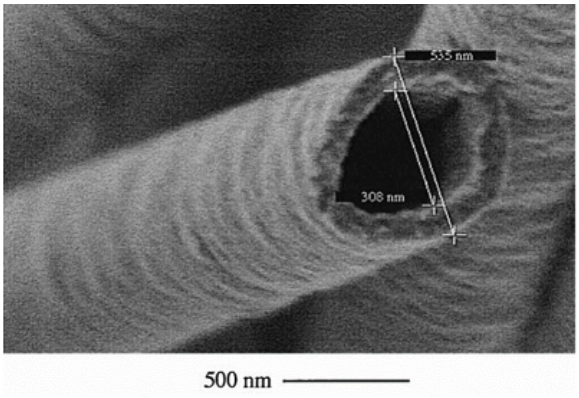


Figure 1.7: SEM image of a PPy nanotube obtained by template synthesis in a PC track-etched membrane. Reproduced from Duchet et al. (1998) [18].

1.1.2 Layer-by-Layer (LbL) assembly

Subject of tremendous scientific interest for the past two decades, Layer-by-Layer assembly (LbL) is a self-assembly technique to produce multilayered films with controlled and tailorable nanostructure, properties and composition [23]. LbL overcomes the drawbacks of other self-assembly techniques, namely Langmuir-Blodgett (LB) and self-assembled monolayers (SAMs), which allow the elaboration of highly-ordered and densely packed monolayers [23]. These techniques are limited by their complexity, cost, lack of stability of the produced layer under certain conditions and limited choice of layer components and substrate [23]. In contrast, LbL assembly has emerged as a simple, inexpensive and highly versatile bottom-up approach for surface modification of various substrates [23]. In light of these numerous advantages, LbL is now investigated for a wide variety of applications, including tissue engineering.

1.1.2.1 Principle

Build-up of multilayered films by LbL assembly is achieved by alternate adsorptions of interacting molecules on a substrate [24]. The interactions between the species used as building-blocks is the driving force for the assembly and ensures the cohesion between neighboring layers of the obtained structure [23, 24]. LbL assembly has been achieved with building blocks presenting various types of interactions, namely electrostatic interactions, hydrophobic interactions or biological interactions [23]. However, electrostatic interactions are the most preferred driving forces for LbL assembly and by far the most studied [24]. Since only electrostatic LbL assembly is used in this thesis, only it will be discussed.

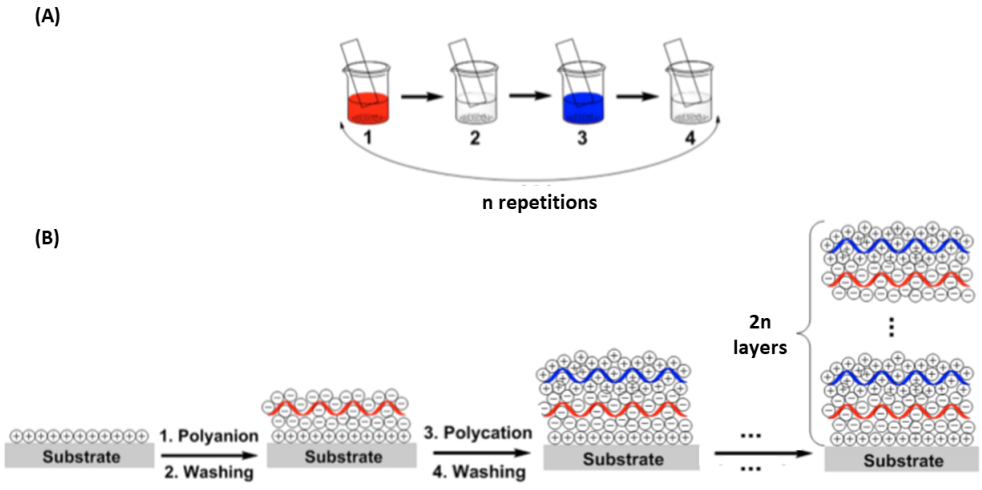


Figure 1.8: Schematic of the LbL assembly of polyelectrolytes of opposite charges, starting for example from a positively charged substrate. (A) Schematic of the LbL dipping technique: the substrate is alternately immersed in polyanionic (in red) and polycationic (in blue) solutions, with rinsing steps in between. (B) Schematic of the film build-up at the molecular level. Repeating the cycle of alternate adsorptions n times results in the build-up of a multilayered film (2n layers). Adapted from Borges and Mano (2014) [23].

Figure 1.8 shows a schematic of electrostatic LbL assembly of oppositely charged polyelectrolytes. A substrate with a charged surface is dipped in a solution of a polyelectrolyte of opposite charge for a certain time. Thanks to the electrostatic attraction between the polyelectrolytes in solution and the substrate, polyelectrolyte chains adsorb on the surface. The charge of the substrate is overcompensated by the adsorbed polyelectrolytes, thus reversing the sign of the surface charge [25]. This charge reversal allows the subsequent adsorption of an additional polyelectrolyte layer upon exposure to a solution of polyelectrolytes of opposite charge compared

to the first layer [25]. With the addition of this new layer, the surface charge is again reversed and the process can be repeated. The repetition of these adsorption cycles leads to the stepwise build-up of the multilayered film [25]. Between each adsorption step, rinsing is necessary to remove weakly adsorbed species and avoid contamination of the next solution [23, 25].

1.1.2.2 Suitable building blocks and substrates

One of the main advantages of LbL assembly is its extensive choice of possible building blocks. A wide variety of synthetic polyelectrolytes are suitable for LbL assembly [25]. In addition, charged nano-objects, such as charged colloids or carbon nanotubes for instance, can be used as well [23, 25]. Most importantly for possible biological applications, a large variety of natural polyelectrolytes are suitable for the process. These include proteins, nucleic acids and polysaccharides [25]. Compared to other self-assembly techniques, LbL assembly can be carried out in aqueous and mild conditions, since it requires no exposure to extreme pH or temperatures or to harmful solvents [23]. This makes LbL particularly suitable to produce films with biopolymers or biologically active molecules with preserved activity [11, 23, 25].

LbL also presents a high versatility regarding the choice of the substrate. LbL can be performed on almost any kind of substrate provided it carries a minimal surface charge [25]. Even if no surface charge is inherently present, it can usually be produced with appropriate surface treatment [25]. In addition, LbL is applicable to a wide variety of substrate geometries including planar substrates, fibers, colloidal particles or even porous substrates [23].

1.1.2.3 Structure and properties of LbL films

Studies have shown that LbL assembly leads to the formation of coherent and uniform coatings with few defects on their surface [25]. The internal structure of these coatings consists in alternating layers of the polyanionic and polycationic species stacked on top of each other. However, they do not present a perfectly multilayered structure [25]. Indeed, the film's layers tend in fact to interpenetrate to a certain level. As a result, LbL films present a stratified structure but are not made of perfectly separate layers [25]. A scheme of the general structure of an LbL film is presented in Figure 1.9.

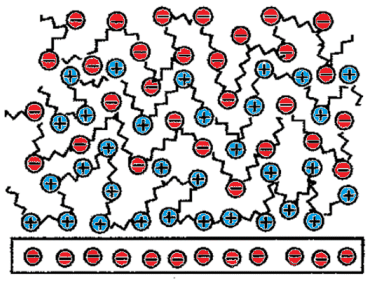


Figure 1.9: Schematic of the general structure of an LbL film. Neighboring layers tend to more or less interpenetrate. Adapted from Bertrand et al. (2000) [25].

However, even if LbL films share the general structure described here above, their properties can vary a lot from one system to another. Indeed, they depend not only on the properties of the building blocks (chain stiffness, charge density, etc.) but also on properties of the medium in which the assembly is carried out (pH, ionic strength, temperature, etc.) [26]. Therefore, processing conditions can be carefully chosen in order to modulate the film's properties [11].

First, the properties of the chosen building blocks can influence significantly the thickness, water content or stiffness of the assembled film. For example, it has been established that polyelectrolytes with a higher charge density usually lead to the formation of thinner films [24]. Also, films made from synthetic polyelectrolytes usually do not exhibit the same structure and properties as films made from natural polyelectrolytes. For instance, films made from polysaccharides and polypeptides tend to be more hydrated, with a higher swelling capability, than synthetic LbL films [12]. This difference of behavior is explained by the presence of more hydrophilic

groups in natural polyelectrolytes (especially polysaccharides) than in synthetic polymers [12].

Then, the film's mechanical properties have been shown to be linked with its growth mechanism [26]. Depending on the polyelectrolytes used, the film's growth regime can be either linear or exponential. Examples of linear and exponential thickness growth are shown in Figure 1.10. Films growing linearly experience a linear increase of mass with the number of deposition steps [12]. On the other hand, films exhibiting an exponential growth show a faster increase of mass and thickness with the number of depositions [12]. Linear growth is most often observed with a pair of synthetic strong polyelectrolytes [23]. However, if the pair comprises a natural polymer (polypeptide or polysaccharide), the growth is usually exponential [23]. As a whole, films growing exponentially tend to be softer than films with linear growth [26]. LbL of polypeptides and polysaccharides thus usually produces soft and gel-like films [11]. Nonetheless, some exceptions exist. For example, LbL films containing collagen exhibit a linear growth [11].

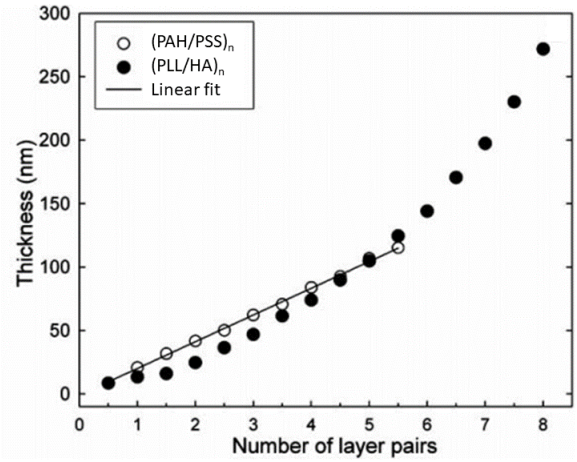


Figure 1.10: Linear versus exponential film growth. Thickness growth as a function of the number of deposited layers n of linearly growing poly(styrene sulfonate)/poly(allylamine hydrochloride) (PSS/PAH) films and of exponentially growing poly-L-lysine/hyaluronan (PLL/HA) films. Reproduced from Picart et al. (2008) [12].

Finally, the properties of the film are also strongly influenced by the choice of the experimental conditions such as pH, ionic strength, temperature, solvent, etc. Among those, the pH of the solutions used for the depositions has been shown to be a crucial parameter, especially for films made from weak polyelectrolytes [24,25]. Indeed, the degree of ionization of weak polyelectrolytes strongly depends on the pH. Thus, changing the pH of the solution can change drastically the charge density and the conformation of the polyelectrolyte chains [24]. This provides the opportunity to control the film structure, composition and thickness by simply adjusting the pH [24]. Sometimes, choosing adequately the pH is even essential to ensure the feasibility of the assembly process. This is the case when assembling a film from proteins for example. Proteins are polyampholytes. They bear both positive and negative charges and the sign of their net charge depends on the pH. They behave as polycations when the pH is below their isoelectric point and as polyanions above [25]. Therefore, if a protein is assembled with a polyanion, the pH must be set adequately to ensure that it behaves as a polycation.

1.1.2.4 Stability of LbL films

Issues of stability mostly apply to LbL films made from weak polyelectrolytes, especially polypeptides and polysaccharides films [12,25]. Indeed, studies have shown that strong polyelectrolyte films tend to present good ageing properties and resistance to change of pH or salt concentration [25]. However, weak polyelectrolyte films are more sensitive to change of pH or ionic

strength [12]. Stability issues can thus arise when the medium in which the film was built up has a pH or ionic strength different from the medium in which the film is intended to be used. In that case, the changes of charge density and conformation undergone by the polyelectrolyte chains upon medium change induce internal stresses disrupting the film [12]. If the pH value of the new medium reduces substantially the charge of the polyelectrolytes, the film simply dissolves [25]. These considerations are especially important for LbL films intended for cell culture or tissue engineering applications. Indeed, build-up conditions do not always coincide with physiological conditions, i.e. a NaCl concentration of about 1.5 M and a pH between 5 and 7.4 [12]. For instance, Johnston et al. have reported that LbL films of collagen and hyaluronan are not stable when the pH is changed from 4 (build-up medium) to 7 (physiological medium) [12].

Fortunately, stability of biopolymeric films can be ensured by creating covalent crosslinks inside the film. Picart and coworkers developed a crosslinking protocol based on carbodiimide chemistry. By means of 1-Ethyl-3-(3-dimethylaminopropyl)carbodiimide (EDC) combined with N-hydroxysulfosuccinimide (sulfo-NHS), covalent amide bonds are created between carboxyl and amine groups present in the film [12]. In addition, crosslinking also has the effect of modifying the mechanical properties of the film. Indeed, crosslinked films have been shown to be stiffer than native non-crosslinked films [26]. This, as will be seen in section 1.3.3.5, was proven to be advantageous for cell culture. Moreover, the stiffness of the crosslinked film can be controlled by tuning the amount of crosslinking agent (EDC) [26].

1.1.2.5 LbL films for tissue engineering

For the past ten years, LbL assembly has been extensively investigated for tissue engineering applications. The ability to coat by LbL a wide variety of substrates with a broad range of species, including biological molecules, makes it a suitable method to modify the surface of tissue engineering scaffolds, with the aim of controlling cellular processes [11, 27]. In this section, the main types of LbL films studied for tissue engineering applications, with an emphasis on bone tissue engineering, are presented.

- **Synthetic polymer films**
  Poly(styrene sulfonate) (PSS) and poly(allylamine hydrochloride) (PAH) LbL films are the most widely used synthetic LbL film in cell studies. Various cell types, including endothelial cells, fibroblasts and osteoblastic cells have been successfully cultured on PSS/PAH films, with good adhesion and proliferation [11]. The main advantage of these synthetic films is a high degree of control on the film's properties and structures through the modulation of parameters such as pH and ionic strength [11].

- **Natural polymer films**
  Most interestingly for tissue engineering, LbL offers the possibility to organize ECM components or biologically active molecules into multilayered architectures while preserving their bioactivity. Therefore, LbL can be used to produce biomimetic coatings [12]. ECM components used for this purpose include proteins such as collagens (COL) or gelatine (GEL) and glycosaminoglycans such as hyaluronan (HA), chondroitin sulfate (CS) and heparin (HEP) [26]. Other polysaccharides from algae or crustacean shells, such as alginic acid (ALG) or chitosan (CHI) have also been studied [26]. For instance, osteoblasts have been successfully cultured on CHI/GEL LbL films with good adhesion and viability [28]. Crosslinked films made from CS, an important component of bone tissue, also yielded good adhesion of osteoblastic cells [29]. HA/COL films, which are investigated in this thesis, were found to enhance proliferation and differentiation of preosteoblastic cells [30]. The main advantage of natural LbL films is that, unlike synthetic films, they are able to interact specifically with cells to stimulate a certain response [11]. The interactions between cells

and biomimetic coatings, involving collagen and hyaluronic acid especially, will be reviewed in more details in section 1.3.3.

In addition, LbL coatings can potentially serve as reservoir for biologically active molecules provided a sufficiently high swellability and porosity [12]. Growth factors, proteins or drugs can be loaded in the film during its build-up. These are then released either by diffusion to the surface of the film or upon degradation of the film by enzymes or hydrolysis [12]. This opens up prospects for the development of smart surfaces with enhanced bioactivity for tissue engineering [12, 27].

1.2 Mouse MC3T3-E1 cell line as an osteoblastic model

In vivo, bone formation goes through the following steps: preosteoblast recruitment, osteoblast precursor differentiation to postmitotic matrix-producing osteoblasts and, finally, osteoid mineralization by differentiated osteoblasts [31]. Different studies have tried to come up with a cell line able to reproduce this osteoblastic development *in vitro*. One cell line which retained attention for this purpose and succeeded in reproducing *in vitro* the equivalent of the aforementioned steps is the MC3T3-E1 cell line [31, 32, 33].

This section starts by describing the genesis of the MC3T3-E1 cell line. Next, the proliferation and differentiation phases, as firstly described by Quarles et al. [31], are presented. Then, additional markers for osteoblastic differentiation and their expression patterns are presented. Finally, some assay methods for the main markers for osteoblastic differentiation are described.

1.2.1 Description

The MC3T3-E1 cell line is a murine clonal osteogenic cell line which retains the capacity to differentiate into mature osteoblasts and to mineralize *in vitro* [32, 33, 34]. This cell line was established in 1981 by Kodama et al. [32] from newborn mouse calvaria under a 3T3 subculturing schedule (hence the name MC3T3). The 3T3 schedule means that the cells were transferred at 3-day intervals at inoculum of 3x10^5 $cells/25cm^2$ in order to select cells sensitive to postconfluence inhibition of division [32]. Among the different subcultures, only one, named MC3T3-E, showed the typical behavior of osteoblast-like cells regarding the evolution with time of alkaline phosphatase (ALP) activity. Indeed, the MC3T3-E cells started by showing a low ALP activity during the growing phase (up to day 4 of culture) but then showed an increasing ALP activity [32]. From these MC3T3-E cells, ALP-positive colonies were isolated. The clone MC3T3-E1 was the one showing the highest ALP activity and was, therefore, the permanent cell line which was selected for further investigation [32]. In 1983, Sudo et al. demonstrated that the MC3T3-E1 cell line expresses parameters of the osteoblast phenotype such as synthesis of type I collagen, alkaline phosphatase activity and extracellular matrix mineralization [31, 33]. In 2010, Yazid et al. demonstrated that MC3T3-E1 cells can only differentiate into osteoblasts and not osteoclasts [34]. This differentiation into osteoblasts only is a characteristic of progenitor cells [34].

Other solutions, such as malignant osteoblast cell lines or primary osteoblast cultures, were considered as models for the osteoblastic development [31, 33, 34]. However, malignant osteoblasts failed to display the normal coupling of differentiation and growth arrest due to their unrepressed replicative activity [31]. As far as primary osteoblast cultures are concerned, they have the disadvantages of containing various cell populations (e.g. fibroblast, chondroblasts and osteoblasts) and of loosing osteoblast specific characteristics during subcultivations [31].

1.2.2 Proliferation and differentiation [31]

In 1992, Quarles et al. [31] studied the proliferation and differentiation stages of MC3T3-E1 cells in culture. The cells were plated into multiwell dishes and grown for periods ranging from 2 to 31 days in α-MEM containing 10% FBS volume with and without supplementation with β-glycerol phosphate and/or ascorbate in order to study the different stages of the osteoblastic development. They reported three main stages: the proliferation phase and the differentiation phase which is itself divided into an intermediate phase and a mineralization phase.

1.2.2.1 Proliferation

The initial stage of development of the osteoblast-like cells is the proliferation phase. During this period, the active replication of undifferentiated cells results in a rapid increase of the cell number and a high rate of DNA synthesis. The DNA synthesis is coupled with high type I collagen mRNA expression and collagen biosynthesis. However, those immature cells fail to mineralize and express low levels of alkaline phosphatase. The collagen accumulation in the extracellular matrix is low during this period despite the high rate of collagen production.

1.2.2.2 Differentiation

When the cells attain confluence, the initial phase (i.e. proliferation) is followed by an intermediate phase (the first stage of differentiation). During this second period, the replication progressively decreases until the cells become quiescent. This downregulation of replication is coupled with a significant increase in alkaline phosphatase activity at the onset of growth arrest. This sharp increase in ALP is a marker of the mature osteoblast function. The reduction in DNA synthesis at the onset of growth arrest is coupled with a reduction in type I collagen mRNA expression and collagen biosynthesis. At this stage, significant amounts of collagen accumulate in the extracellular matrix. However, mineralization of the extracellular matrix is still lacking.

The final phase consists in the formation of a mineralized extracellular matrix. This mineralization requires the presence of ascorbate and β-glycerol phosphate in the culture medium.

1.2.2.3 Effect of ascorbate and β-glycerol phosphate on MC3T3-E1 cells development

Ascorbate and β-glycerol phosphate do not affect the replication rate, the attainment of the onset of growth arrest or the onset of osteoblast differentiation as measured by alkaline phosphatase. However, ascorbate enhances alkaline phosphatase activity in mature osteoblasts. β-glycerol phosphate has no effect on alkaline phosphatase activity on its own but it acts synergistically with ascorbate. Indeed, in the presence of both ascorbate and β-glycerol phosphate, a significant increase in alkaline phosphatase activity is observed after the onset of growth arrest compared to cells grown in the presence of FBS alone.

Regulation of collagen biosynthesis or type I collagen mRNA expression are not affected by the presence of ascorbate or β-glycerol phosphate. However, the ascorbate supplementation is absolutely required to get collagen accumulation into the extracellular matrix in mature cells. Addition of β-glycerol phosphate enhances this effect of ascorbate but β-glycerol phosphate used without ascorbate does not lead to collagen accumulation in the extracellular matrix.

Finally, mineralization of the extracellular matrix is observed only in mature cultures in the presence of both ascorbate and β-glycerol phosphate.

1.2.3 Other markers for osteoblastic differentiation

In addition to alkaline phosphatase and type I collagen, a number of other bone-related proteins have been used as markers for osteoblastic differentiation in different studies [35, 36, 37]. The main ones are osteocalcin (OCN), osteonectin, osteopontin (OPN), bone sialoprotein (BSP), transforming growth factor-β1 (TGF-β1), histones H3 and H4, fibronectin,Osteoblast-specific factor 2 (Osf2) (also known as core binding factor α1 (Cfba1/Runx2)), the parathyroid hormone (PTH)/parathyroid hormone-related protein (PTHrP) receptor and the ribosomal protein S6 [35]-[36]- [37]. Those markers are briefly described hereafter:

- Alkaline phosphatase is an enzyme which regulates phosphate metabolism through hydrolyzation of phosphate esters. It is an early marker of osteoblast differentiation [36].
- Type I collagen is bone main organic component. Its quantity increases during bone formation [36].
- Osteocalcin and osteopontin play a role in bone mineralization and nodule formation. They are used as marker for osteogenic differentiation [35, 36].
- Osteonectin is the most abundant non-collagenous matrix protein in bone. In the skeleton, it is essential to balance bone formation and resorption in response to the parathyroid hormone (PTH). It promotes osteoblast differentiation [38].
- Bone sialoprotein is believed to play a role in mineralization. *In vitro* studies have shown that it holds a role in hydroxyapatite nucleation [37].
- Osteoblast-specific factor 2 (Osf2), also reported as core binding factor α1 (Cfba1/Runx2), AML3 or PEBP2α1, is an osteoblast-related transcription factor necessary for the expression of the osteocalcin gene and is the main specific transcription factor involved in osteogenesis [37, 39]. However, its presence alone in a MC3T3-E1 subclone is not sufficient to mark osteoblast differentiation [37].
- Transforming growth factor-β1 (TGF-β1) is an immunoregulatory cytokine. It enhances osteoblast proliferation, blocks osteoblast apoptosis and it enhances the production of extracellular bone matrix proteins by osteoblasts in the early phase of osteoblast differentiation [40].
- Histones H3 and H4 are two histones playing a prominent regulatory role in chromatin formation and which retain *in vitro* the capacity to impede transcription [41].
- Fibronectin is a protein involved in cell attachment, migration and differentiation [42].
- Parathyroid hormone (PTH) is a hormone which maintains calcium homeostasis by promoting calcium release in the bones and enhancing calcium reabsorption in the kidney [43].
- The ribosomal protein S6 is a component of the S40 ribosome subunit [44].

In 1995, Choi et al. further studied the expression patterns of bone-related proteins during osteoblast differentiation in MC3T3-E1 cells [35]. Those proteins have a temporal expression pattern during cell differentiation. During the proliferation period (days 4-10 of culture) the expressions of histones H3 and H4 and of ribosomal protein S6 are high (Fig. 1.11) [35]. ALP activity is high at the beginning of the bone matrix formation/maturation period (day 10) and then decreases until the end of this period (day 16) but remains higher than the level observed during the proliferation period (Fig. 1.12) [35]. Other proteins have specific expression patterns during this bone matrix formation/maturation period (days 10-16 of culture). Type I collagen biosynthesis and expression are high (Fig. 1.11). The expressions of TGF-β1, osteonectin

and fibronectin are high as well and are maximal around the end of this period (day 16) (Fig. 1.13) [35]. A distinction can be made in the expression patterns of those proteins. On the one hand, type I collagen and TGF-β1 expressions are higher during the maturation period than during both the proliferation and mineralization periods. On the other hand, fibronectin and osteonectin expressions are higher during the maturation and mineralization period than during the proliferation period [35]. During the third period, the mineralization period (days 16-30 of culture), the expression of osteocalcin is high and keeps increasing until day 28 (Fig. 1.13) [35]. Furthermore, bone nodule formation is observed during this period [35].

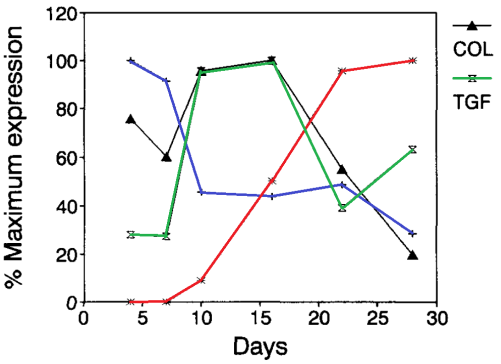


Figure 1.11: Expression of type I collagen (▲,black), TGF-β1 (⧖,green), histone H4 (+,blue) and osteocalcin (*,red) during the differentiation of MC3T3-E1 osteoblastic cells. Levels of expression are expressed in percent of the maximal expression observed during the osteoblastic differentiation. Adapted from Choi et al. (1996) [35].

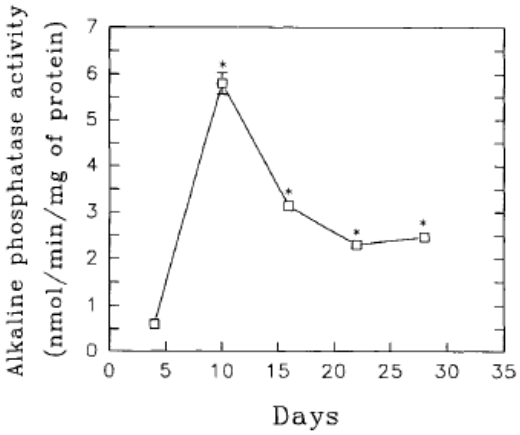


Figure 1.12: Alkaline phosphatase activity during the differentiation of MC3T3-E1 osteoblastic cells. Adapted from Choi et al. (1996) [35].

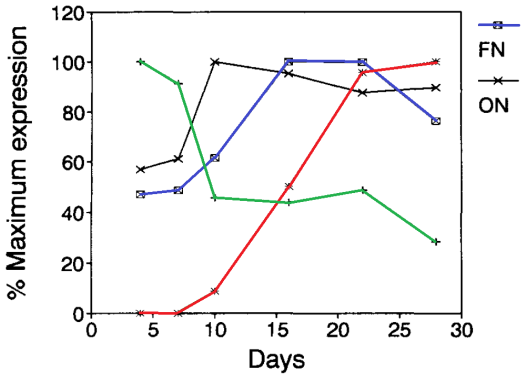


Figure 1.13: Expression of fibronectin (⊠, blue), osteonectin (×, black), histone H4 (+, green) and osteocalcin (*, red) during the differentiation of MC3T3-E1 osteoblastic cells. Levels of expression are expressed in percent of the maximal expression observed during the osteoblastic differentiation. Adapted from Choi et al. (1996) [35].

It is worth noticing that studies about expression patterns of bone-related proteins of different culture systems yielded different results. For instance, the protein expression patterns of rat calvarial osteoblasts or chicken osteoblasts differ from the one of MC3T3-E1 [35]. Indeed, while the rat calvarial osteoblasts produce bone matrix proteins mainly during the proliferation period, the expression of the same proteins in MC3T3-E1 is not as clearly divided between the proliferation, the maturation and the mineralization periods [35]. Furthermore, the maximal expression of those proteins is not concomitant between MC3T3-E1 cells and rat calvarial cells [35]. However, it is not known to which extent these differences are due to the different cell types or to differences in culture conditions such as the cell plating number or the serum lot [35].

1.2.4 Main assays for osteoblastic differentiation markers

The alkaline phosphatase activity is usually evaluated by lysing the cells. The ALP activity of the lysates is then extracted from the production pattern of p-nitrophenol (absorbing at 405-410 nm) which is obtained following the dephosphorylation of para-nitrophenylphosphate (p-NPP) by the ALP [34, 35]. The capacity of osteoblast to mineralize *in vitro* can be evaluated through the visualization of bone nodules by von Kossa or Alizarin red staining [34, 35, 39]. The level of expressions of the other proteic markers such as osteopontin, osteocalcin, Osf2, PTH/PTHrP receptor, collagen are evaluated by analysis of the RNA content. Total RNA content is first isolated from the cell using different methods such as the method of Chomczynski and Sacchi [37] or the use of TRI-Reagent [34]. The total RNA is then analyzed, for instance by reverse transcription polymerase chain reaction (RT-PCR) [34], in order to evaluate the quantity of specific mRNA of each of the proteins of interest.

1.3 Major cell-instructive cues

Numerous studies have shown that cellular functions such as, for instance, adhesion, proliferation and differentiation can be affected by the physical and chemical properties and the topography, particularly at the nanoscale, of the substrates on which they are plated [45, 46, 47]. This section starts by describing the cell interaction with the material used in this master thesis for the fabrication of the biointerfaces: polypyrrole. Next, the effect of nanotopoghraphy on cellular behavior are reviewed. Finally, the ways that ECM-derived surface coatings can be used to control cellular functions are described.

1.3.1 Cellular interactions with polypyrrole

Polypyrrole (PPy) possesses many properties desirable for tissue engineering applications, including biocompatibility, electrical conductivity, good stability and resistance to corrosion, ease of synthesis and flexibility in processing [48, 49]. Therefore, it has been the subject of many studies investigating its suitability as tissue engineering scaffold for different types of tissues, including bone.

1.3.1.1 Physical properties of polypyrrole

Physical properties, both bulk and surface properties, can have a significant impact on the behavior of seeded cells. Therefore, in this section, the main properties of polypyrrole to consider for tissue engineering applications will be described.

Polypyrrole (PPy) has the particularity of being an electrically conductive polymer. In tissue engineering applications, PPy substrates are thus able to provide electrical stimulation of the seeded cells. The conductivity of PPy stems from its conjugated structure, which allows charge mobility along the polymer chains [48, 50]. As shown in Figure 1.14, PPy backbone presents an alternation of single and double carbon-carbon bonds. In a reduced state, PPy has an initially neutral backbone and behaves therefore like an insulator [50]. However, positive mobile charge carriers are formed in the backbone upon oxidation, thus rendering it conductive [50]. This process is referred to as p-doping and can be achieved either chemically by using a strong oxidizing agent or electrochemically [50]. When oxidized, an electron is removed from the backbone, thus producing a polaron (a radical cation). Upon further oxidation, pairs of polarons combine to form bipolarons (dications), which can migrate along the conjugated structure of the backbone, thus providing conductivity [48, 50]. The introduction of polarons and bipolarons in the chain is illustrated in Figure 1.14.

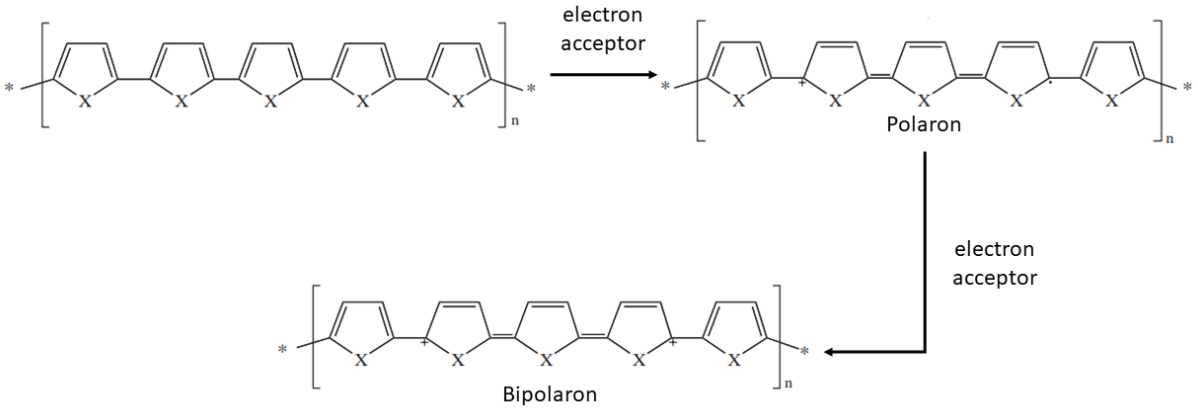


Figure 1.14: Introduction of polaron and bipolaron upon oxidation of a heterocyclic polymer (for polypyrrole X=NH) Removal of a first electron upon oxidation introduces a radical cation in the chain, called a polaron. Further oxidation of the same chain segment produces a second polaron that combines with the first introduced polaron to form a bipolaron (bication). Adapted from Guimard et al. (2007). [48]

Since positive charges are introduced in the backbone during p-doping, negative counterions must be introduced during the process to maintain overall charge neutrality (Fig. 1.14) [50]. These negative counterions are called dopants. A wide variety of dopants can be used in the synthesis of conductive PPy, including small salt ions, polyelectrolytes or even biological polymers such as polysaccharides or proteins [48]. However, doping with biological molecules can only be achieved by electrochemical synthesis [48]. Adequate choice of the dopant is crucial because its chemical nature influences, among others, the conductivity of the obtained PPy [48].

Aside from electrical conductivity, mechanical properties and stability are also important to consider for tissue engineering application. Unmodified polypyrrole is brittle and rigid [48, 51]. This lack of mechanical flexibility can be a drawback for tissue engineering application [48]. This is especially the case if the scaffold is designed to be implanted *in vivo*, since it has to be able to withstand physiological loads. Nonetheless, it is possible to improve the scaffold's mechanical properties by combining PPy with more flexible materials such as polyesters [48]. The choice of dopant has also been shown to influence the stiffness of PPy [52].

Finally, morphology and surface topography can also affect significantly cell behavior (section 1.3.2). However, these properties are highly dependent on the chosen conditions for the polymerization process [48]. For instance, chemical synthesis usually yields thick PPy films or powder [48]. Electrochemical synthesis, on the other hand, allows the production of very thin films (of the order of 20 nm) [48]. Surface topography of PPy films can be modified through different processing parameters such as pH, solvent, polymerization times, temperature, etc. [48]. The dopant has also a strong impact on the surface topography of the produced PPy, especially when large molecules are used [48]. For instance, Ateh et al. have studied the impact of dopant and polymerization time on the surface topography (Fig. 1.15) [50].

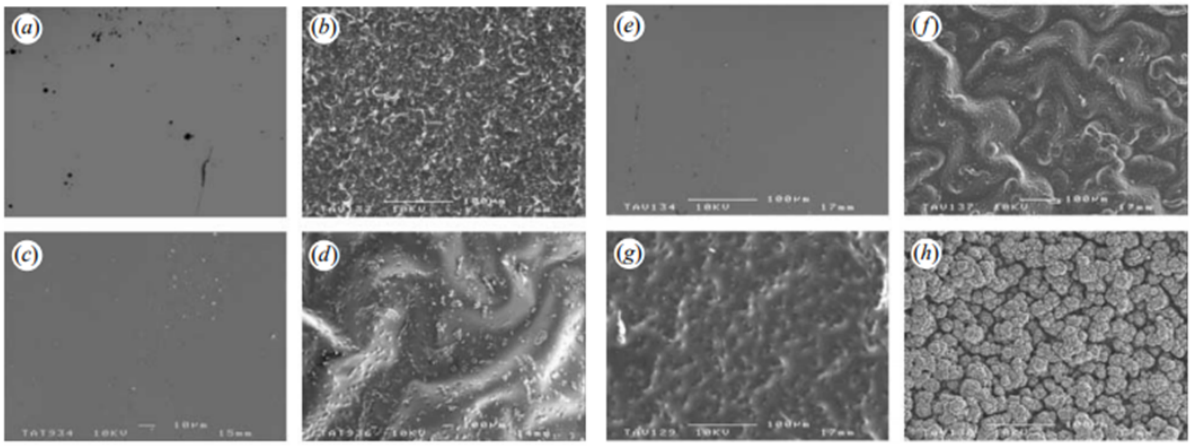


Figure 1.15: Scanning electron microscopy images of the surface topography of elctrochemically synthesized PPy films for different dopants and different polymerization times. (a-b) PPy doped with chloride (c-d) PPy doped with polyvinyl sulphate (e-f) PPy doped with dermatan (g-h) PPy doped with collagen. For each dopant, the first image corresponds to short polymerization times while the second corresponds to long polymerization times. Reproduced from Ateh et al. (2006) [50].

1.3.1.2 Biocompatibility

The substantial interest of polypyrrole as cell scaffold comes from the discovery of its compatibility with many biological tissues in the 1980s [49]. Indeed, polypyrrole was one of the first conducting polymers whose interactions with mammalian cells was studied [53]. Since then, numerous studies on PPy-cell interactions have shown that PPy substrates support the adhesion and growth of a wide variety of cell types [48]. A non-exhaustive list includes namely endothelial cells, neural cells (neurons and support cells), keratinocytes, mesenchymal stem cells and osteoblasts [48, 54]. An in-depth biocompatibility assessment of polypyrrole (both *in vivo* and *in vitro*) was performed by Wang et al. [54]. Toxicity tests in compliance with ISO 10993 an ASTM F1748-82 standards were carried out [54]. An extraction solution made from chemically-synthesized polypyrrole powder was tested on various animal models for acute toxicity, subacute toxicity, change of body temperature, hemolysis of red blood cells, allergic reactions and mutagenesis [54]. They reported that the PPy extraction solution had none of these adverse effects on the tested animals [54]. Cell viability in the PPy extraction solution was also measured *in vitro* on rat Schwann cells, by replacing their culture medium with a medium containing 50% of the PPy solution. Schwann cells showed significantly better survival rates in the PPy modified medium than in the control group in a medium containing 50% of saline solution, thus indicating that the PPy extracts are not cytotoxic [54].

However, if PPy itself is biocompatible, its monomer, pyrrole, and short oligomers are toxic for biological tissues. Thus, prior to culture, PPy substrates should be washed thoroughly to remove any toxic species potentially remaining after the synthesis [50]. Biocompatibility can also be affected by the dopant used in the synthesis, since dopants can leach out of the substrate into the culture medium and potentially disrupt cell function [52]. For instance, PPy is commonly doped with chloride because of its biocompatibility [48]. PSS is another commonly used dopant for biomedical applications because of its inert and non-cytotoxic nature [52].

1.3.1.3 Effect on cell function

In addition to being biocompatible, numerous studies have shown that PPy substrates can enhance cell functions, such as proliferation and differentiation, of various cell types [48, 50, 55]. As mentioned previously, PPy properties potentially affecting cell function can be modulated through numerous parameters in the synthesis of PPy and through the choice of dopant. Due to

the infinite number of possible combinations of such factors, generalization of the cell response on PPy proves difficult [50]. Moreover, it has also been shown that the response depends on the cell type [50]. Therefore, this section will be restricted to the subject of interest of this thesis, bone tissue engineering, and several examples of studies investigating the effect of PPy on cell function for this application will be presented.

Due to its conductive nature, PPy has mainly been studied for nerve, cardiovascular and muscle tissue engineering applications [49]. However, it has also emerged as a promising biomaterial for bone tissue engineering . Indeed, PPy substrates have been shown is several studies to promote osteogenesis [55, 56]. For instance, Castano et al. demonstrated that substrates coated with ultrathin PPy films affect the induction of osteogenicity of rat mesenchymal stromal cells [55]. Ultrathin PPy films were obtained by admicellar polymerization, which involves the use of a surfactant in addition to the monomer and oxidizing initiator [55]. In that case, ammonium persulfate was used as oxidizing agent [55]. Cell differentiation towards the osteoblastic phenotype was assessed by alkaline phosphatase (ALP) and calcium assays [55]. Films of different thickness were shown to induce drastically different behaviors. Thicker PPy films, obtained at higher monomer concentration, showed poorer attachment and differentiation than on regular tissue culture polystyrene (TCP) dishes. The authors explained the poor results of the thicker films by a surface topography impeding cell adhesion [55]. However, thin films, obtained with low monomer concentration, exhibited an increased induction of cell adhesion and differentiation, comparable to the TCP controls [55].

Hu et al. cultured rat bone marrow stromal cells (BMSCs) on chemically synthesized PPy oxidized by ammonium persulfate [57]. By adjusting the concentration of monomer, films of different conductivity (ranging between about 0.5 and 2.5 S/m) were obtained [57]. Films made from higher pyrrole concentration presented a higher conductivity [57]. As presented in Figure 1.16 measurement of the calcium content after culture in osteogenic medium demonstrated an increased mineralization of the ECM on the PPy films compared to the TCP controls [57]. In addition, the films with the highest conductivity were found to have the highest normalized calcium deposition [57]. Finally, the peak in ALP expression occurred earlier on the PPy films than on the TCP controls. These results indicate that the electroactive nature of the PPy films contributes to speeding up osteogenesis [57].

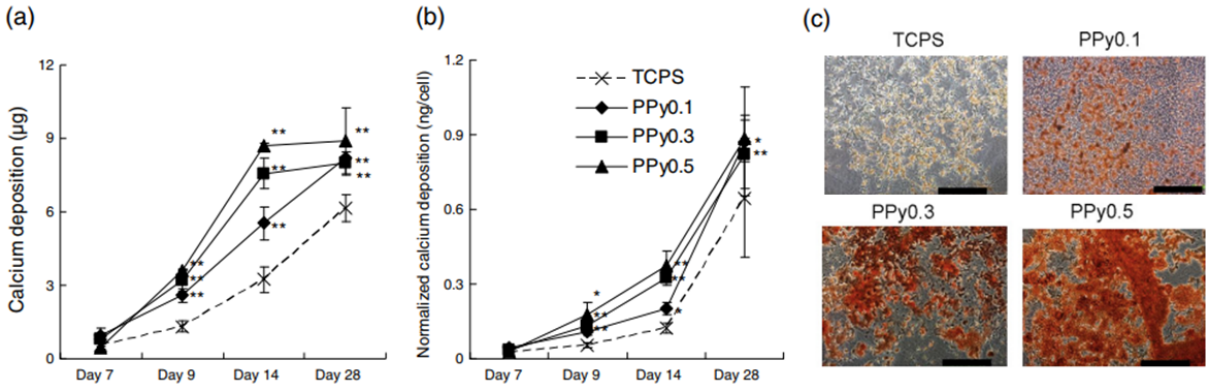


Figure 1.16: Calcium deposition of rat BMSCs cultured on PPy films in osteogenic medium. The PPy films were synthesized from different pyrrole concentrations (0.1, 0.3 and 0.5 M). (*:p-value<0.05, **= p-value<0.01 compared to the TCP controls) (a) Calcium deposition in the ECM measured with the Ca-OCPC complex method. (b) Calcium deposition normalized by cell number (determined by LDH assay). (c) Alizarin red S staining after 14 days of culture in osteogenic medium was used to assess the ECM mineralization and its distribution. Reproduced from Hu et al. (2014) [57].

1.3.1.4 Biofunctionalization

In order to enhance its bioactivity, PPy can also be functionalized with biological molecules by means of physical adsorption, entrapment or covalent attachment (Fig. 1.17) [48].

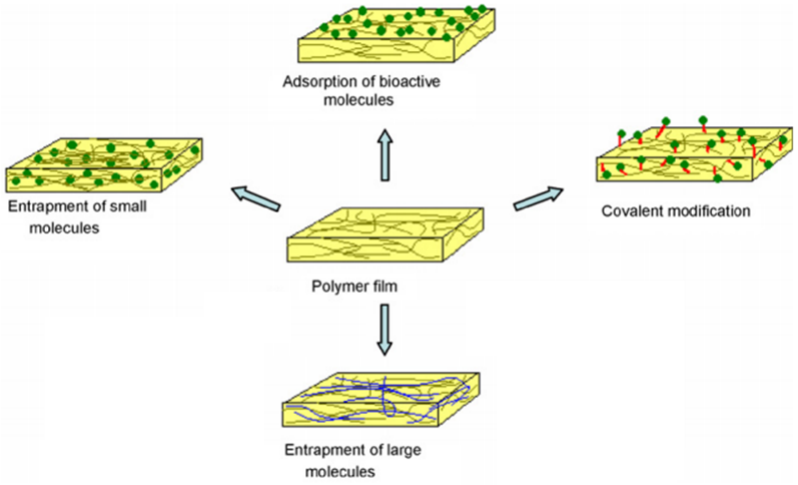


Figure 1.17: Biofunctionalization strategies of PPy. PPy can be modified via non-covalent methods: physical adsorption of biological molecules or entrapment of molecules in the film (either as dopant or in addition to the dopant). Alternatively, biological molecules or groups can be grafted covalently to the surface. Reproduced from Guimard et al. (2007) [48].

First, a straightforward approach to modify PPy surfaces is through non-covalent adsorption of bioactive molecules on the surface [48, 51]. In this case, charged bioactive molecules are put into contact with the PPy substrate after its synthesis [51]. As the surface of oxidized PPy is charged, the biomolecules adsorb on its surface through electrostatic interactions [51]. Small biological molecules can be immobilized this way on the PPy surface. Alternatively, multilayered films of biological polyelectrolytes can also be obtained through LbL assembly. This approach is the simplest to perform. Nonetheless, its outcome is sensitive to pH and the biomolecules are susceptible to desorption [51]. The other non-covalent approach consists of entrapping the biological molecules in the PPy substrate during its synthesis [48, 51]. This is achieved by mixing the desired biomolecule with the monomer, the dopant and the solvent before its electrochemical synthesis. This approach has been successfully used to entrap large molecules, such as DNA or enzymes for biosensing applications [51]. In particular for tissue engineering applications, studies have also investigated the entrapment of adenosine triphosphate (ATP) or nerve growth factors (NGF) [51]. For instance, entrapment of NGF and its controlled release upon reduction of the PPy substrate have been shown to promote neurite extension of PC12 cells, a cell line commonly used as a primary neuron model [48]. Alternatively, the desired biomolecules can be entrapped in the PPy substrate directly as dopant [48]. Indeed, a wide variety of biomolecules can be integrated in PPy substrate as dopant including collagen, heparin, laminin, fibronectin and chitosan [50, 51]. The choice of a particular biomolecule as dopant can be dictated by the targeted cell or tissue type. For instance, heparin-doped films have been studied for the culture of endothelial cells, as it is an important component of the ECM of blood vessels and has anticoagulant properties [50]. For bone tissue, Serra Moreno et al. studied PPy films with various polysaccharides as dopant: heparin (HEP), chondroitin-4-sulphate (CS) and hyaluronic acid (HA) [58]. The incorporated polysaccharides were shown to retain their specific functions. MC3T3-E1 preosteoblastic cells cultured on all three sorts of films showed good viability, proliferation and differentiation [58]. Level of expression of Runx2 and ALP activity were found to be comparable to control group cultured on reference dishes, thus showing that the polysaccharide-doped PPy films are suitable to maintain the normal osteoblast metabolism and differentiation [58]. If this approach is simple to carry out, the main

drawback of using biomolecules as dopant is that only a small amount of them can actually be bound [51]. The chosen dopant can also have a negative impact on the electrical conductivity [51].

Covalent binding presents the advantage of a better long-term stability than non-covalent approaches [51]. Multiple techniques to this aim have been proposed. A notable example is the grafting of cysteine on PPy chains [59]. Cysteine was found to be able to form covalent bonds with pyrrole cycles via their sulphydryl group [59]. Using this approach, De Giglio et al. grafted a RGD containing peptide with a terminal cysteine on PPy films [59]. Rat calvarial osteoblasts were cultured on the RGD-grafted PPy films with a reported 230% increase in cell attachment compared to the bare PPy and glass controls [59].

1.3.2 Effect of nanotopography on cellular behavior

It is known that nanoscale surface topography of materials significantly affects the interactions with proteins and cells [45]. The main motivation for studying the effects of nanoscale topography is the hope to artificially reenact the set of nanotopographical cues naturally present in cells' microenvironment. It is believed that nanotographical cues could be tailored to regulate cell function in a way similar to the one in which the ECM features affect cell functions [45]. Indeed, *in vivo* cells respond to textured cues in the ECM such as pits, pores, protrusions and fibers in a length scale of 5-200 nm [45, 46].

This subsection will start by describing how the surface topography can affect cellular behavior. Next, the effect of nanotopography on osteoblastic cells more precisely will be presented. Finally, being even more specific, the effect of nanotopography on MC3T3-E1 cells will be described.

1.3.2.1 General effect of surface topography on cellular behavior

Surface topography, at the micro and nanoscale, can influence cellular behaviors among which adhesion, differentiation, morphology, migration, orientation, focal adhesion, cytoskeletal development, gene expression and protein production [45,46]. It has long been recognized that microscale surface topography can affect cellular response but it has only been shown recently that surface features as small as 10 nm can affect cell adhesion as well [45, 46]. Furthermore, it has been shown that nanoscale surface topography has a significant influence on both protein adsorption and cellular response [45]. In the end, the effect of surface properties and topography on cellular response is conveyed by the proteins which adsorbed on the surface. Indeed, when a biomaterial is in contact with a biological system, proteins spontaneously adsorb on its surface [45, 46, 60]. This spontaneous protein adsorption results in a surface-bound protein layer which governs the subsequent cell attachment by interacting with cell surface receptors [45, 46]. This mediation of the cellular response to the nanotopography by the adsorbed protein layer is supported by the fact that nanoscale surface topography significantly affects cell adhesion only in the presence of serum [45]. The effect of the surface topography on the cellular response depends on the speciation, conformation and orientation of the proteins adsorbed on this surface [45]. The overall effect of surface nanoscale features on protein adsorption is not fully understood yet [45]. It is believed that the increase of surface area, combined with other mechanisms still to be identified, is responsible for the altered protein adsorption on nanotopographical surfaces compared with flat surfaces [45]. For instance, the observation that nanogrooves promote the alignment of osteoblast-like cells compared to flat surfaces is believed to be due to the fact that the nanogrooves act as sites for protein deposition creating therefore protein patterns which reflect the topography of the underlying substrate [45].

Therefore, the ability to produce surfaces with controlled nanotopograhies might be a promising solution to direct cell functions [45]. The influence of nanotopography on cellular

response has been investigated in numerous studies for various cell types (e.g. osteoblasts, fibroblasts, neural cells) and topographies. Examples of nanotopographies whose effect has been studied on cell function are shown in Figure 1.18. It results from those studies that different cell types react differently to different surface nanostructures [45, 46]. Therefore, it is difficult to extract a general trend but what can be concluded from these different studies is that cellular responses can be modulated in the short and medium term by the nanoscale surface topography [45]. The rest of this subsection will therefore focus on how osteoblastic cells respond to nanotopographical features.

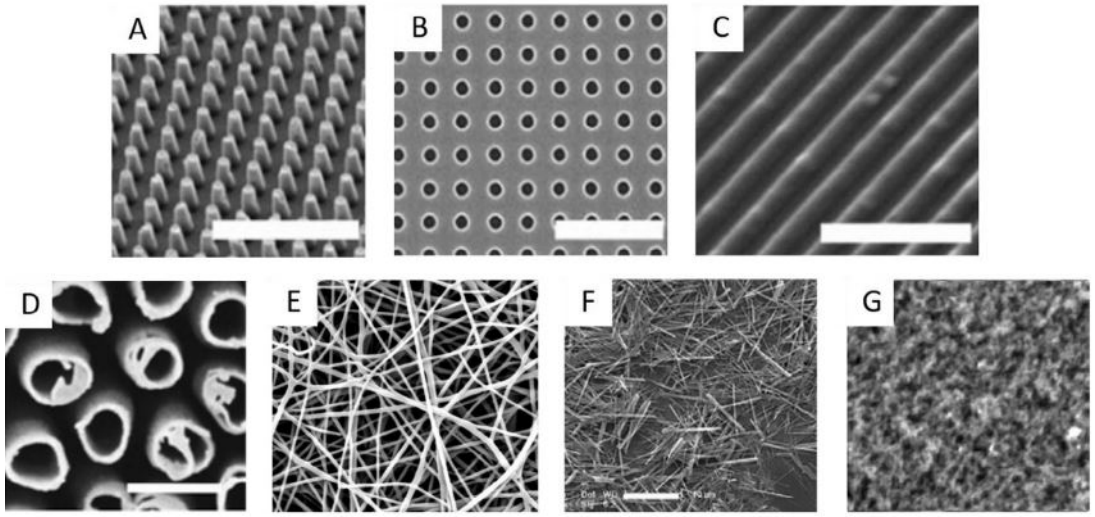


Figure 1.18: Examples of nanotopographical features whose influence on cellular response have been studied. (A) Nanopillars (B) Nanopits (C) Nanogrooves/gratings (D) Nanotubes (E) Nanofibers (F) Nanowires (G) Surface roughness. Reproduced from Dobbenga et al. (2016) [61].

1.3.2.2 Effect of nanotopography on osteoblastic cells

Surface nanotopography has been observed to promote a variety of cellular functions of osteoblastic cells including adhesion, proliferation, bone matrix synthesis, gene expression and osseointegration [45]. The effect of nanoscale surface topography on osteoblast adhesion has been shown on nanophase alumina. Indeed, nanophase alumina was able to support three times more cells than what was the case on conventional alumina [45]. This effect was attributed to the conformation of vitronectin adsorbed on the nanophase alumina [45]. Concerning proliferation, carbon fibers of less than 100 nm diameters have been shown to increase osteoblast proliferation compared with fibers of diameter greater than 100 nm [45]. Furthermore, the osteoblasts which adhered on the fibers of diameters less than 100 nm produced more ALP and more extracellular calcium than the osteoblasts adsorbed on fibers of larger diameters [45]. Osteoblast morphology has been shown to be modulated by the specific shape of nanoscale features. For instance, on silicon substrates containing nanogrooves, osteoblasts elongated and aligned along the long axis of the nanogrooves and actin organization was parallel to the nanongrooves [45]. It was also shown that nanopits of appropriate depth can enhance osteoblast functionality. Indeed, human fetal osteoblast cells (hFOB) cultured for 24 h on poly(L-lactic acid) and polystyrene (PLLA/PS) (50/50 w/w)-demixed nanopit-textured films (Fig. 1.19) with nanopits of 14 nm and 29 nm depth exhibited increased cell adhesion, cell spreading, and integrin expression compared with osteoblasts cultured on similar films with nanopits of 45 nm depth or on control flat PLLA films (Fig.1.20). Best results were obtained for the 14 nm deep nanopits [46,62].

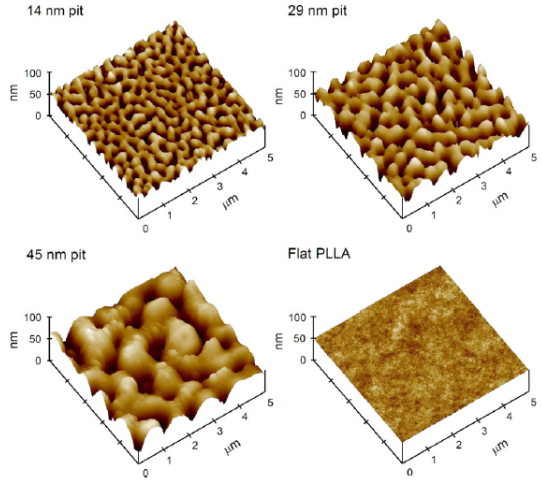


Figure 1.19: AFM height images of PLLA/PS (50/50 w/w)-demixed nanopit-textured films spin-cast at various solution concentrations of 0.5% (14 nm deep pits), 1% (29 nm deep pits), and 1.5% (45nm deep pits) w/w and flat PLLA films. Reproduced from Lim et al. (2007) [62].

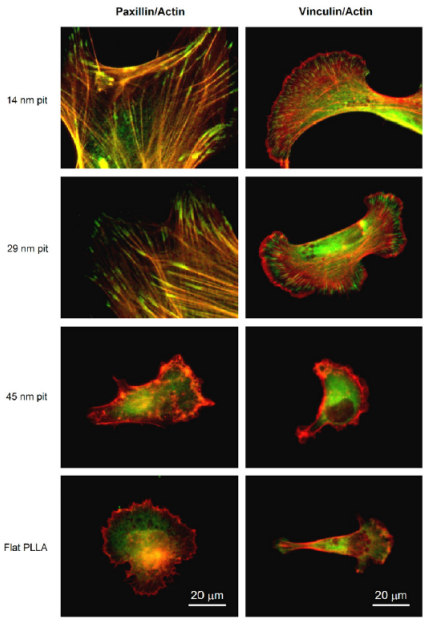


Figure 1.20: Paxillin and vinculin (both green) immunofluorescent staining double-labeled with actin (red) for hFOB cells cultured for 24 h on PLLA/PS (50/50 w/w)-demixed nanopit-textured films and flat PLLA films. Reproduced from Lim et al. (2007) [62]

It is important to notice, however, that the dimensions of the nanoscale features (e.g. height and width of nanopits) is not enough to control the cellular response. Indeed, in addition to those dimensions, a degree of disorder at the nanoscale is required. It has been shown for instance that osteoprogenitor cells on PMMA with ordered nanopits of 120 nm diameter did not express osteopontin or osteocalcin after 21 days while osteoprogenitor cells on PMMA with non-ordered nanopits of same diameter did express osteopontin and osteocalcin after the same period of time (Fig. 1.21). Regarding the expression of those two proteins, pillar-like nanostructures with dimensions of 15, 55 and 100 nm on titanium surfaces have also been found to increase OPN and OCN expression after 21 days as compared to flat titanium surfaces [45].

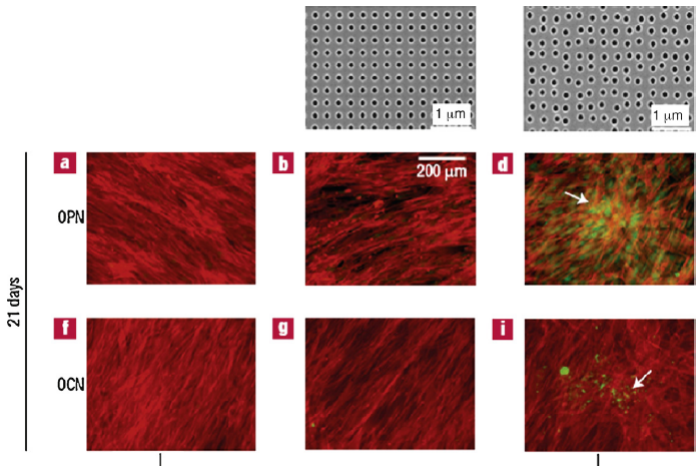


Figure 1.21: The effect of ordered and non-ordered nanopits on osteopontin (OPN) and osteocalcin (OCN) expression by osteoprogenitor cells after 21 days stained with alizarin red. PMMA surfaces produced by e-beam lithography with ordered (top row left) and non-ordered (top row right) nanopits of 120 nm diameter. Osteoprogenitor cells on control surfaces and on surfaces with ordered nanopits did not express OPN (a and b) or OCN (f and g) whereas osteoprogenitor cells on surfaces with non-ordered nanopits were positive for OPN and OCN (d and i). Reproduced from Lord et al. (2010) [45].

1.3.2.3 Effect of nanoscale topography on MC3T3-E1 cellular response

Several studies have investigated the effect of nanotopography on MC3T3-E1 cellular response. Six of them, which dealt with nanofibers, nanowires, nanoscale particles, nanoripples and nanopores, are presented below.

Three interesting studies investigated the effect of nanofibers and nanowires on MC3T3-E1 cells. First, in 2006, Badami et al. [63] studied the effect of fiber diameter on MC3T3-E1 cells. MC3T3-E1 cells were cultured for 14 days on electrospun fibers of poly(ethylene glycol)-poly(lactic acid) (PEG-PLA) copolymers of mean diameter of 0.14-2.1 μm. After the 14 days of culture, it was observed that cell density increased with fiber diameter. Compared with cells cultured on smooth surfaces, cells on electrospun fibers had a smaller projected area. However, cells on 2.1 μm diameter fibers exhibited a higher aspect ratio and extended lamellipodia along individual fibers. Therefore, the authors concluded that surface topography introduced by 0.14-21 μm diameter electrospun fibers affects cell morphology and proliferation [63].

Then, in 2016, He et al. [60] studied the effect of polypyrrole nanowires and electrical stimulation (ES) on MC3T3-E1 cell functions. They cultured MC3T3-E1 cells for 21 days on pure PPy nanowires surface (PPy NWs) polymerized on titanium surface, on PPy with normal cauliflower-like morphology (ca-PPy) polymerized on titanium surface (Fig. 1.22) and on bare titanium (Ti), in the three cases with and without electrical stimulation. Cell proliferation was higher on PPy NWs coated surfaces than on the two other surfaces which indicates the good osteoconductivity of PPy NWs coating (Fig.1.23) [60]. Electrical stimulation further improved cell proliferation on all surfaces. The coating also affected the morphology of M3T3-E1 cells. After 12h, most of the cells on Ti surface were shrinking, the degree of cell extension was low and there were few pseudopods (Fig. 1.24-A). In contrast, cells on surfaces coated with PPy displayed a polygonal morphology, appeared to be flatter and possessed more pseudopods (Fig.1.24-B,C) [60]. Furthermore, PPy NWs enhanced ALP synthesis and calcium deposition [60].

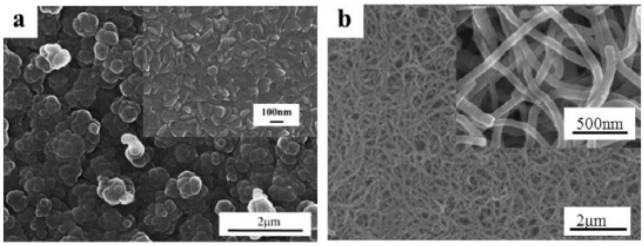


Figure 1.22: SEM images of (a) PPy with cauliflower-like morphology (ca-PPy) coating on Ti surface (b) PPy nanowires coating on Ti surface. Reproduced from He et al. (2016) [60].

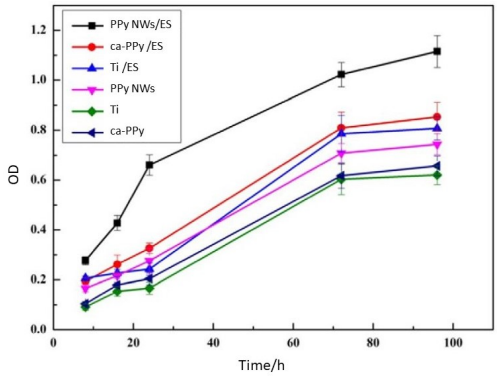


Figure 1.23: MC3T3-E1 cells proliferation (MTT assay) for bare Ti, Ti coated with cauliflower-like PPy (ca-PPy) and Ti coated with PPy nanowires (PPy NWs) without and with electrical stimulation (ES). Reproduced from He et al. (2016) [60].

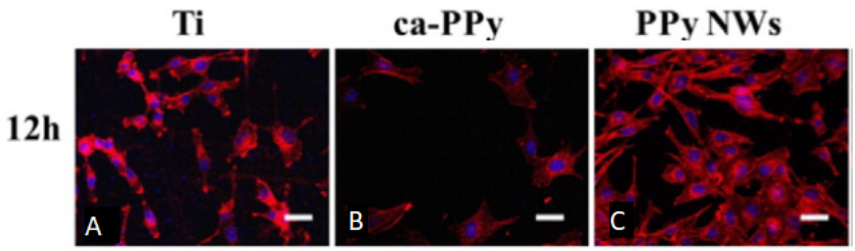


Figure 1.24: Fluorescence images of MC3T3-E1 actin fibers stained with Rhodamine Phalloidin (red) and nuclei stained with Hoechst 33258 (blue) after 12 hours of culture on (A) Ti surface, (B) ca-PPy surface and (C) PPy NWs surface. Adapted from He et al. (2016) [60].

Finally, in 2017, Ming et al. [64] showed the effect of nanowires on titanium surfaces on the cellular response of MC3T3-E1 cells. The cells were cultured on sandblasted and acid-etched (SLA) titanium surfaces and nanowires modified titanium surface (Ti-NW) prepared via acid etching and hydrothermal treatment with a NaOH solution (Fig. 1.25). After 8 hours of culture, cells spread more evenly across Ti-NW surfaces and extended more pseudopodia than cells on Ti-SLA surfaces (Fig. 1.26). After 3 and 6 days of culture, cell proliferation was significantly higher on Ti-NW surfaces than on Ti-SLA surface. Furthermore, after 14 days of culture, ALP activity was significantly higher for Ti-NW surfaces than for Ti-SLA surfaces. Therefore, it was shown in this study that the nanowires structure promoted cell spreading, cell proliferation and osteogenic differentiation of MC3T3-E1 cells [64].

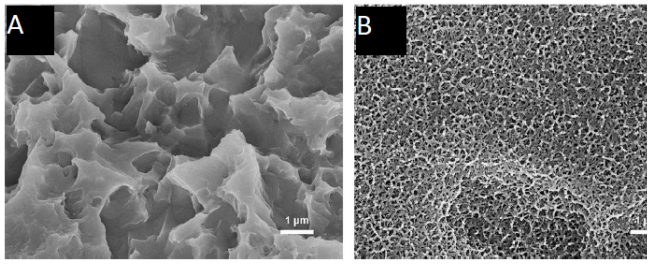


Figure 1.25: SEM images (magnification 10 000x, scale-bar= 1 μm) of (A) Ti-SLA surface and (B) Ti-NW surface. Adapted from Ming et al. (2017) [64].

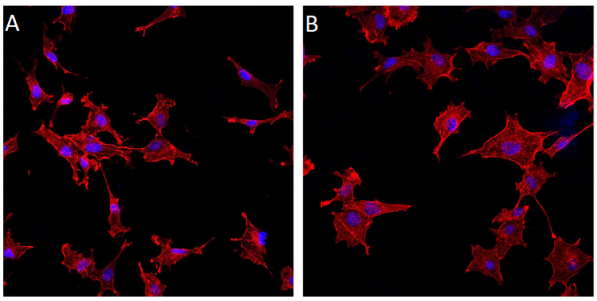


Figure 1.26: Fluorescence images of MC3T3-E1 cells after 8h of incubation (magnification 200x) on (A) Ti-SLA surface and (B) Ti-NW surface. Adapted from Ming et al. (2017) [64].

These three studies together show that nanofibers and nanowires can favorably affect cell morphology, formation of lamellipodia, cell spreading and proliferation and osteoblastic differentiation. Furthermore, there exist optimal dimensions for those nanofeatures.

In 2013, Tamjid et al. [65] compared the effect of the addition of nanoscale particles on 2D and 3D scaffolds on the cellular response of MC3T3-E1 cells. The 2D scaffolds consisted in films of PCL while the 3D scaffolds consisted in porous interconnected 3D-printed structure of PCL with macro-(400-500 μm) and micro-(~25 μm) porosity. The added nanoscale particles were TiO_2 and bioactive glass particles. Cell differentiation was assessed by the ALP activity after 7, 14 and 21 days. Cell differentiation was remarkably higher in 3D scaffolds than in 2D films. Interestingly, the effect of nanoscale topography was found to be different for 2D and 3D structures. Indeed, the addition of nanoparticles in the structures increased cell proliferation in the 2D structures whereas it did not have much influence on the 3D structures. Furthermore, the effect of the addition of nanoparticles on cell differentiation was more visible for 2D scaffolds than for 3D scaffolds [65]. Therefore, this shows that modification of the nanotopography may not affect the cellular response in the same way when it comes from 2D or 3D scaffolds.

In 2017, Chen et al. [66] studied the effect of periodic micro/nanometer-scale grooves on titanium surfaces on the cellular response of MC3T3-E1 cells. The MC3T3-E1 cells were cultured on titanium surfaces with periodic micrometer-scale grooves (mTi) and on titanium surfaces with periodic micrometer-scale grooves containing nanometer-scale ripples in the vertical direction made by femtosecond laser irradiation (fsTi) (Fig. 1.27). After 6-hours of culture, cells on mTi surfaces showed a wider distribution of areas and a rounder morphology whereas cells on the fsTi surfaces displayed a higher aspect ratio and were more aligned (Fig. 1.28). After 5 days of incubation, cellular proliferation was found to be significantly lower on fsTi surfaces than on mTi surfaces. Regarding, the differentiation capacities, after 7 days of culture, along with other markers of osteoblastic differentiation, the total amount of calcified deposits was larger on fsTi surfaces than on mTi surfaces. Therefore, this study concluded that the nanoscale ripples topography contained in the microgrooves increased osteogenic differentiation and calcification of preosteoblastic cells while decreasing the cellular proliferation. This increase in cellular differentiation and decrease in cellular proliferation may be due to the regular interrelationship between proliferation and differentiation of the osteoblast phenotype [66].

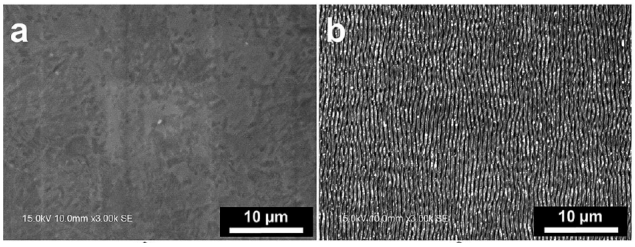


Figure 1.27: SEM images of (a) mTi surface and (b) fsTi surface. Adapted from Chen et al. (2017) [66].

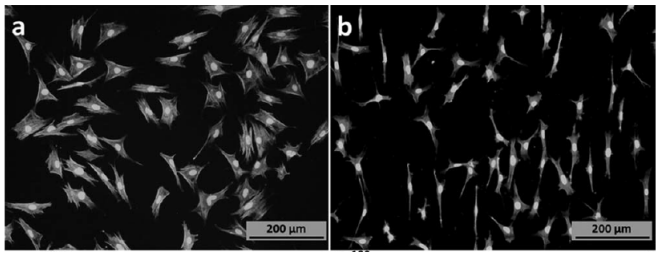


Figure 1.28: Confocal microscopy images of the morphology of MC3T3-E1 cells after 6-hours incubation on (a) mTi and (b) fsTi surfaces. F-actin and nuclei of the cells were stained respectively with rhodamine-phalloidin and 4',6-diamidino-2-phenylindole. Adapted from Chen et al. (2017) [66].

In 2018, Mussano et al. [47] studied the effect of nanopores on alumina surfaces on cellular response of MC3T3-E1 cells. Cells were cultured on standard plastic culture dishes and on two alumina surfaces on which nanopores were generated by oxidative anodization. On the first alumina surface the pore diameter range was 16-30 nm while on the second the pore diameter range was 65-89 nm (Fig. 1.29). After 24 hours of culture, cells on the nanoporous alumina surfaces displayed a very high number of filopodia and ramification compared to cells on standard culture plastic dishes (Fig. 1.30) [47]. Compared to the standard culture plastic dish, cell adhesion, cell viability and focal adhesion density (i.e. the number of focal adhesions per surface unit), and osteogenic differentiation (assessed by ALP activity at 7 days and calcium deposition at 21 days) were higher on nanoporous alumina surfaces. Furthermore, both ALP activity and calcium deposition were higher for the cells seeded on the nanoporous alumina surface with pore diameter range of 65-89 nm than on the one with pore diameter range of 16-30 nm. Therefore, this shows that nanoscale features can promote osteogenic differentiation and that there is an optimal dimension for these features.

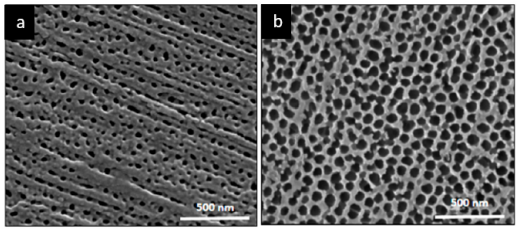


Figure 1.29: Field Emission Scanning Electron Microscope analysis of alumina surfaces with pore diameter range (a) 16-30 nm (b) 65-89 nm. Adapted from Mussano et al. (2018) [47].

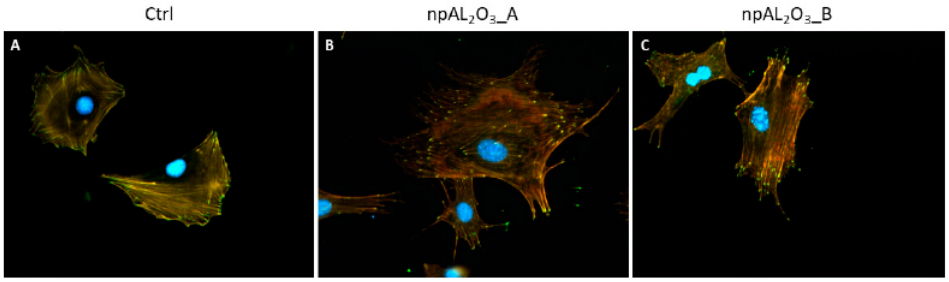


Figure 1.30: Fluorescence photomicrographs (magnification 200x) of MC3T3-E1 cells after 24 hours of culture on (A) standard culture dish plastic (Ctrl), (B) alumina surface with nanopores of diameter range 16-30 nm (npAL_2O_3A) and (C) alumina surface with nanopores of diameter range 65-89 nm. Adapted from Mussano et al. (2018) [47].

From the studies presented in this section, the following conclusions can be drawn. Various nanotopographical features, namely nanofibers, nanowires, nanoparticles, nanoripples and nanopores, can be used to affect the cell morphology and orientation and to increase or decrease cell proliferation and osteogenic differentiation of MC3T3-E1 cells. Furthermore, optimal dimensions seem to exist for these different nanoscale features. Finally, effects of nanofeatures on 2D structures on MC3T3-E1 cells do not always induce the same effect when used on 3D structures.

1.3.3 ECM surface coatings to control cellular functions

In addition to structural cues, the ECM also provides crucial biochemical cues regulating cell functions such as adhesion, migration, proliferation and differentiation. Indeed, macromolecules composing the ECM can be recognized by cell membrane receptors, inducing specific cellular behavior [67]. This understanding of the role of the ECM components in cell fate has motivated their use in tissue engineering to make biomimetic scaffolds which imitate the chemical environment of native ECMs [67]. Besides the tailoring of the nanotopography, the introduction of ECM molecules in tissue engineering scaffolds is, therefore, a promising approach to direct cell behavior towards a desired state [67]. However, scaffolds made entirely from ECM molecules often present insufficient mechanical strength [67]. Therefore, surface modification of synthetic biomaterials with ECM components has been widely investigated as a means to improve their biocompatibility and bioactivity.

First, the main interactions between native ECM and cells *in vivo*, which are important to understand how biomimetic ECM coatings can impact cellular behavior, will be briefly described. Then, the two main approaches investigated for surface biofunctionalization, i.e. the adsorption of full-length ECM components and the grafting of short binding peptides, will be presented. Next, the focus will be put on the first approach, which is the one that was implemented in this thesis. In particular, cell interactions with simple collagen and simple hyaluronan coatings will be reviewed, before finally considering cell interactions with multilayered LbL coatings made from ECM components.

1.3.3.1 ECM-cell interactions *in vivo*

In order to understand how surfaces modified with ECM components can impact cell function, one must first understand the interactions between cells and ECM macromolecules *in vivo* and how those interactions can trigger specific cell behavior. *In vivo*, every cell is surrounded by the ECM. The ECM is in fact a complex network of macromolecules (collagens, fibronectin, elastin or fibrillin) with entrapped proteoglycans and glycoproteins [68]. The composition of the ECM is highly complex and tissue-specific [68]. As already mentioned, the ECM provides structural and mechanical support to the cells but also, through its composition, biochemical cues that are crucial in the regulation of cell behavior [68].

ECM macromolecules present binding epitopes, or peptide sequences, that can be specifically recognized by receptors present on cell membranes. The largest family of cell membrane receptors involved in the recognition of biochemical cues from the ECM is the integrins [6]. Integrins are $\alpha - \beta$ heterodimeric transmembrane receptors which have the ability to bind both extracellular ligands from the ECM and intracellular ligands [67]. The extracellular side is involved in the recognition of specific binding epitopes present on ECM macromolecules [67]. The intracellular side, on the other hand, is involved in intracellular signaling pathways [67, 68]. Activation of the integrin by binding of an extracellular ligand induces a change of conformation that allows the binding of various proteins on its intracellular domain, such as the cytoskeleton-binding talin (Fig. 1.31) [67, 68]. This way, recognition of ECM binding-epitopes by the integrins transmits signals inside the cell that induces specific behavior, such as cytoskeleton reorganization, adhesion, proliferation and differentiation [67, 68].

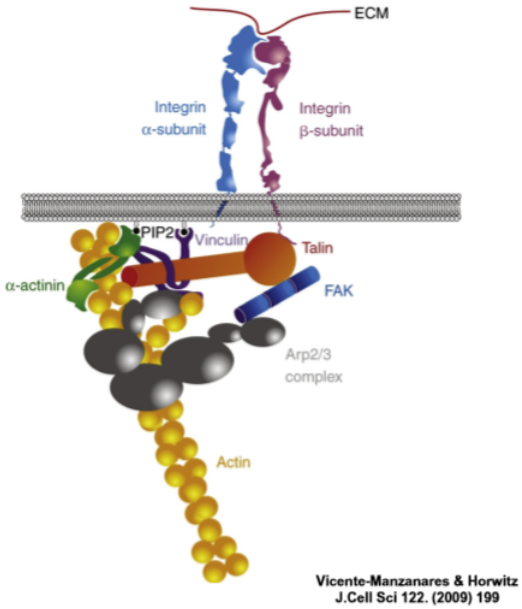


Figure 1.31: Transmembrane linkage between ECM macromolecule and actin cytoskeleton mediated by an integrin receptor. The cytoplasmic domain of the integrin can bind to talin which itself binds to actin. The formed complex is stabilised by other proteins (vinculin, alpha-actinin, etc.) [68].

Despite a detailed knowledge of the structure of integrin receptors and of the main adhesive proteins of the ECM (fibronectins, collagens and laminin), the exact mechanisms by which integrins recognize specific epitopes on these molecules is still not known, except for two particular adhesive peptide sequences, RGD and GFOGER [68]. The RGD (Arg-Gly-Asp) sequence was the first cell adhesive epitope that was discovered [68]. Known as a universal binding sequence, it is found on many ECM adhesive proteins, including fibronectin, vitronectin and osteopontin. This sequence is the most widely used for biomaterial surface modification. RGD-modified surfaces have been shown to improve the adhesion of many cell types, including fibroblasts, stem cells, endothelial cells, neural cells and osteoblasts [59, 67]. GFOGER is a triple-helical cell-binding epitope found in collagens (type I, II and III) [68]. Studies on these cell-binding epitopes have shown that recognition by integrins depends not only on the presence and the sequenced order of the amino-acids themselves but also on the three-dimensional conformation of the sequence, their spatial orientation and their density in the ECM [67]. Therefore, the cellular response on biomimetic surfaces depends not only on the presence of binding epitopes but also on their density and spatial arrangement [68].

1.3.3.2 Main approaches for biological surface modification

Two main approaches have been investigated to biofunctionalize tissue engineering scaffold surfaces: the adsorption of entire ECM-components on the surface or the covalent grafting of specific binding peptide sequences [67]. The first approach is simple and straightforward. Coatings of various ECM components involved in cell adhesion have been achieved with this method [6]. The most used ECM macromolecules for biomimetic coatings are collagens (type I, II and III), elastin, fibronectin, hyaluronan and chondroitin-sulfate [68]. Due to their adhesiveness, these proteins adsorb easily on the surface of almost any type of biomaterial (polymers, metals and ceramics) [6]. Nonetheless, these coatings may pose issues of stability. Also, proteins may

undergo change of conformation upon adsorption susceptible to denature or hide binding epitopes to the cells [6]. To overcome the limitations of the first approach, grafting of small peptides containing the cell-binding sequences present in native ECM proteins have been investigated. The mostly used ECM-derived peptides used for this purpose is the RGD sequence [68]. Peptides containing the RGD sequence have been successfully covalently grafted to various polymeric substrate, including polypyrrole as explained in section 1.3.1.4. The advantage of using small peptides is that the density of presented cell-binding epitopes can be more precisely controlled than with adsorption of full-length ECM-molecules. Much higher densities of binding epitopes can be achieved. This approach also offers the possibility to arrange the epitopes into nanoscale patterns [6]. However, because of the complexity of the ligand-receptor interactions, results reported in the literature using this approach tend to lack consistency [67].

Despite offering less control on the presentation of the binding epitopes, adsorption of full-length ECM molecules constitutes a simple and straightforward approach [67]. Moreover, alternate adsorption of oppositely charged ECM macromolecules leads to the formation of multilayered LbL coatings. As shown in section 1.1.2, LbL films present the advantage that their structure and properties can easily be tailored, thus offering the possibility to control cellular behavior through the adjustment of those properties [11].

1.3.3.3 Cell interactions with collagen type I coatings

Collagen type I is one of the most abundant ECM components, especially in connective tissues such as bone, skin or tendons [68]. Collagen type I molecules can self-assemble to form fibrils of high tensile strength [68]. Therefore, collagen contributes to the stiffness and mechanical strength of the tissue. Aside from their structural role, collagens are specific ligands to several receptors of the integrin family [11]. Collagen-coated surfaces have been shown to support the attachment, spreading and proliferation of most cell types independently of the nature of the underlying substrate as long as it is non-toxic and able to adsorb collagen [68]. Good cell adhesion and proliferation were observed both on native collagen coatings, in which collagen molecules keep their triple-helical conformation, and on denatured collagen coatings, in which collagen molecules have a random coil conformation [68]. Moreover, collagen coatings have also been shown to promote adsorption of fibronectin present in the serum, thus further improving cell attachment [68].

As collagen type I constitutes 95% of the organic phase of bone tissue, it has been widely investigated for bone tissue engineering applications [49, 69]. Indeed, studies have shown that collagen type I promotes osteogenic differentiation. Collagen type I is also able to initiate and control mineralization of bone tissue thanks to a collagen/apatite self-assembly process [3, 49]. Because of its osteoconductive properties, it has thus been widely considered as a coating to improve the osteointegration of orthopaedic implants for instance [49]. Geissler et al. studied the adhesion of rat calvarial osteoblastic cells on titanium surfaces coated with adsorbed collagen type I either fibrillar or monomeric [70]. They discovered that the coated surface accelerates the early attachment of osteoblasts compared to the bare Ti controls [70]. Collagen coatings were found to promote cell spreading and formation of filopodia [70]. van den Dolder and Jansen also studied the effect of collagen type I coated titanium surface on rat bone marrow cells [71]. After 8 and 24 days of culture in osteogenic medium, an increased calcium deposition was reported for cells cultured on adsorbed collagen I coatings compared to the bare Ti control, thus showing an enhanced osteogenic differentiation [71]. In addition, the arrangement of collagen into 3D structures has been shown to induce cellular behaviors different than on planar substrates [6]. Indeed, a 3D structured scaffold provides the cells with an environment closer to their *in vivo* environment [8]. For instance, Matthews et al. cultured MC3T3-E1 and rat preosteoblastic cells on 3D collagen gels and on planar collagen-coated dishes [72]. von Kossa staining showed

accelerated mineralization of the ECM of MC3T3-E1 cells cultured on 3D collagen gels compared to cells cultured on 2D planar collagen dishes [72]. Compared to planar collagen substrates, primary rat osteoblasts cultured on the 3D collagen gels showed an increased and earlier expression of several osteoblast marker genes, including the genes for osteocalcin, alkaline phosphatase and bone sialoprotein [72]. These results indicate that combining collagen with a 3D-structured scaffold can potentially further enhance osteogenic differentiation than simple planar collagen coatings.

1.3.3.4 Cell interactions with hyaluronic acid coatings

Hyaluronic acid (HA), also called hyaluronan, is a glycosaminoglycan that plays an important role in cell adhesion, migration and proliferation [73]. It is a polyanionic multifunctional polymer and a component of the ECM of many cells including osteoblasts [74]. In the bone matrix, in addition to its structural role, HA regulates cell adhesion, proliferation, migration, wound healing and expression of osteoinductive factors such as ALP [74]. Furthermore, its anionic and hydrophilic nature prevents bacterial adhesion when coated on a surface [74]. However, HA-coating is not sufficient to completely avoid infection [74]. Several studies have investigated the effect of hyaluronan coatings on osteoblast behavior.

In 2017, Agarwal et al. [74] studied the effect of the coating of hyaluronic acid on the surface of AZ31 Mg alloy on the cellular response of MC3T3-E1 cells. MC3T3-E1 cells were cultured on AZ31 Mg alloy sheets (AZ31) and on AZ31 Mg alloy sheets coated with hyaluronic acid (AZ31-HA). After 24h of incubation, preosteoblasts attached on uncoated AZ31 were sparse and circular which demonstrates a poor cellular adhesion to the substrate (Fig. 1.32a). Furthermore, no strong actin filament staining was observed which confirms the poor cellular adhesion and shows that the cells did not develop a filamentous actin cytoskeleton (Fig. 1.33a). In contrast, the preosteoblasts adherent to the AZ31-HA substrate demonstrated flattened, extended morphology and greater cell-to-cell interaction (Fig. 1.32b). Moreover, the cells appeared cuboidal in morphology and showed strong acting filament organization extending in different directions which is indicative of an osteoblast phenotype (Fig.1.33) [74]. Cell proliferation, assessed by DNA quantification, was significantly higher for the cells cultured on AZ31-HA than on AZ31 for all durations (i.e. 3, 7 and 14 days). Osteoblast differentiation, assessed by ALP activity was significantly higher for the cells cultured on AZ31-HA than for those on AZ31 for all durations (i.e. 3, 7 and 14 days). Therefore, the authors concluded that the HA-coating improved cellular adhesion, proliferation and differentiation as compared to the bare AZ31 surface.

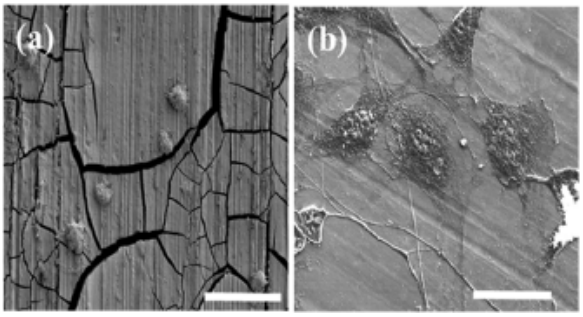


Figure 1.32: SEM images (scale bar is 50 μm) of MC3T3-E1 cells cultured on AZ31 Mg alloy (a) and AZ-31 Mg alloy coated with hyaluronic acid (b) Adapted from Agarwal et al. (2017) [74].

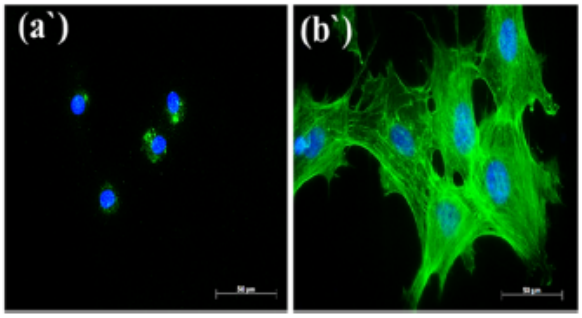


Figure 1.33: Fluorescent images of the actin cytoskeleton and nuclei of MC3T3-E1 cells cultured on (a) and AZ-31 Mg alloy coated with hyaluronic acid (b). Actin cytoskeleton was stained with Phalloidin (green) and nuclei were obtained with DAPI (blue) Adapted from Agarwal et al. (2017) [74].

In 2010, Seo et al. [73] investigated the effect of immobilization of hyaluronic acid onto - NH_2

functionalized anodized titanium surface on the proliferation of MC3T3-E1 cells. To do so, they cultured MC3T3-E1 cells on titanium surface (Ti), anodized Ti surface, anodized Ti surface functionalized with - NH_2 (Ti/NH_2) and anodized Ti surface functionalized with - NH_2 and with immobilized HA (Ti/NH_2/HA surface). After 6 days of culture, the cell proliferation on the Ti/NH2/HA surface increased by approximately 80% compared to the Ti surface, while the cell proliferation on simply anodized Ti surfaces and Ti/NH_2 surfaces were similar to cell proliferation on Ti surface. The authors concluded that the presence of HA enhances the cellular proliferation of MC3T3-E1 cells.

In 2011, Mathews et al. [75] studied the effect of collagen type I, chitosan and hyaluronic acid on osteogenic differentiation of human bone marrow derived mesenchymal stem cells (hMSCs). The cells were cultured on bare tissue culture plates, tissue culture plates coated with either chitosan, collagen type I or hyaluronic acid. The osteogenic differentiation was assessed by the calcium deposition. After 14 days of culture, Alizarin Red S staining revealed a significantly higher mineralization in the HA-coated plates than in all other plates. After 21 days of culture, von Kossa staining showed a relatively higher mineral deposition than in the other plates. Finally, the amount of calcium in the secreted mineral matrix quantified by the o-cresolphthalein complexone method showed that the HA-coating significantly improved the calcium deposition whereas there was no significant difference among the untreated plate and the plates coated with chitosan and collagen type I [75]. Therefore, this paper showed that HA-coating improves the mineralization of the ECM.

In 2008, Chua et al. [76] studied the effect of hyaluronic acid and chitosan on the cellular response of MC3T3-E1 cells. The cells were cultured on pristine Ti surface, pristine Ti coated by LbL with polyelectrolyte multilayers of hyaluronic acid and chitosan (PEM-functionalized Ti) and on pristine Ti surface functionalized with dopamine and then independently grafted with HA (Ti-Dop-HA) and CHI (Ti-Dop-CHI). After 4h of incubation, the number of adherent cells on Ti-Dop-HA surface was significantly lower than on pristine Ti while the number of adherent cells on Ti-Dop-CHI was significantly higher than on pristine Ti. For the PEM-functionalized Ti surfaces, the cellular adhesion after 48h was higher when the outer layer was made of CHI than when it was made of HA. However, in both cases, the cellular adhesion was lower than on pristine Ti surface. The authors concluded therefore that HA has a negative effect on cellular adhesion.

From the studies presented above, it appears that the beneficial or detrimental effect of HA on cellular adhesion depends on the surface onto which it is coated. However, it seems to promote osteoblastic differentiation as assessed by ALP activity and calcium deposition.

1.3.3.5 Cell interactions with LbL films

As seen in the previous sections, the incorporation of cell-binding ECM macromolecules, such as collagens and HA, in surface coatings can promote cell proliferation and differentiation. Nonetheless, the coatings reviewed in the previous sections present the disadvantage that parameters such as thickness, porosity, stiffness or surface charge cannot be easily adjusted [77]. LbL assembly, whose principle was described in section 1.1.2, has emerged as an easy technique allowing the production of coatings from ECM molecules with a good control on the structure and properties of the obtained coatings [29].

Indeed, studies on LbL coatings have shown their ability to control cellular function not only by the incorporation of ECM molecules but also through the adjustment of their physicochemical properties [12, 29]. The main properties that have been shown to impact cellular behavior are the surface charge and hydrophilicity of the film, as well as its thickness and its stiffness [11, 29]. First, the surface charge, determined by the terminal layer, has been shown to influence strongly the

binding force between the cells and the film [29]. As most mammalian cells bear predominantly anionic species in their membrane, cells tend to adhere more easily on surfaces bearing positive charges [29]. The surface charge also affects protein adsorption and, through that, cell adhesion [11]. Hydrophillicity has also been shown to be an important parameter affecting cellular function [11]. Indeed, ECM proteins cannot bind on highly hydrophilic surfaces [29]. On the other hand, if the surface is too hydrophobic they tend to adsorb in a conformational state that can be unsuitable for cell binding, thus impeding cell adhesion as well [29]. Generally, the optimum range of hydrophilicity for cell adhesion is reported as between 60°and 80°of water contact angle [29]. As the terminal layer of the LbL film determines its surface charge and surface hydrophilicity, it can have a strong impact on cell behavior and should therefore be chosen appropriately [29].

The film's mechanical properties have also proven to be a crucial factor in the control of cell processes [11, 12]. Indeed, cells possess receptors acting as mechanotransducers and can therefore interact with the ECM via mechanical stimuli [11]. Studies have shown that soft and highly hydrated LbL films tend to impede cell adhesion and proliferation [11]. Unfortunately, LbL assembly of natural polymers, especially highly hydrated polysaccharides, usually yields soft gel-like films [11, 12]. Such films are thus initially not favorable for cell adhesion [11, 12]. For instance, osteoblasts exhibited poor adhesion on poly(L-lysine) (PLL)/HA, CHI/HA, PLL/ALG and PLL/poly(L-glutamic acid) (PGA) films [26]. A first solution to improve cell adhesion on polyaminoacid and polysaccharide LbL coatings is to make thin films by depositing only a small number of layers (typically less than 6) on a stiff surface [12]. Alternatively, several strategies have been developed to modulate the mechanical properties of soft LbL films, including chemical or photo-crosslinking and the incorporation of particles or stiff layers of synthetic polyelectrolyte in the film [11]. Among those, chemical crosslinking has proven an efficient and reliable technique to adjust the stiffness of the film [11]. Many polysaccharide films mentioned above, which were non-adhesive in their native form, were found to become cell adhesive upon cross-linking by means of carbodiimide chemistry (described in section 1.1.2) [12]. Crosslinking was also shown to promote other cell functions than adhesion. For example, crosslinked PLL/CS films showed enhanced adhesion, proliferation and differentiation of MC3T3 cells compared to the unmodified films [78].

Therefore, cell response on LbL films depends on multiple factors: the macromolecules used to build the film and the physicochemical properties of the film [11]. In some cases, the presence of biochemical signals from ECM molecules is able to compensate for physicochemical properties initially unfavorable to cell adhesion [11]. In other cases, the physical properties of the film are more important than the presence of adsorbed ECM molecules [11]. The response has also been shown to depend highly on cell type. For this reason, cell interactions with LbL films are difficult to generalize and should be studied on a case to case basis [11].

1.3.3.6 Cell interactions with COL/HA LbL films

Despite the numerous studies investigating the effects of LbL films made from ECM components on cell function, very few concern films assembled from both collagen type I (COL) and hyaluronan (HA), which are studied in this thesis.

In 2005, Zhang and coworkers first studied the interactions between HA/COL films with cells [77]. The films were built up at pH 4 on glass slides with a preliminary adsorbed layer of poly(ethylenimine) (PEI). At this pH value, COL is positively charged since its pI is of about 5.5 and HA, with a pI of about 2.5, bears negative charges [77]. Prior to cellular tests, the film build-up and surface topography were characterized. As expected, during build-up, the ζ-potential, characterizing the surface charge, was shown to alternate between positive when COL is the last layer and negative when it is HA [77]. The film thickness was demonstrated

to increase linearly with the number of deposited layers [77]. AFM images of COL terminated films (Fig. 1.34) showed a uniform and dense fiber network covering the entire surface of the substrate [77]. This fiber-like structure is completely different from the structure usually observed with synthetic LbL films, made of round aggregates. This peculiar surface topography is due to the assembly of the adsorbed collagen molecules into fibrils [77]. The diameters of the fibers were found to increase when the number of deposition steps increased. This suggests that new collagen molecules are able to adsorb along the previously formed fibers which are coated with HA from the previous deposition step [77].

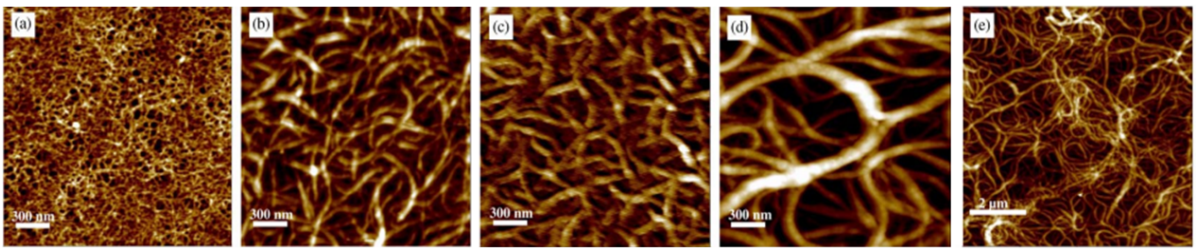


Figure 1.34: AFM height mode images of HA/COL films with a COL terminal layer. (a) simple collagen adsorbed layer. The surface is covered with thin fibers (20-30 nm width). (b) PEI/$(HA/COL)_1$. A network of long (from 1 to several μm long) and large (70-100 nm width) fibers strongly entangled (c) PEI/$(HA/COL)_5$. The fibers width now ranges up to 140 nm. (d-e) PEI/$(HA/COL)_{122}$. The height scale (z) goes from 0 to 4 nm (image a), 0 to 20 nm (images b and c) and from 0 to 50 nm (images d and e). The images were acquired in aqueous conditions (pH 4). Images (a)-(b)-(c)-(d) cover a surface of 2x2 μm and image (e) a surface of 8x8 μm. Reproduced from Zhang et al. (2005) [77].

Zhang et al. then cultured chondrosarcoma (HCS-2/8) cells on the (HA/COL) films [77]. Cells were cultured on $(HA/COL)_5$ and $(HA/COL)_5$/HA to assess the influence of the terminal layer [77]. As seen in the previous section, HA containing films have been reported to inhibit cell adhesion due to their mechanical softness. Nonetheless, $(HA/COL)_5$ films showed good cell adhesion and spreading, probably because the collagen fibrous-network contributes to rigidify the coating [77]. AFM images of cells cultured on the COL ending films showed the presence of pseudopods as well as collagen fibers emerging from the cells. Those collagen fibers emerging and spreading around the cells were identified by the authors as native collagen fibers synthesized by the cells [77]. On the other hand, cells cultured on HA terminated films presented no pseudopods and no native collagen even after 2 days of culture [77]. Thus, these results suggest that a COL terminating layer enhances cell adhesion while a HA terminating layer impedes it [77].

As reported in section 1.3.3.3, collagen coatings have been shown to promote the adhesion of osteoblastic cells and matrix mineralization. Therefore, Li et al. in 2012 studied the responses of preosteoblastic cells to HA/COL LbL coatings to assess their suitability for the biofunctionalization of orthopedic implants [30]. MC3T3-E1 cells were cultured on three types of substrates: bare smooth titanium (SM-Ti), bare acid-etched titanium (AE-Ti) and titanium coated with an ultrathin $(COL/HA)_4$/COL LbL films (CHC-Ti) [30].

Cell morphology after 1, 3 and 24 hours of culture on the three substrates was assessed by fluorescence microscopy (Fig. 1.35). Cells attached on all three substrates and spread on all three systems after 3 hours of culture [30]. Nonetheless, the cells cultured on the (HA/COL)-coating (CHC-Ti) exhibited more elongated morphology and showed more cellular extensions than those cultured on the bare titanium, both SM-Ti and AE-Ti, thus confirming a better cell spreading on the (HA/COL)-coated surfaces [30]. Cell proliferation was then assessed by fluorometric DNA quantification after 4, 7 and 14 days of culture [30]. After 4 days, no significant difference in DNA content was detected. However, after 7 days of culture, the CHC-Ti groups showed a significantly higher DNA content than the other two groups, indicating that the coating enhanced cell proliferation [30]. At 14 days of culture, DNA content reached a plateau, as no more space was available on the surface for cell proliferation [30].

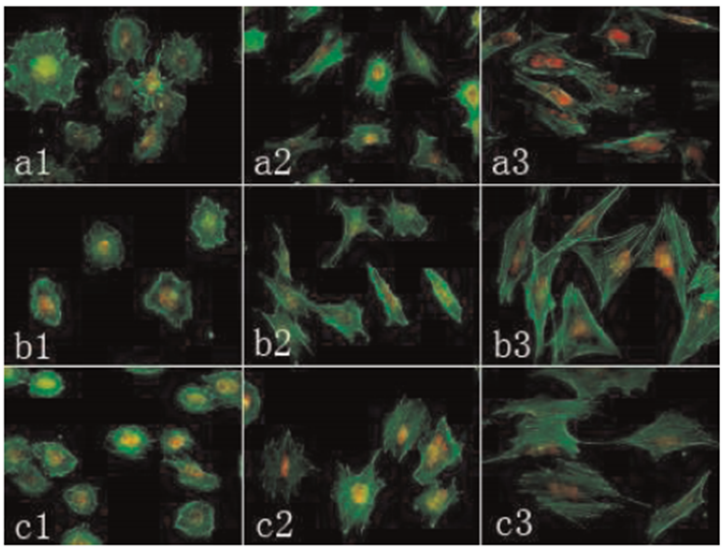


Figure 1.35: Fluorescence image of MC3T3-E1 cells cultured on CHC-Ti (a),SM-Ti (b) and AE-Ti (c). (a1-b1-c1) After 1 hour of culture. (a2-b2-c2) after 3 hours of culture. (a3-b3-c3) after 24 hours of culture. The actin cytoskeleton was stained with FITC phalloidin (green). The nuclei were stained with propidium iodide (red). Reproduced from Li et al. (2012) [30].

Finally, differentiation of the MC3T3-E1 cells cultured on the three surfaces was evaluated by measuring intracellular ALP activity and osteocalcin release [30]. Figure 1.36 shows the ALP activity normalized by total protein content after 4, 7 and 14 days of culture in osteogenic medium [30]. ALP activity increased with culture time for all three groups. For each considered time, the coated substrate (CHC-Ti) showed an ALP activity significantly higher than the other two substrates [30]. The (HA/COL)-coating therefore accelerates the early phase of osteogenic differentiation. Release of osteocalcin, which is related to matrix mineralization, was measured after 14 days of culture in osteogenic medium (Fig. 1.37) [30]. Osteocalcin level (normalized by total protein) was significantly higher on the coated substrate (CHC-Ti). These results demonstrate that HA/COL LbL coatings can promote proliferation and osteogenic differentiation of preosteoblasts [30].

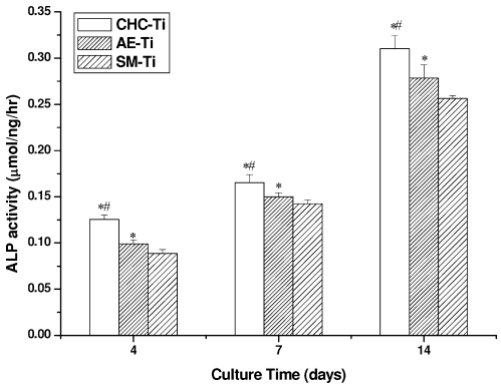


Figure 1.36: Intracellular ALP activity of MC3T3-E1 cells cultured on CHC-Ti, AE-Ti and SM-Ti substrates. The ALP activity is normalized by total protein. The symbol * indicates a statistically significant difference ($p < 0.05$) between CHC-Ti and SM-Ti or between AE-Ti and SM-Ti. The symbol # represents a statistically significant difference between CHC-Ti and AE-Ti. Reproduced from Li et al. (2012) [30].

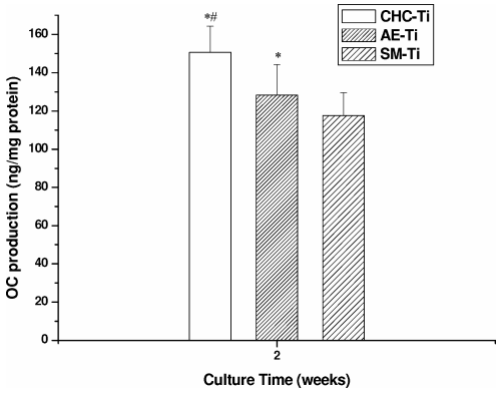


Figure 1.37: Osteocalcin content in the culture medium, normalized by total protein secreted in the culture medium. The symbol * indicates a statistically significant difference ($p < 0.05$) between CHC-Ti and SM-Ti or between AE-Ti and SM-Ti. The symbol # represents a statistically significant difference ($p < 0.05$) between CHC-Ti and AE-Ti. Reproduced from Li et al. (2012) [30].

Chapter 2

Materials and Methods

In this chapter, the materials and methods used in the frame of this thesis will be detailed. First, the elaboration of the polypyrrole (PPy) nanotube frameworks and the assembly of the hyaluronan/collagen (HA/COL) coating by Layer-by-Layer deposition will be described. Conditions of cell culture will then be presented. Finally, the cellular tests performed to assess cell adhesion, proliferation and differentiation on the elaborated biointerfaces will be detailed.

2.1 Elaboration of the PPy nanotube frameworks

2.1.1 Materials

2.1.1.1 Products

Pyrrole extra pure (Py, purity 99%), anhydrous Iron (III) chloride ($FeCl_3$, purity 98%) and 2-(N-morpholino)ethanesulfonic acid monohydrate (MES, purity 99+%) for biochemistry were purchased from Acros Organics. Powder of sodium hydroxide (purity 97%) was obtained from Sigma-Aldrich. Aluminium oxide basic, Brockmann I, for chromatography (50-200μm) was purchased from Acros Organics.

2.1.1.2 Solvents

Ultrapure water was obtained by purification with a Milli-Q system with a resistivity of 18.2 mΩ. Dichloromethane (99.8 +%) stabilized with amylene was purchased from Acros Organics.

2.1.1.3 Templates

Sheets of polycarbonate (PC) track-etched membranes of thickness 25 μm with intersected pores of diameter 40 nm and diameter 300 nm were supplied by it4ip. Intersected pores were obtained by double irradiation with an angle of incidence of 35 and 41°(with respect to the surface normal). The characteristics of both templates are summarized in Table 2.1.

Table 2.1: Characteristics of the PC track-etched templates

Mean pore diameter [nm]	**Thickness [μm]**	**Pore density [cm^{-2}]**	**Irradiation angles of incidence**
300	25	$2.8 \cdot 10^8$	35 and 41°
40	25	$1.2 \cdot 10^{10}$	35 and 41°

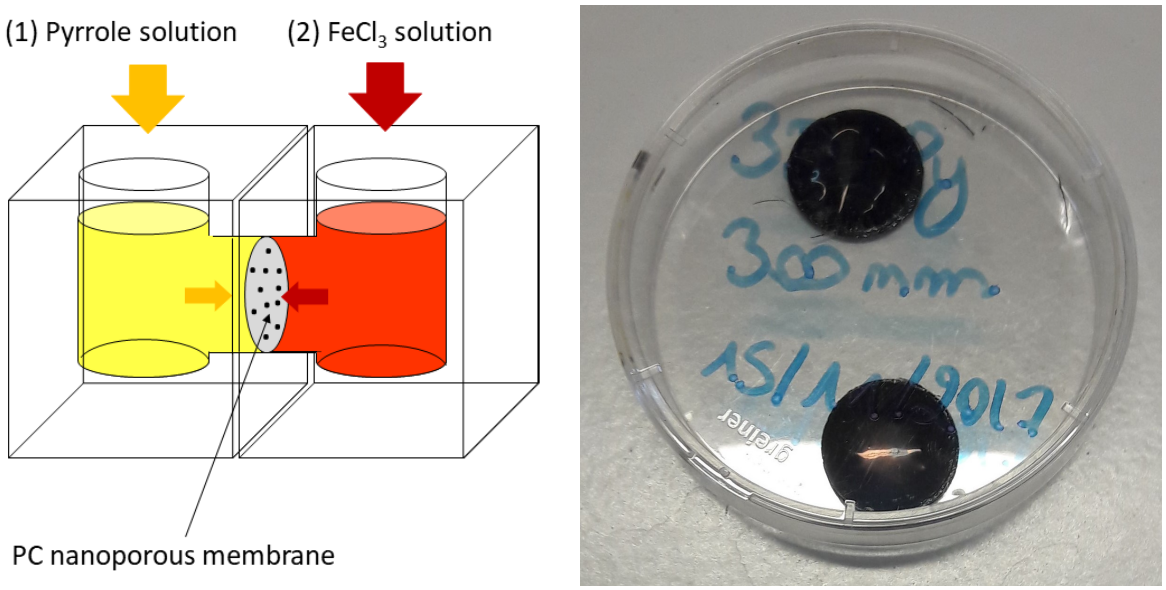
2.1.2 Template synthesis of the nanotube frameworks

Self-standing networks of intersected polypyrrole nanotubes were elaborated by *in situ* chemical polymerization of PPy within the pores of PC track-etched membranes.

Pyrrole was purified prior to the synthesis in order to remove short PPy chains that may have polymerized during storage. This was achieved by performing column chromatography using aluminum oxide particles of 50 to 200 μm of diameter. Iron (III) chloride ($FeCl_3$) was used as the oxidizing agent for the polymerization.

The polymerization was carried out in a 100 mM MES buffer at pH 5.5 prepared beforehand in ultrapure water. A monomer solution of 0.5 M Py and an oxidizing solution of 0.5 M $FeCl_3$ were freshly prepared in the MES buffer and agitated for 20 minutes prior to the polymerization.

For the templated synthesis of polypyrrole, the approach of Duchet et al. using a two-compartment chamber was implemented [18]. The PC track-etched membrane was cut into a circle of 2 cm diameter, which was then placed as a separation between the two compartments (Fig. 2.1(a)). The Py solution was first added in one chamber and allowed to diffuse in the pores of the membrane for 20 minutes. Then, the $FeCl_3$ solution was added to initiate the oxidative polymerization. After 5 minutes, the solutions were removed to stop the polymerization and the template with PPy polymerized in its pores was retrieved and abundantly rinsed with ultrapure water. A picture of two templates at this stage of the templated synthesis is shown in Figure 2.1(b).



(a) (b)

Figure 2.1: (a) Schematic of the templated synthesis of a polypyrrole nanotube framework using a two-compartment polymerization chamber. The nanoporous track-etched PC membrane with intersected pores is placed as a separation between the two compartments. (1) The monomer solution (Py 0.5 M in MES buffer, pH 5.5) is added to the first compartment and allowed to diffuse through the membrane for 20 minutes. (2) The oxidizing solution ($FeCl_3$ 0.5 M in MES buffer, pH 5.5) is added. Polymerization is allowed to proceed for five minutes. (b) Picture of two PC templates with PPy polymerized in their pores at the end of the templated synthesis after being abundantly rinsed with ultrapure water and cut to 1.6 cm diameter.

2.1.3 Template removal

The last step in the elaboration of the PPy nanotube framework is the removal of the PC template to recover the self-standing PPy nanotube framework.

Given that Py polymerization also takes place on the two faces of the PC membrane, forming a crust, decrusting was therefore necessary to obtain a framework of nanotubes with free extremities. To do so, each face was polished mechanically on a polishing pad covered with alumina powder for 2 minutes. Then, dissolution of the template was achieved by pouring 40 mL of dichloromethane dropwise on the substrate.

After template dissolution, the obtained nanotube frameworks were put in the wells of a multi-well plate and stored at 4°C for at least 12 hours prior to the LbL deposition in ultrapure water adapted at pH 4 in order to ensure correct wetting of the frameworks and wash away any remaining dichloromethane from the template dissolution. The pH value of the ultrapure water was adapted beforehand by the dilution of HCl 0.1M.

2.2 LbL assembly of the (HA/COL)-coatings

2.2.1 Materials

2.2.1.1 Solvent

Ultrapure water at pH 4 was used as a solvent and as a rinsing solution. The ultrapure water was obtained by purification with a Milli-Q system with a resistivity of 18.2 mΩ and its pH was adapted to 4 by the dilution of HCl 0.1M purchased from Sigma-Aldrich.

2.2.1.2 Polyelectrolytes

Collagen type-I from bovine calf skin solution (4mg/mL) was obtained from Merck Millipore. Hyaluronan was purchased in the form of dried sodium hyaluronate (HA200, 151-300 kDa) from Lifecore biomedical. The chemical formula of hyaluronan is presented in Figure 2.2.

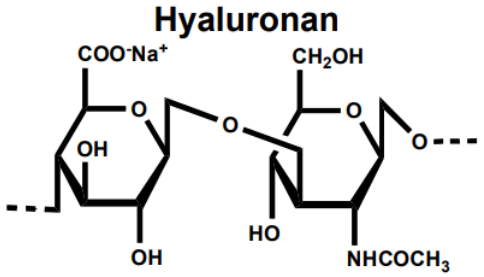


Figure 2.2: Chemical formula of hyaluronan (HA). Reproduced from Picart (2008) [12].

For the LbL deposition, an aqueous solution of 1mg/mL collagen type I and an aqueous solution of 1 mg/mL hyaluronan were used. Both solutions were prepared using ultrapure water at pH 4. At this pH, collagen is positively charged and hyaluronan negatively charged. The solutions can be conserved one week at 4°C. The pH of both solutions were adapted at 4 after the addition of the corresponding polyelectrolyte, using either HCl or NaOH.

2.2.1.3 Substrates

PPy nanotube frameworks, synthesized as explained in section 2.1, were used as substrates for the LbL deposition in order to cover the nanotubes with the biomimetic (HA/COL)-coating. For

the cellular tests, glass coverslips, serving as positive cell-adhesive control, were also coated using the same procedure as the PPy frameworks. Prior to the LbL deposition, the glass coverslips were cleaned by two successive sonications: a first one of 12 hours in ethanol and a second one of 12 hours in ultrapure water.

2.2.1.4 Chemical crosslinkers

1-(3-Dimethylaminopropyl)-3-ethylcarbodiimide hydrochloride (EDC, purity 98+%) was obtained from Acros Organics and N-hydroxysulfosuccinimide salt (sulfo-NHS, 98+%) was purchased from Aldrich. The chemical formulas of EDC and sulfo-NHS appear in Figure 2.3.

2.2.2 LbL deposition procedure

The LbL dipping method usually implies the substrate to be dipped consecutively in the different solutions. However, the PPy nanotube frameworks are too fragile to be manipulated with tweezers. Therefore, the substrates intended to be coated, both PPy frameworks and glass coverslips, were each placed in a well of a multi-well plate. To achieve the LbL build-up, HA and COL solutions were alternately added and retrieved from each well. This way, the samples did not have to be displaced, which could have damaged them, and remained in the same well throughout the entire process.

On each day of the LbL deposition, the pH of the HA and the COL solutions was readapted to 4, just before starting the deposition. First, the samples were immersed for 30 minutes in the HA solution. The HA solution was then retrieved and each sample was rinsed for 5 minutes in ultrapure water at pH 4 in order to wash out unadsorbed molecules. After having removed the rinsing solution, the collagen solution was added in each well. The adsorption time for collagen is of 2 hours. After another rinsing step, the cycle can be repeated until the desired number of (HA/COL)-bilayers is reached. In this work, all assembled coatings were composed of 6 (HA/COL)-bilayers.

Considering the long deposition times, a coating of 6 (HA/COL)-bilayers could not be completed in one day. All samples were thus stored in ultrapure water at pH 4 and kept at 4°C until completion of the 6 (HA/COL)-bilayers.

2.2.3 Chemical crosslinking

After the 6 (HA/COL)-bilayers were adsorbed, crosslinking of the assembled coatings was performed following the protocol based on carbodiimide chemistry established by Picart et al. [12]. Indeed, as HA and COL bear multiple carboxylic acid and amine functions, EDC and sulfo-NHS can be used to create covalent amide bonds between them within the film. The reaction mechanism of EDC/sulfo-NHS crosslinking is presented in Figure 2.3. First EDC reacts with a carboxylic acid group to form an activated intermediate (o-Acylisourea) [79]. The activated intermediate can then react with a primary amine to form an amide bond [12]. However, the o-Acylisourea intermediate is unstable as it tends to be hydrolyzed back to its carboxylic acid form [79]. Therefore, sulfo-NHS is used in conjunction with EDC to improve the efficiency of the crosslinking [79]. Sulfo-NHS reacts with the o-Acylisourea intermediate to form a more stable amine reactive ester [79]. The sulfo-NHS ester then reacts with a primary amine to form an amide bond.

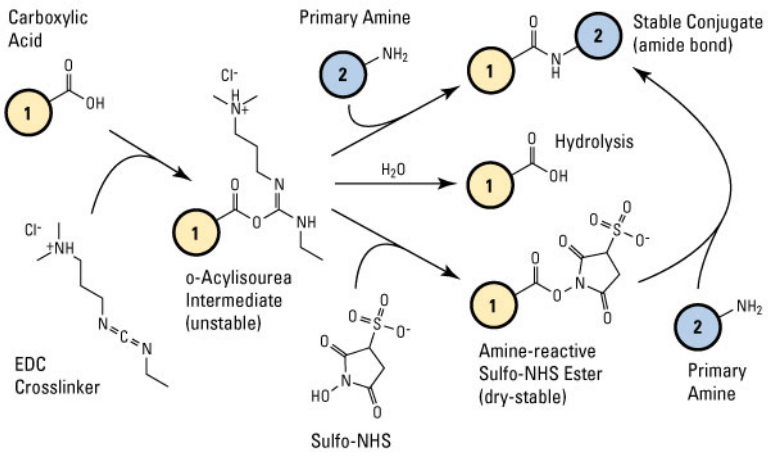


Figure 2.3: Reaction mechanism of EDC/sulfo-NHS crosslinking. Reproduced from Thermo Scientific (2012) [79].

For the crosslinking of the newly assembled films, a solution of EDC/sulfo-NHS was prepared in ultrapure water (pH 4) with a concentration of 100 mg/mL in EDC and 11 mg/mL in sulfo-NHS. Due to the high reactivity of EDC and sulfo-NHS, the crosslinking solution was prepared freshly just before use. The samples were kept in the crosslinking solution for at least 24 hours at 4°C. After crosslinking, the coated samples were rinsed 4 times for 10 minutes in ultrapure water at pH 4. Thorough rinsing was deemed necessary prior to cell seeding to avoid any harmful effect of unreacted EDC/sulfo-NHS.

2.3 Cell culture

Mouse calvaria derived MC3T3-E1 cells purchased from ATCC were cultured in alpha modified minimal essential medium (α-MEM) purchased from Gibco, Life Technologies. The culture medium was supplemented with 10% Fetal Bovine Serum (FBS sterile filtered, from Lonza), 1% penicillin streptomycin (pen/strep, Gibco) and 1% sodium pyruvate (100 mM solution, sterile filtered, Sigma-Aldrich). The cells were kept in an incubator at 37°C in an atmosphere with 5% CO_2 and 95 % humidity. Culture medium was changed every 2 or 3 days. All manipulations were performed in sterile conditions under a laminar flow hood. When reaching confluence, a passage of the cells was performed through trypsinization using trypsin/EDTA (200mg/L Versene, 170.000 U Trypsin/L, Lonza). Prior to trypsinization, cells were rinsed with sterile PBS (Lonza) to remove any unattached cells. Passages were performed each time the cells reached confluence until enough cells were obtained to start the cellular tests. All cells used for the tests described in sections 2.4 and 2.5 were at a passage number between 23 and 25.

2.4 Cell adhesion and proliferation tests

The ability of the coated PPy nanotube frameworks to support adhesion and proliferation of MC3T3-E1 cells was assessed by means of three tests. The proliferative ability of MC3T3-E1 cells was evaluated by means of a DNA quantification assay. Cell adhesion and morphology were evaluated by epifluorescence microscopy and scanning electron microscopy (SEM).

2.4.1 Experimental plan

Two complete sets of samples, named group A and B, were prepared (Tab. 2.2). As cell adhesive proteins present in the fetal bovine serum (FBS) may mask the effect of the (HA/COL)-coating by interacting with the collagen and hyaluronan, cells of group A were cultured on the samples

for 24 hours in culture medium that was not supplemented with FBS. In contrast, cells of group B were cultured on the samples for 24 hours in culture medium that was supplemented with FBS. This separation into two groups was intended to enable a clear discrimination of the effect of the biomimetic (HA/COL)-coating from the one of adhesive proteins naturally found in FBS. To highlight a potential effect of nanotopography on cell behavior, two nanotube diameters for the PPy nanotube frameworks were tested: 40 and 300 nm. In addition to (HA/COL)-coated samples, non-coated PPy frameworks of both nanotube diameters were also tested to assess the effect of the PPy nanostructure alone. Glass coverslips, both coated and non-coated, were used as positive cell adhesive controls. For the DNA quantification assay, samples were prepared in triplicates, while only one sample of each type was prepared for epifluorescence microscopy.

Table 2.2: Experimental plan for the cellular adhesion and proliferation tests. "PPy x nm" designates PPy nanotube frameworks with tubes of x nm diameter. "+$(HA/COL)_6$" indicates a sample coated with 6 crosslinked bilayers of hyaluronan (HA) and collagen type I (COL).

24 hours			
Density = 500 000 cells/well			
Ultra-low attachment 24-well plate (Corning)			
Group A: Without FBS		**Group B: With FBS**	
Adhesion & morpholgy (Epifluorescence)	*DNA quantification*	*Adhesion & morphoolgy (Epifluorescence)*	*DNA quantification*
Glass [x1]	Glass [x3]	Glass [x1]	Glass [x3]
Glass +$(HA/COL)_6$ [x1]	Glass +$(HA/COL)_6$ [x3]	Glass +$(HA/COL)_6$ [x1]	Glass +$(HA/COL)_6$ [x3]
PPy 40 nm [x1]	PPy 40 nm [x3]	PPy 40 nm [x1]	PPy 40 nm [x3]
PPy 300 nm [x1]	PPy 300 nm [x3]	PPy 300 nm [x1]	PPy 300 nm [x3]
PPy 40 nm +$(HA/COL)_6$ [x1]	PPy 40 nm +$(HA/COL)_6$ [x3]	PPy 40 nm +$(HA/COL)_6$ [x1]	PPy 40 nm +$(HA/COL)_6$ [x3]
PPy 300 nm +$(HA/COL)_6$ [x1]	PPy 300 nm +$(HA/COL)_6$ [x3]	PPy 300 nm +$(HA/COL)_6$ [x1]	PPy 300 nm +$(HA/COL)_6$ [x3]

After completing the tests presented in Table 2.2, the two PPy frameworks of 40 nm nanotube diameter (i.e. the coated one and the non-coated one) from group B prepared for epifluorescence microscopy were also imaged by scanning electron microscopy (SEM). SEM images intended to enable a more precise observation of the cell morphology and to focus on the cellular interactions with the PPy nanotube frameworks at the nanoscale.

2.4.2 Cell seeding

Prior to the cell seeding, all samples described in table 2.2 were transferred to ultra-low attachment multi-well plates (Corning). The purpose of these anti-adhesive multi-well plates was to prevent cells from adhering outside from the samples (i.e. on the walls or bottom of the wells). Sterilization of the samples was achieved by immersion in 70% volume ethanol solution for 30 minutes. The sterilizing solution was then removed and the samples were rinsed 4 times in sterile PBS (Lonza) for 10 minutes each. MC3T3-E1 cells at passage 24 were seeded on the samples at a density of 500 000 cells/mL(= cells/well as 1 mL was distributed per well of a 24-well plate). Samples of group A were seeded with cells suspended in culture medium non-supplemented with FBS while samples from group B were seeded with cells suspended in culture medium supplemented with FBS. Just before seeding, cell densities of both cell suspensions were determined by trypan blue exclusion staining (Trypan blue solution, 0.4%, sterile-filtered, Sigma) with a LUNA-II^{TM} automated cell counter from Logos Biosystems. After cell seeding, the cells were maintained in culture for 24 hours in an incubator at 37°C in an atmosphere with 5% CO_2 and 95% humidity

before their retrieval for the DNA quantification assay and their fixation for epifluorescence microscopy.

2.4.3 DNA quantification assay

The number of cells attached to each sample after 24 hours of culture was determined by fluorometric DNA quantification. A CyQUANT^{TM} Proliferation Assay kit was purchased from Molecular Probes. CyQUANT^{TM} proliferation assays are based on the use of a green fluorescent dye, the CyQUANT^{TM} GR dye, whose fluorescence is strongly enhanced when bound to cellular nucleic acids. Fluorescence can be directly measured and converted to cell number by means of a calibration curve built from a known number of cells of the same type as those used in the experiment [80].

2.4.3.1 Cell retrieval and lysis

Cell retrieval for DNA quantification was achieved by trypsinization using trypsin/EDTA (Lonza). Cells were first rinsed with sterile PBS before being trypsinized and then centrifuged to recover cell pellets. The cell pellets were then rinsed with PBS and centrifuged a second time to evacuate the phenol red which might interfere with the CyQUANT^{TM} assay. The cell pellets collected from each sample were then frozen at -80 °C. This freezing step is important to ensure effective cell lysis for the DNA quantification assay.

2.4.3.2 Assay procedure

The CyQUANT^{TM} kit provides a 400X concentrated GR-dye solution in dimethyl sulfoxide (DMSO) and a 20X concentrated cell lysis buffer (CLB). Before the start of the assay, the concentrated cell lysis buffer was diluted 20 times in ultrapure water. The reagent solution containing the DNA-binding dye was then prepared by diluting 80 times the CyQUANT^{TM} GR dye with the freshly prepared CLB solution. This way a GR dye/CLB solution was obtained with a 5X GR dye final concentration. According to the CyQUANT^{TM} protocol, this is sufficient to extend the linear detection range to 250 000 cells [80]. The dye solution was prepared on the day of the assay and was kept protected from light.

In order to build a fluorescence/cell number calibration curve, reference pellets of 500 000 MC3T3-E1 cells frozen at -80 °C were thawed and resuspended in CLB. From each reference cellular suspension, serial dilutions (with factor 2) were performed in the wells of a 96-well microplate such as to span cell numbers from 244 to 250 000. CLB/GR dye 5X solution was then added in each well to reach a final volume of 200 μL. For each sample group (A and B), this was done three times such as to obtain three repetitions of the cell number calibration curve. For each repetition, a well containing only the CLB/GR dye solution (i.e. with no cells) was used as a blank.

Cell pellets from the studied samples frozen at -80 °C after 24 hours of culture (section 2.4.3.1) were thawed and then each pellet was resuspended in 200 μL of CLB/GR dye 5X solution. Each sample cellular suspension was entirely transferred to a well of the microplate (Fig. 2.4). One well containing only the CLB/GR dye solution (i.e. with no cells) was used as a blank.

Fluorescence in each well was then measured with a Tecan infinite M200-PRO plate reader at an excitation and emission wavelength of 480 nm and 520 nm respectively.

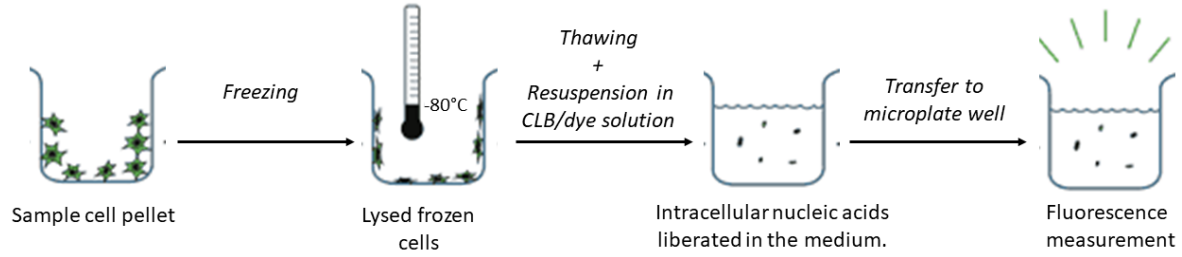


Figure 2.4: Schematic of the principle of the CyQUANT^{TM} DNA quantification of the cells retrieved from the samples. Cell pellets previously retrieved from the samples and frozen at -80°C, are thawed and resuspended in CLB/GR dye solution. The freezing step and resuspension in CLB ensure lysis of the cells. Intracellular nucleic acids are thus released in the medium and react with the GR dye. After the transfer of the suspension in the well of a microplate, fluorescence intensity is measured with a plate reader at an excitation wavelength of 480 nm and an emission wavelength of 520 nm. Adapted from ThermoFisher [81].

2.4.3.3 Cell number computation and statistical analysis

The fluorescence measurements of the calibration cell suspensions were used to build a fluorescence/cell number calibration curve by a quadratic least squares regression. Two curves were realized, one for group A (without FBS) and one for group B (with FBS), which respectively represented the relationship between the number of cells and the observed fluorescence for samples from group A and samples from group B. Those curves were used to convert the fluorescence intensity of each sample into a number of cells adherent to this sample.

Results for each sample type (i.e. glass, glass coated, PPy 40 nm, PPy 40 nm coated, PPy 300 nm and PPy 300 nm coated) will be presented as the mean of each triplicate ± the standard error of the mean. Within each sample group (A and B), the average cell numbers of the tested sample types were compared by performing a one-way analysis of variance (ANOVA) followed by a post-hoc test for pairwise multiple comparisons with Tukey's honestly significant difference procedure. Also within each group, the effect of the nanostructure and the coating, as well as their possible interaction, was assessed by means of a two-way ANOVA. Finally, for each sample type, simple comparison of the mean cell number of this sample type in group A (without FBS) and in group B (with FBS) was performed by a t-test to evaluate the effect of the serum. For all statistical tests, a difference was considered statistically significant for a p-value below 0.05. All of these tests (i.e. t-test, ANOVA, post-hoc test) were realized with MATLAB.

2.4.4 Epifluorescence microscopy

2.4.4.1 Cell fixation

Cells intended for epifluorescence imaging were fixed on the samples by crosslinking the proteins with a solution of 4% w/v paraformaldehyde in PBS. First, the samples were rinsed three times for 5 minutes with PBS. Then, the samples were incubated in the paraformaldehyde solution each for 20 minutes at room temperature. Finally, the samples were rinsed twice for 10 minutes with a solution of PBS Tween-20 0.05%. The samples were then kept at 4 °C until the next day when the immunostaining was performed.

The 4% w/v paraformaldehyde solution used for cell fixation was prepared the day before the fixation by diluting paraformaldehyde (Paraformaldehyde prills 95%, Aldrich) in a PBS solution. The PBS solution was made by diluting PBS powder (Phosphate buffered saline, pH 7.4, Sigma) into ultrapure water. The solution was incubated overnight at 60 °C. The PBS Tween-20 0.05% solution was prepared by diluting one bag of PBS Tween-20 0.05% (P3563-10 PAK, Sigma) in 1L of milli-Q water.

2.4.4.2 Immunostaining

The samples on which cells had been fixed with the paraformaldehyde solution were immunostained for epifluorescence microscopy with an Actin Cytoskeleton and Focal Adhesion staining kit from Millipore (Catalog No. FAK100). Vinculin monoclonal antibody (purified clone 7F9) and a secondary antibody conjugated with green fluorophore FITC (Goat anti-mouse IgG FITC-conjugated AP124F, Millipore) were used to mark the focal adhesions. Phalloidin conjugated with TRITC, a red fluorophore, was used to mark actin filaments. DNA intercalant 4',6-diamidino-2-phenylindole (DAPI) was used to stain the nuclei in blue.

First, the cell membranes were permeabilized by incubating the samples for 5 minutes in a Triton X-100 0.1% solution (Sigma). Second, the samples were rinsed twice for 10 minutes with a PBS Tween-20 0.05% solution. The PBS Tween-20 0.05% solution was prepared by diluting PBS Tween-20 0.05% powder (Phosphate Buffered Saline, pH 7.4, with Tween 20, Sigma) into ultrapure water. Third, the samples were incubated in a blocking buffer solution containing 1% bovine serum albumin (BSA, Sigma-Aldrich) in PBS for 30 minutes at room temperature. Then, the primary anti-vinculin antibody was diluted 175 times into the blocking buffer solution. The samples were incubated in the resulting solution for 1 hour at room temperature. Next, the samples were rinsed three times for 10 minutes each in the PBS Tween-20 0.05% solution. A last solution was made by diluting 200 times the secondary FITC-conjugated antibody and 100 times the phalloidin-TRITC into PBS. The samples were incubated for 1 hour at room temperature in the resulting solution. Then, the samples were rinsed three times for 10 minutes with PBS Tween-20 0.05% solution. Finally, for each sample, $20\mu l$ of Vectashield + DAPI was put on a glass slide. The cellular side of the sample was put on the DAPI and a second glass slide was put on top of the sample. The samples, each sandwiched between two glass slides, were stored at 4 °C in aluminum sheet, until the imaging process, in order to protect them from light and avoid quenching of the fluorescent markers.

2.4.4.3 Image acquisition

The epifluorescence images were acquired using a fluorescence microscope Olympus IX71. For each sample, two magnifications were used: 10x and 40x. At each magnification, five images were taken per sample in each of the three channels: the blue channel corresponding to the nuclei, the red channel corresponding to the actin filaments and the green channel corresponding to the focal adhesions. Furthermore, the corresponding images in the three colors were merged to create an image showing the nuclei, the actin filaments and the focal adhesions.

2.4.5 Scanning Electron Microscopy

In order to observe more precisely cell morphologies and cell interactions with the PPy nanotube frameworks at the nanoscale, images of the coated and non-coated PPy 40 nm samples were acquired by scanning electron microscopy (SEM). The two samples had previously been immunostained and imaged by epifluorescence microscopy (section 2.4.4).

The two samples were dehydrated by successive immersions in 20%, 40%, 60%, 80% and 100% (v/v) ethanol/water solutions. For each solution the immersion time was 5 minutes. The samples were then immersed in hexamethyldisilazane (HMDS, purity 99+%, Aldrich) for 10 minutes. The samples were then left to dry overnight under a fume hood. Imaging was performed the next day.

Just before imaging, the samples were sputter coated with gold using a Cressington 208HR sputter coater. The final thickness of the gold layer coated on the samples was of 20 nm. Images were acquired with a JEOL JSM 7600F scanning electron microscope at 15 kV.

2.5 Cell differentiation tests

Differentiation ability of the MC3T3-E1 preosteoblastic cells on the PPy nanotube frameworks was studied by means of an alkaline phosphatase (ALP) quantification assay. As seen in the literature review (section 1.2.2), ALP is an early marker of osteoblastic differentiation. The differentiation tests were carried out in two separate series. A first ALP assay was carried out to assess the effect of the 3D nanostructure of the PPy framework on cell differentiation. Then, a second assay was performed to study the effect of the biomimetic (HA/COL) coating.

2.5.1 ALP assay on uncoated PPy nanotube frameworks

The ability of the uncoated PPy frameworks to support the osteoblastic differentiation of MC3T3-E1 cells was assessed by quantifying the level of ALP activity after 7, 14 and 21 days of incubation in osteogenic medium (osteogenic medium composition is described in section 2.5.1.2). Both the intracellular and extracellular (excreted in the medium) ALP activities were quantified by means of an ALP colorimetric assay. In parallel, cell number was computed by means of a fluorometric DNA quantification assay in order to normalize the ALP activity of each sample by the number of cells adhered on the said sample.

2.5.1.1 Experimental plan

To assess the ability of the uncoated PPy frameworks to support the osteoblastic differentiation and evaluate the effect of the nanotube diameter of the PPy frameworks, confluent MC3T3-E1 cells were incubated in osteogenic medium for 7, 14 and 21 days on triplicates of glass, PPy 40 nm and PPy 300 nm frameworks at an initial cell density of 1 000 000 cells/well in ultra-low attachment 24-well plates (Corning) (Tab. 2.3).

Table 2.3: Experimental plan for the cellular differentiation tests. "PPy x nm" designates PPy nanotube frameworks with nanotubes of x nm diameter.

7 days	14 days	21 days
Density = 1 000 000 cells/well		
Ultra-low attachment 24-well plate (Corning)		
Glass [x3]	Glass [x3]	Glass [x3]
PPy 40 nm [x3]	PPy 40 nm [x3]	PPy 40 nm [x3]
PPy 300 nm [x3]	PPy 300 nm [x3]	PPy 300 nm [x3]

2.5.1.2 Cell seeding and cell differentiation

MC3T3-E1 cells at passage 23 were seeded on the samples at the same time for the three durations (i.e. 7, 14 and 21 days) following the same procedure as described for the cellular adhesion tests (section 2.4.2). The only difference is that the cells were inoculated at a cellular density of 1 000 000 cells/well for the cellular differentiation tests instead of 500 000 cells/well. One specific ultra-low attachment 24-well plate (Corning) was used per incubation duration (i.e. one plate for the 7-day period, one for the 14-day period and one for the 21-day period).

Before being cultured in differentiation medium, the cells were first allowed to proliferate on the samples for 7 days in proliferation culture medium. The proliferation culture medium is the classical culture medium as already used for the cell culture or the cell adhesion test (i.e. α-MEM supplemented with 10% FBS, 1% pen/strep and 1% sodium pyruvate) (section 2.3). During this 7-day period, the proliferation culture medium was changed every 2 or 3 days.

At the end of the 7-day proliferation period, differentiation of the cells was induced by replacing the proliferation culture medium with an osteogenic medium. Osteogenic medium is obtained by supplementing the proliferation medium with 400 μM L-ascorbic acid and 10mM β-glycerophosphate, which are necessary for osteoblastic differentiation as seen in the literature review (section 1.2.2). Solutions of L-ascorbic acid and β-glycerophosphate were obtained by solubilizing respectively L-ascorbic acid powder (Sigma) and β-glycerophosphate powder (Sigma) in Dulbecco's phosphate-buffered saline (DPBS, Gibco). Prior to use, both solutions were autoclaved and sterile filtered. The three incubation periods (i.e. 7, 14 and 21 days) started at the moment at which the osteogenic medium was added (i.e. 7 days after the cell seeding). This osteogenic medium was replaced every 2-3 days. Throughout the proliferation and differentiation periods, the cells were maintained in culture on the samples in an incubator at 37°C in an atmosphere with 5% CO_2 and 95 % humidity.

At the end of each incubation period, cells and culture media from the corresponding plate were retrieved and frozen at -80°C. As for the cell adhesion tests (section 2.4.3.1), cell retrieval was achieved by trypsinization.

2.5.1.3 ALP quantification

Both extracellular and intracellular ALP levels were quantified by colorimetric assay using para-nitrophenylphosphate (p-NPP), a chromogenic substrate for phosphatase enzymes such as ALP. In basic conditions and in the presence of divalent cationic cofactors (Mg^{2+} or Zn^{2+}), ALP catalyzes the hydrolysis of p-NPP which liberates an inorganic phosphate and p-nitrophenol (Fig. 2.5) [82]. Unlike p-NPP which is colorless, p-nitrophenol in alkaline conditions has a yellow color and a strong absorbance at 405 nm [83]. Therefore, the amount of p-nitrophenol produced from p-NPP can be calculated from absorbance measurements at 405 nm using an absorbance/p-nitrophenol calibration curve. ALP activity is defined as the quantity of p-nitrophenol produced per unit time.

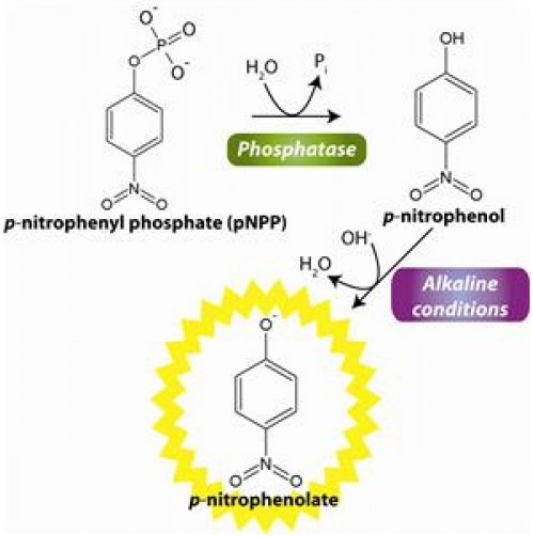


Figure 2.5: Schematic of the principle of phosphatase colorimetric assay using p-nitrophenylphosphate as a substrate. A phosphatase enzyme catalyzes the hydrolysis of p-NPP producing an inorganic phosphate P_i and p-nitrophenol. In alkaline conditions, p-nitrophenol is present in the form of p-nitrophenolate, which has a yellow color and a strong absorbance at 405 nm. Reproduced from G-Biosciences [83].

Prior to starting the assay, the following solutions were prepared. For the establishment of the absorbance/p-nitrophenol calibration curves, a solution of 20 mM p-nitrophenol (4-nitrophenol, spectrophotometric grade, Sigma) was prepared in the cell lysis buffer (CLB) provided in the CyQUANT^{TM} proliferation assay kit (section 2.4.3). A CLB/GRdye 5X solution was also

prepared as explained in section 2.4.3. The reagent solution of 10 mM p-NPP (4-Nitrophenyl phosphate disodium salt hexahydrate for enzyme immunoassay, Sigma) and 10mM $MgSO_4$ (Magnesium sulfate hepta-hydrate, ≥99% purity, Sigma-Aldrich) was prepared in a carbonate/bicarbonate buffer at pH 10.5. The carbonate/bicarbonate buffer was realized by diluting sodium carbonate (Sodium carbonate Decahydrate, ≥99% purity, Fluka) and sodium bicarbonate (Sodium bicarbonate, 99.7+%, for analysis ACS, Acros Organics) into ultrapure water. Throughout the assay, the reagent solution was kept protected from light. A stop solution of 0.1 M NaOH and 0.1 M ethylenediaminetetraacetic acid (EDTA, Titriplex III, Millipore) was prepared in ultrapure water. The addition of the stop solution has the effect of stopping the enzymatic reaction. Indeed, the addition of NaOH disturbs the pH, disrupting, therefore, ALP activity. EDTA is a chelating agent. Therefore, it fixes the cofactor Mg^{+2} ions and, as a consequence, inhibits the reaction [82].

To produce the absorbance/p-nitrophenol calibration curves, serial dilutions (with factor 2) of the p-nitrophenol solution were performed in the wells of 96-well plate such as to span p-nitrophenol concentrations ranging from 0.007 mM to 18 mM. The stop solution was then added to bring the total volume to 200 μL. For each serial dilution, one well containing only the CLB and stop solutions (i.e. with no p-nitrophenol) was used as a blank. Serial dilutions were performed for both intracellular ALP quantification and for extracellular ALP quantification in order to build their respective calibration curve.

To quantify the extracellular ALP activities, the culture media retrieved from each sample which had been frozen at -80°C were thawed at 37°C. Then, 100 μL of the culture medium of each sample were transferred in a well of the 96-well plate. 80 μL of the reagent solution were added in each well. The reaction was left to occur for 30 minutes at 37 °C. At the end of the 30 minutes reaction period, 20 μL of the stop solution were added to each well in order to stop the reaction. One well filled with culture medium from one of the glass samples, to which the stop solution was added before the reagent solution in order to prevent any reaction, was used as a blank.

For the quantification of the intracellular ALP, cells pellets recovered from each sample and frozen at -80 °C were thawed. As the pellets were also used for the CyQUANT^{TM} DNA quantification test (section 2.5.1.4), cells were resuspended in the CLB/GR-dye solution. 100 μL of each sample cell suspensions were transferred into the wells of the 96-well microplate. The same procedure as for the extracellular ALP quantification was then followed: the reaction was allowed to proceed for 30 minutes at 37 °C before adding the stop solution. One well filled with cellular suspension from one of the glass samples, to which the stop solution was added before the reagent solution in order to prevent any reaction, was used as a blank.

Readout of the absorbance at 405 nm of the wells of the microplate was performed with a Tecan infinite M200-PRO plate reader.

2.5.1.4 DNA quantification

To normalize ALP activities by the respective number of adherent cells on each sample, a fluorometric DNA quantification assay was performed in parallel to the ALP assay. As for the cellular adhesion test, a CyQUANT^{TM} Proliferation Assay kit purchased from Molecular Probes was used. What remained of each sample cell suspension after the ALP assay preparation was diluted four times in CLB and 200 μL of the resulting diluted cell suspensions were dispensed into the wells of a 96-well plate. The same protocol as for the cellular adhesion tests was applied (section 2.4.3).

2.5.1.5 ALP activity and cell number computation and statistical analysis

Calibration absorbance/p-nitrophenol curves for the extracellular and intracellular ALP assay were built from the absorbance measurements of the serial dilutions of p-nitrophenol by applying quadratic least squares regression. The concentration of p-nitrophenol produced on each sample, both extracellular and intracellular, was then computed from the absorbance measurements based respectively on the extracellular calibration curve and on the intracellular calibration curve. ALP activity was assessed from the quantity of p-nitrophenol produced from p-NPP. ALP activity will be expressed in nmol $\cdot$ min^{-1}. Two limits of detection were computed: the limit of detection based on the standard deviation of the blanks and the limit of detection of the regression. The first one was computed as three times the standard deviation of the absorbance of the blanks. The second one was defined as the absorbance corresponding to a null p-nitrophenol concentration according to the quadratic least squares regression (i.e. the y-intercept of the reference absorbance/p-nitrophenol curve). Absorbance values below either one or both of these limits of detection were considered as corresponding to p-nitrophenol concentrations equal to zero. More information about these limits of detection are presented in appendix B.1.2.

The cell number of the cellular suspension corresponding to each sample was determined from the fluorescence measurements and the fluorescence/cell number calibration curves obtained from a reference cellular suspension similarly to what was done for the cellular adhesion test (section 2.4.3). Normalized ALP activity was then calculated for each sample by dividing the ALP activity of the sample by its cell number.

The results of each sample type at each differentiation duration will be presented as mean $\pm$ standard error of the mean in section 3. The results (i.e. cell number, ALP activity and normalized ALP activity) were compared by performing a one-way ANOVA and a post-hoc test for pairwise multiple comparisons with Tukey's honestly significant difference procedure. Results were considered as significantly different for p-values lower than 0.05.

2.5.2 ALP assay on (HA/COL)-coated PPy nanotube frameworks

A second ALP assay was carried out on PPy nanotube frameworks coated with six (HA/COL)-bilayers to assess the effect of the bioactive coating, combined with the nanostructure, on the osteoblastic differentiation of MC3T3-E1 cells. As for the first ALP assay (section 2.5.1), ALP activity was quantified by colorimetric assay and cell number was computed by performing a DNA quantification assay in parallel to the ALP assay.

2.5.2.1 Experimental plan

The plan of the samples tested in this second ALP quantification assay is presented in Table 2.4. MC3T3-E1 cells were cultured on coated glass and coated PPy 300 nm frameworks. To assess the effect of the coating, cells were also cultured on non-coated glass and non-coated PPy 300 nm frameworks. Cells were kept in culture on the samples in osteogenic medium for 14 and 21 days. For each differentiation time, each type of sample was prepared in triplicate. The samples were placed in an ultra-low attachment 24-well plate (Corning) and seeded with a cell density of 500 000 cells/well.

Table 2.4: Experimental plan for the cellular differentiation tests on coated samples. "PPy x nm" designates PPy nanotube frameworks with nanotubes of x nm diameter.

14 days	21 days
Density = 500 000 cells/well	
Ultra-low attachment 24-well plate (Corning)	
Glass [x3]	Glass [x3]
Glass + $(HA/COL)_6$ [x3]	Glass + $(HA/COL)_6$ [x3]
PPy 300 nm [x3]	PPy 300 nm [x3]
PPy 300 nm + $(HA/COL)_6$ [x3]	PPy 300 nm + $(HA/COL)_6$ [x3]

2.5.2.2 Cell seeding and cell differentiation

MC3T3-E1 cells at passage 25 were seeded on each sample with a density of 500 000 cells/well following the same procedure as for the first ALP assay (section 2.5.1). Two ultra-low 24-well attachment plates (Corning) were used, one for each differentiation time (i.e. 14 days and 21 days).

As in the first ALP assay, cells were first allowed to proliferate on the sample for a duration of 7 days. At the end of this period, the proliferation medium was replaced by the osteogenic medium (section 2.5.1). The same protocol as for the first ALP assay was applied. Both cells and cell media were retrieved and frozen at -80°C at the end of each differentiation times. Prior to freezing, cell pellets were washed with PBS.

2.5.2.3 ALP and DNA quantification

Extracellular and intracellular ALP activities were quantified following the same protocol as for the first ALP assay (section 2.5.1). Cell number was quantified in parallel with a CyQUANT™ Proliferation assay (Molecular Probes) following the same procedure as the first ALP assay (section 2.5.1).

2.5.2.4 ALP activity and cell number computation and statistical analysis

Computation of ALP activities, cell number and normalized ALP activities was performed as described in section 2.5.1. Results will be presented as mean ± standard error of the mean in section 3. Results were compared by performing a one-way ANOVA and a post-hoc test for pairwise multiple comparisons with Tukey's honestly significant difference procedure. A difference was considered statistically significant for p-values lower than 0.05. This statistical analysis was performed using MATLAB.

Chapter 3

Results and Discussion

In this chapter, the results of the cellular tests will be presented and discussed. The chapter will be divided into two main parts. In the first part, the results of the adhesion and proliferation tests will be reported and discussed. In the second part, the results of the differentiation tests will be analyzed. In both cases, the effects of the nanostructure of the PPy frameworks and of the hyaluronan/collagen LbL coating on cell behavior will be investigated.

3.1 Cell adhesion and proliferation

The objective of the adhesion and proliferation tests was to assess the ability of the PPy nanotube frameworks to support the adhesion and proliferation of MC3T3-E1 mouse preosteoblastic cells. Cell number on each sample was determined after 24 hours of culture by means of a DNA quantification assay. Cell morphology and spreading were qualitatively evaluated by epifluorescence microscopy after immunostaining. Furthermore, cell interactions with PPy nanotube frameworks were assessed by SEM. In this section, the results of these tests will be presented and the effects of the PPy framework nanostructure, of the nanotubes diameter and of the (HA/COL)-coating will be discussed.

3.1.1 DNA quantification

The fluorescence readouts of reference cellular suspensions of known cell density enabled the production of calibration curves displaying the fluorescence intensity as a function of the number of cells (in absence and in presence of FBS in the proliferation medium). These curves, which were used to determine the number of cells attached to each sample (section 2.4.3), are shown in appendix A.1.

Two groups of samples were considered: group A and group B, where cells were cultured respectively in absence and in presence of FBS in the medium. For both groups, the initial cell seeding was $5 \cdot 10^5$ cells per sample and the cells were kept in culture on the samples for 24 hours. The detailed results for both groups are shown in appendix A.2. First, the effect of the PPy nanostructure and of the (HA/COL)-coating will be discussed within each group separately. Finally, the results of both groups will be compared to evaluate the effect of FBS on cell adhesion.

3.1.1.1 Group A: Cells cultured without FBS

For the cells cultured on group A samples (culture medium without FBS), the best cell adhesion results were achieved on the coated glass ($1.58 \cdot 10^4 \pm 0.45 \cdot 10^4$ cells, $mean \pm SE$), which served as positive cell adhesive control, and on the coated PPy 300 nm ($1.47 \cdot 10^4 \pm 0.08 \cdot 10^4$ cells) (Fig. 3.1). The lowest number of attached cells was the one of the non-coated glass ($0.54 \cdot 10^4 \pm 0.1 \cdot 10^4$ cells). The only statistically significant difference in cell number (assessed by one-way ANOVA and

post-hoc multiple comparison test, see section 2.4.3) was the difference between the non-coated glass and the coated glass samples. Nonetheless, trends regarding the effects of the nanostructure of the PPy samples and of the biomimetic (HA/COL)-coating can be observed between the samples. Looking at the non-coated samples, it seems that the PPy frameworks enhance the cell adhesion compared to the bare glass, with the 40 nm diameter nanotubes seeming to be even more beneficial to the cell adhesion than the 300 nm nanotubes. Regarding the effect of the biomimetic (HA/COL)-coating, the coated glass yielded an increased cell adhesion compared to the bare glass. This is in accordance with results previously reported in the literature showing that biomimetic coatings of ECM components such as collagen can further enhance the cell adhesive properties of glass culture substrates [84]. However, the effect of the (HA/COL)-coating seems to depend on the surface onto which the coating is applied. In particular, for the PPy frameworks the effect of the coating seems to depend on the dimension of the nanotopographical cues. Indeed, whereas the coating further enhanced the already beneficial effect of the nanotopography for the 300 nm diameter nanotube frameworks, it attenuated the beneficial effect of the nanotopography of the 40 nm nanotube frameworks. This was confirmed by a two-way ANOVA. Indeed, the two-way ANOVA revealed that the interaction between the type of sample (i.e. glass, PPy 40 nm or PPy 300 nm) and the coating state (i.e. coated or non-coated) significantly influences the number of adhering cells (Tab. 3.1).

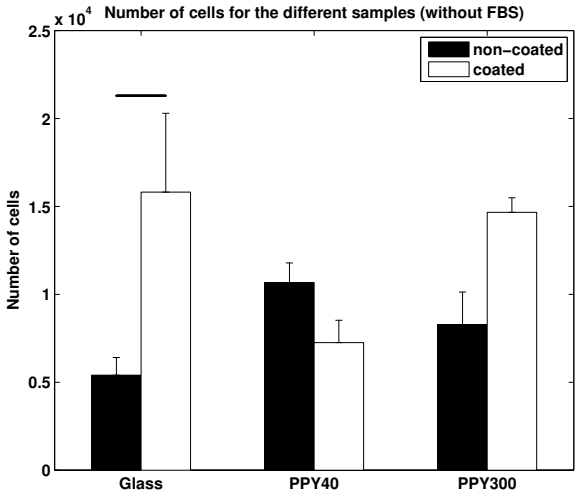


Figure 3.1: Mean cell number per sample type after 24h of culture in the absence of FBS, computed from the fluorescence/cell number calibration curve and the fluorescence readouts. The error bars correspond to the standard error of the mean (SE). A horizontal line above two results indicates a significant difference between those two results (p-value<0.05).

Table 3.1: Two-way ANOVA results for cell adhesion test without FBS. Sample type is glass, PPy 40 nm or PPy 300 nm. Coating state is coated or non-coated. Sample type*Coating state designates the interaction between the sample type and the coating state.

Parameters	p-value
Sample type	0.5189
Coating state	0.0267
Sample type*Coating state	0.0213

3.1.1.2 Group B: Cells cultured with FBS

For the cells cultured on group B samples (culture medium with FBS), the best cell adhesion results were obtained for the non-coated PPy 40 nm ($6.38 \cdot 10^4 \pm 1.62 \cdot 10^4$ cells, $mean \pm SE$) followed by the coated PPy 40 nm samples ($5.25 \cdot 10^4 \pm 1.65 \cdot 10^4$ cells) and the coated glass samples ($5.08 \cdot 10^4 \pm 0.84 \cdot 10^4$ cells) used as positive cell adhesive control (Fig. 3.2). Again, the bare glass showed the lowest number of adherent cells ($1.75 \cdot 10^4 \pm 1.07 \cdot 10^4$ cells). None of the observed differences in mean cell number were statistically significant as assessed by one-way ANOVA followed by post-hoc multiple comparison test (see section 2.4.3). Nevertheless, as for group A (without FBS), trends regarding the effects of the PPy nanotube framework and

of the biomimetic (HA/COL)-coating can be inferred. Looking at the non-coated samples, as observed in absence of FBS, the nanostructure of the PPy frameworks seems to enhance the cell adhesion compared to the bare glass control. Also in line with the results of group A, the 40 nm diameter nanotube framework appears to have an even more beneficial effect on cell adhesion than the 300 nm diameter framework. Regarding the effect of the coating, the (HA/COL)-coating seems to enhance the cell adhesion for the glass samples. However, the effect of the biomimetic (HA/COL)-coating on the PPy nanotube frameworks, previously observed in absence of FBS (group A), seems to be masked in presence of FBS. Indeed, the (HA/COL)-coating appears to have no effect on the PPy 300 nm frameworks. The coating may even slightly decrease the beneficial effect of the 40 nm nanotubes on cell adhesion but the standard error of the mean (SE) is high for both the coated and non-coated samples. Furthermore, in contrast to group A (without FBS), a two-way ANOVA did not attribute a significant effect to the interaction between the coating state and the sample type on the number of adherent cells or to any of these parameters considered on its own (Tab. 3.2). The attenuation of the effect of the (HA/COL)-coating in the presence of FBS can probably be attributed to the masking of the biomimetic coating by the adsorption of a mixture of proteins present in FBS. The addition of FBS could lead to a homogenization of the surfaces of the samples presented to the cells. However, it is not certain that the layer of adsorbed proteins on a non-coated substrate is identical to the adsorbed layer on a (HA/COL)-coated substrate. It is therefore also possible that the similar adhesion levels of bare and coated PPy frameworks are not the result of a similar layer of adsorbed proteins but of a combination of other factors.

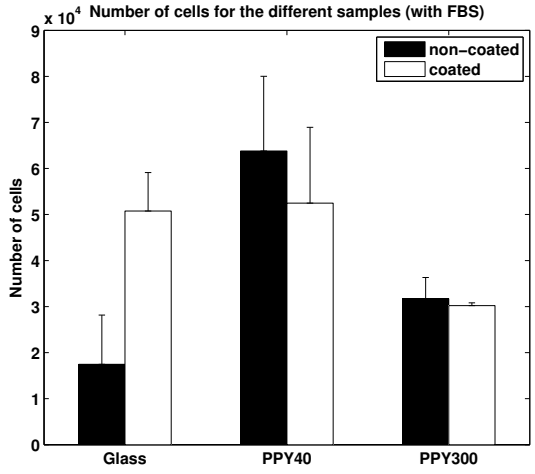


Figure 3.2: Mean cell number per sample type after 24h of culture in the presence of FBS, determined from the fluorescence/cell number calibration curve and the fluorescence readouts. The error bars correspond to the standard error of the mean (SE).

Table 3.2: Two-way ANOVA results for cell adhesion test with FBS. Sample type is glass, PPy 40 nm or PPy 300 nm. Coating state is coated or non-coated. Scaffold type*Coating state designates the interaction between the sample type and the coating state.

Parameters	p-value
Sample type	0.0845
Coating state	0.5035
Sample type*Coating state	0.1798

3.1.1.3 Comparison of group A and B: effect of FBS

When comparing the cell adhesion results obtained in the absence or presence of FBS in the culture medium, it can be seen that for all samples, coated or non-coated, the number of attached cells is always higher in the presence of FBS (Fig. 3.3). This higher number of attached cells is significant for all samples except for the non-coated glass and the coated PPy 40 nm samples. This difference in cell adhesion is explained by the adsorption of a mixture of proteins naturally present in the serum, which has the effect of increasing the adhesive properties of both the glass and PPy substrates. Consequently, the adsorption of serum proteins may lead to a homogenization

of the surfaces of the samples. This may explain the attenuated difference in terms of adherent cells number between the coated and non-coated PPy samples in presence of FBS. In addition, it can be seen that the SE is higher in the presence of FBS. The FBS seems, therefore, to be a source of variability in the results. Nevertheless, similar conclusions were reached in absence and presence of FBS regarding the effect of the PPy frameworks on cell adhesion. Considering the bare PPy frameworks, cells seem to adhere the most on the 40 nm diameter nanotube framework, both in presence and in absence of FBS. In absence of FBS, the effect of the coating was shown to depend on the size of the PPy nanotubes. Indeed, it further increased the adhesive properties of the 300 nm nanotube framework on cell adhesion but attenuated the adhesive properties of the 40 nm PPy nanotube framework. Finally, the main conclusion to be drawn from the DNA quantification assay is that the non-coated and coated PPy frameworks showed an increased cell adhesion compared to bare glass, which possesses high cell-adhesive properties [85, 86] and has been commonly used as cell culture substrate for decades [87, 88]. Moreover, the PPy samples with the most adherent cells in each group, i.e. the coated and non-coated PPy 40 nm with FBS and the coated PPy 300 nm without FBS, performed similarly to the coated glass, which is a positive cell adhesive control.

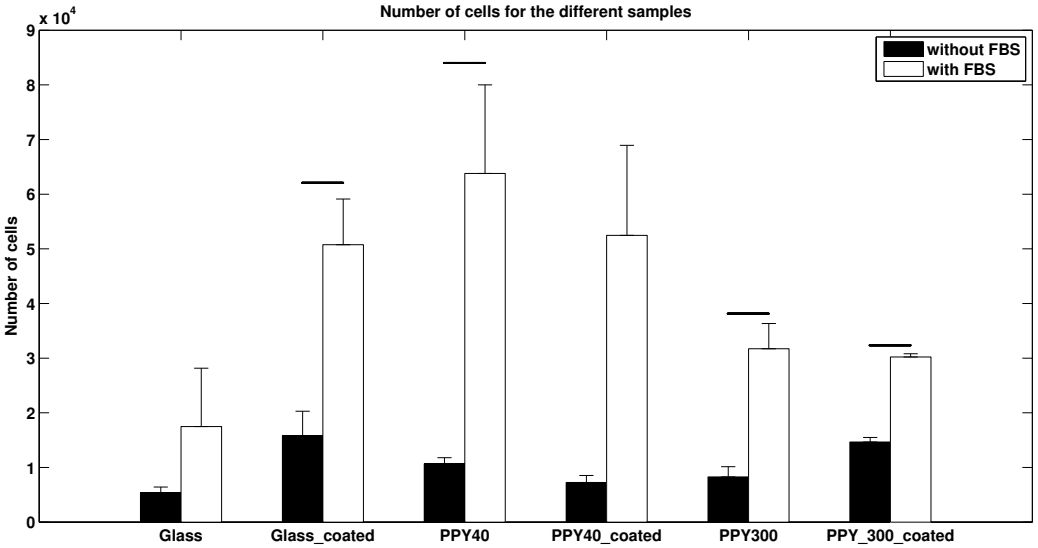


Figure 3.3: Mean cell number per sample type after 24h computed from the fluorescence/cell number calibration curve and the fluorescence readouts for the samples seeded in culture medium without FBS (black) and with FBS (white). The error bars correspond to the standard error of the mean (SE). A horizontal line above two results indicates a significant difference between those two results (p-value<0.05), assessed by a t-test for each sample between the results of this sample in the absence and in the presence of FBS.

3.1.2 Qualitative evaluation of cell adhesion

Cell adhesion after 24 hours of culture in absence (group A) or in presence (group B) of FBS on the samples was qualitatively evaluated by epifluorescence microscopy after fixation and immunostaining of the cells on their sample. To do so, images at low magnification (x10) were acquired to observe the density of adherent cells on each sample of group A and B (Fig. 3.4 and Fig. 3.5 respectively). Observations will also be compared with the results of the DNA quantification assay (section 3.1.1). The effects of the serum, of the nanostructure of the PPy samples and of the LbL (HA/COL)-coating will be discussed.

3.1.2.1 Effect of FBS

Comparison between the images acquired on the samples of group A (Fig. 3.4) and the images acquired on the samples of group B (Fig. 3.5) reveals a higher density of adherent cells in the presence of FBS (Fig. 3.5). This is in accordance with the results of the DNA quantification assay. The only exception is the PPy 300 nm +$(HA/COL)_6$ sample which shows very few cells in the presence of FBS (Fig. 3.5(f)), in contradiction with the results of the DNA assay. This result and the poor quality of the image suggest that a problem may have occurred during the immunostaining procedure. Indeed, immunostaining on PPy frameworks proved not trivial as they present a particular combination of characteristics, not usually encountered in optical studies of cell morphology. The PPy samples are not smooth, flat and transparent but highly porous, black, opaque and present a 3D structure. Nevertheless, the acquired images show, with the exception of the PPy 300 nm +$(HA/COL)_6$ (Fig. 3.5(f)), that cells are more numerous in presence of FBS. It can also already be noticed, as will be confirmed at higher magnification in section 3.1.3, that without FBS, cells have a more spherical morphology and seem more isolated from one another. Nonetheless, cells still managed to attach to and to colonize the PPy samples in 24 hours even in the absence of serum, thus showing the intrinsic ability of the PPy frameworks to support cell adhesion.

3.1.2.2 Effect of the nanostructure

In the absence of FBS, no clear difference is observed in terms of adherent cell density between the non-coated PPy samples (Fig. 3.4(b-c)) and the non-coated glass sample (Fig. 3.4(a)). However, in presence of FBS, differences between the uncoated PPy samples (Fig. 3.5 (b-c)) and the glass sample (Fig. 3.5(a)) are more pronounced. Indeed, both non-coated PPy 40 nm (Fig. 3.5(b)) and PPy 300 nm (Fig. 3.5(c)) samples display an increased adherent cell density compared to the bare glass control and the cells appear to be more spread. Cells on the bare PPy samples are also less isolated than on the glass control. This confirms the conclusions from the DNA quantification (section 3.1.1) that the 3D PPy nanostructure enhances cell adhesion compared to bare glass.

3.1.2.3 Effect of (HA/COL)-coating

First, it is important to point out that the assessment of the effect of the coating is complicated by the poorer quality of some of the images, mainly those from the coated samples (for example Fig.3.4(e) and Fig.3.5(e)). Indeed, DAPI (blue) and the anti-vinculin primary and secondary antibodies (green) proved difficult to image correctly on certain samples, especially coated PPy samples, as they formed halos and spots. This is probably the result of a combination of factors, originating from the intrinsic characteristics of the PPy frameworks (e.g. high porosity, opacity, 3D structure) and from the (HA/COL)-coating. Indeed, biomacromolecules from the coating are probably able to bind specifically or non-specifically the immunostaining markers. This would explain the poorer quality of the images of the coated PPy samples. The observations for the coated samples should, therefore, be taken with caution.

The main motivation for the division of the samples into two groups, one without FBS and one with FBS, was to distinguish the effect of the coating itself on cell adhesion from the effect of cell adhesive proteins present in the serum. In the absence of FBS, no difference is observed in terms of cell adhesion between the glass (Fig. 3.4(a)) and coated glass (Fig. 3.4(d)) samples. Regarding the PPy samples, lower adherent cell densities are observed on the coated PPy 40 nm (Fig. 3.4(e)) and coated PPy 300 nm (Fig. 3.4(f)) than on the glass and coated glass samples. On the PPy nanotube frameworks, the coating appears here to have a detrimental effect on the cell adhesion. This observation is in contradiction with the results of the DNA quantification (section 3.1.1), which revealed higher levels of cell adhesion on the coated PPy samples than

on the bare glass samples. However, the observations of the epifluorescence images are only qualitative. In addition, they allow the observation of only a fraction of the cells attached to the sample whereas the DNA quantification assay allowed the determination of the total cell number. In particular, cells may have penetrated to some extent in the PPy framework and would therefore not be visible by epifluorescence microscopy but still taken into account in the DNA quantification assay. However, considering the dense packing of the PPy nanotubes and the small thickness (25 μm) of the framework, it is likely that most cells attached only to the top and side surfaces without penetrating in the framework. Therefore, and considering the poor quality of the images of the coated samples, observations of the epifluorescence images are less reliable than the results of the DNA quantification.

In the presence of FBS, a higher adherent cells density is observed on the glass $+(\mathrm{HA/COL})_6$ sample (Fig. 3.5(d)) than on the bare glass sample (Fig. 3.5(a)). Furthermore, the cells appear to be more spread on the glass $+(\mathrm{HA/COL})_6$ sample. The coated PPy 40 nm (Fig. 3.5(e)) sample displays a density of adherent cells similar to the coated glass sample and, therefore, higher than the bare glass. This observation is in agreement with the results of the DNA quantification assay (section 3.1.1) which showed that the coated PPy 40 nm induced increased cell adhesion compared to the bare glass control. Unfortunately, the effect of the coating on the PPy 300 nm sample cannot be assessed with epifluorescence as the immunostaining of the PPy 300nm $+(\mathrm{HA/COL})_6$ (Fig. 3.5(f)) was unsuccessful.

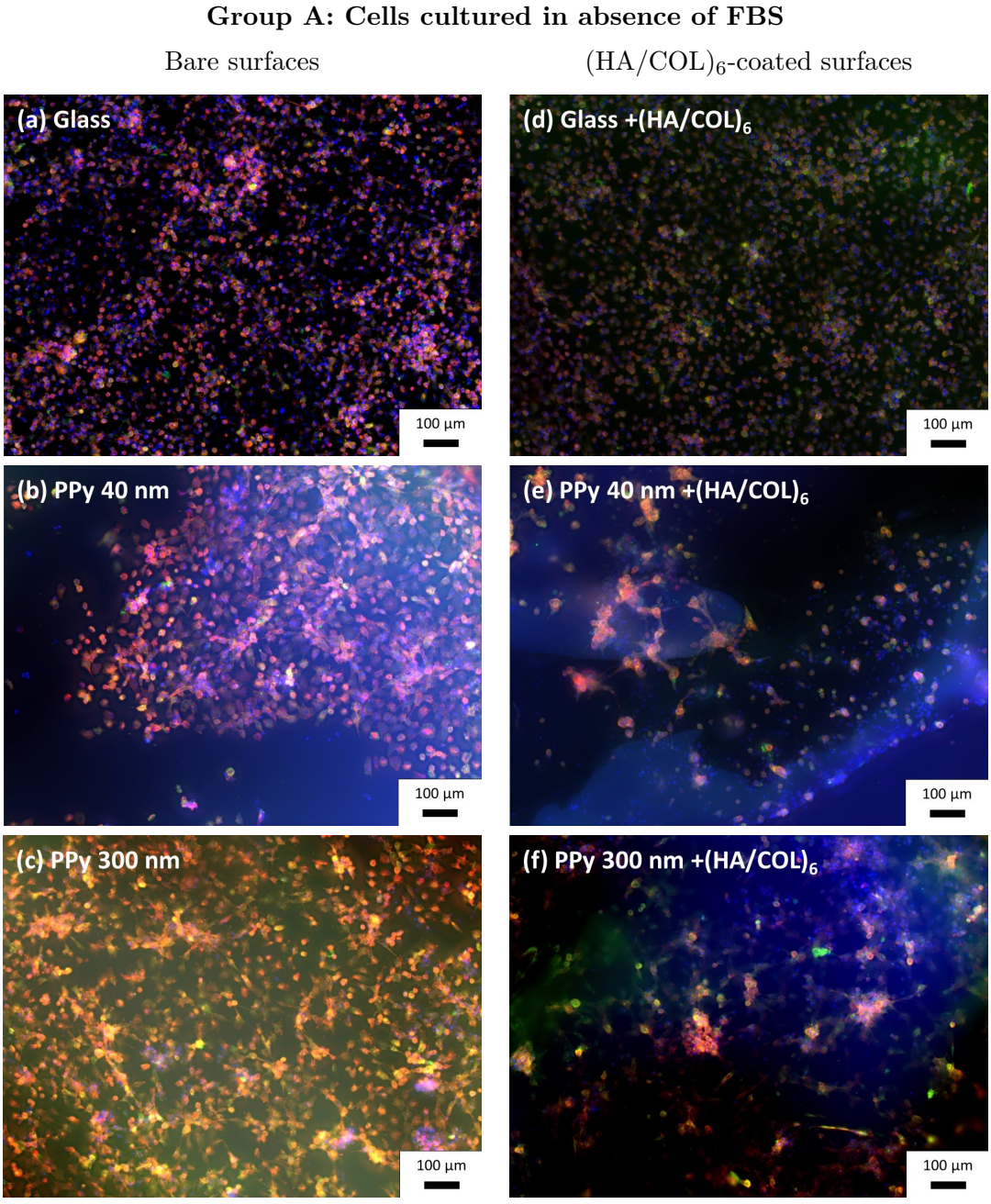


Figure 3.4: Epifluorescence images (magnification 10x) of MC3T3-E1 cells cultured for 24h in the absence of FBS on the glass substrates and PPy nanotube frameworks (group A = without FBS). Nuclei were stained in blue, actin filaments in red and focal adhesions in green.

Group B: Cells cultured in presence of FBS

Bare surfaces $(HA/COL)_6$-coated surfaces

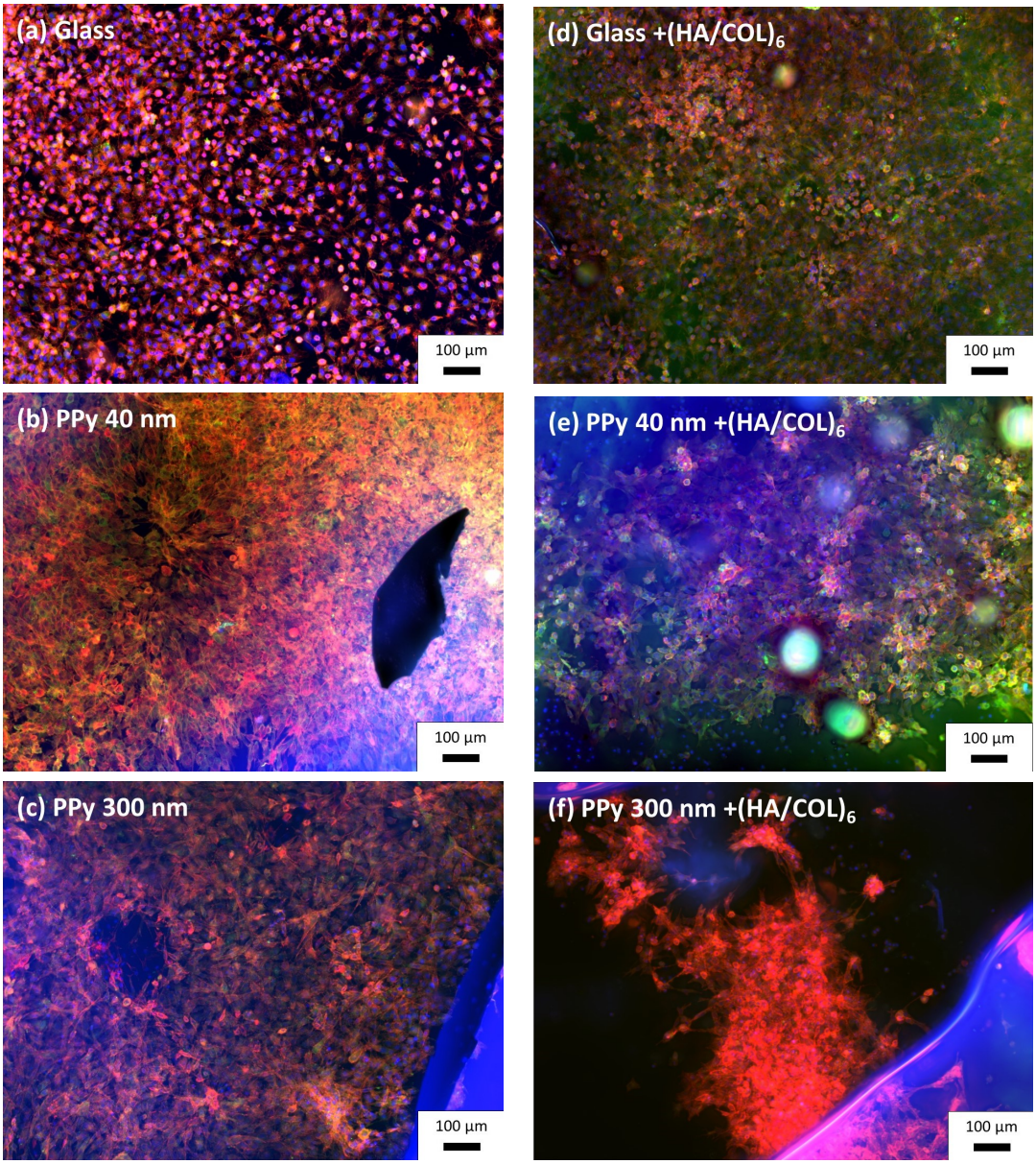


Figure 3.5: Epifluorescence images (magnification 10x) of MC3T3-E1 cells cultured for 24h in the presence of FBS on the glass substrates and PPy nanotube frameworks (group B=with FBS). Nuclei were stained in blue, actin filaments in red and focal adhesions in green.

3.1.3 Cell morphology

Epifluorescence images at a higher magnification (x40) were acquired in order to observe cell morphology on each sample after 24 hours of culture. Images acquired for samples of group A (without FBS) and samples of group B (with FBS) are presented in Figures 3.6 and 3.7 respectively. As for cell adhesion (section 3.1.2), the effects of FBS, of the nanostructure and of the (HA/COL)-coating will be discussed.

3.1.3.1 Effect of FBS

Cells cultured on the samples in presence of FBS (Fig. 3.7) display as a whole a more elongated shape than cells cultured in absence of FBS (Fig. 3.6) which present a more spherical morphology. For each sample type, cells formed more numerous and longer cell extensions in the presence of FBS. This can be explained by the presence of various cell adhesive proteins in the serum (e.g. fibronectin, collagens), which adsorb on the sample surface and promote cell spreading.

3.1.3.2 Effect of nanostructure

Considering the bare PPy samples cultured in absence of FBS, cells on both the bare PPy 40 nm (Fig. 3.6(b)) and bare PPy 300 nm (Fig. 3.6(c)) samples display a more elongated shape than on the bare glass control (Fig. 3.6(a)). Cells on bare PPy 40 nm and bare PPy 300 nm also formed more numerous and longer cellular extensions than on the bare glass control. Therefore, the bare PPy nanotube frameworks promote cell spreading and the formation of cellular extensions even in the absence of cell adhesive proteins from the serum. Here, no effect of the nanotube diameter can be observed. This trend appears to be accentuated in the presence of FBS (Fig. 3.7). Cells on both bare PPy 40 nm (Fig. 3.7 (b)) and bare PPy 300 nm (Fig. 3.7(c)) samples are more elongated and exhibit longer cell extensions than on the bare glass control (Fig. 3.7(a)), further confirming the positive effect of the nanostructure of the PPy frameworks on cell spreading. The enhanced cell spreading on the PPy frameworks in the presence of FBS may be the result of a nanostructure-directed adsorption of cell adhesive proteins from the serum. Indeed, the nanotopography of the substrate has been shown to have a significant impact on protein adhesion, which in turns controls the cell response via cell-membrane receptors such as the integrins [45,68]. In this case, the particular repartition and conformation of the adsorbed proteins on the PPy frameworks may have forced the cells to elongate more than on the flat glass surface.

3.1.3.3 Effect of the (HA/COL)-coating

In absence of FBS, no effect of the coating on cell morphology can be distinguished on the glass samples (Fig. 3.6(a) and Fig. 3.6(d)) . Indeed, cells on the coated glass display a spherical shape similar to what is observed on the uncoated glass. Regarding the effect of the coating on PPy samples, cells on PPy 40 nm +$(HA/COL)_6$ (Fig. 3.6(e)) display a round shape with almost no cell pseudopods. As observed in the DNA quantification results (section 3.1.1) and in the cell adhesion observation (3.1.2), the coating has a detrimental effect on cell adhesion and spreading on PPy 40 nm samples in absence of FBS. However, a similar effect is not observed for the PPy frameworks with 300 nm diameter nanotubes as cells spread on the PPy 300 nm +$(HA/COL)_6$ (Fig. 3.6(f)) as well as on the PPy 300 nm (Fig. 3.6(c)) and formed numerous filopodia.

In presence of FBS, cells display a good spreading on the PPy 40 nm +$(HA/COL)_6$ (Fig. 3.7(e)) with long cell extensions. The enhanced cell spreading on the PPy 40 nm coated sample in presence of FBS compared to without FBS suggests that for this nanotube diameter, the adsorption of cell adhesive proteins on the coating is necessary to support efficiently cell adhesion and spreading. Finally, even though the immunostaining of the PPy 300 nm+$(HA/COL)_6$ of group B (Fig. 3.7(f)) was not completely successful (section 3.1.2), an image at magnification

x40 of cells on this sample could be acquired. Despite the poorer quality of the image (spots of DAPI and unsuccessful vinculin staining), it is possible to observe the elongated shape of the cells and the presence of cell extensions. This suggests that the cells behave as well on the coated PPy 300 nm (Fig. 3.7(f)) than on the bare PPy 300 nm (Fig. 3.7(c)).

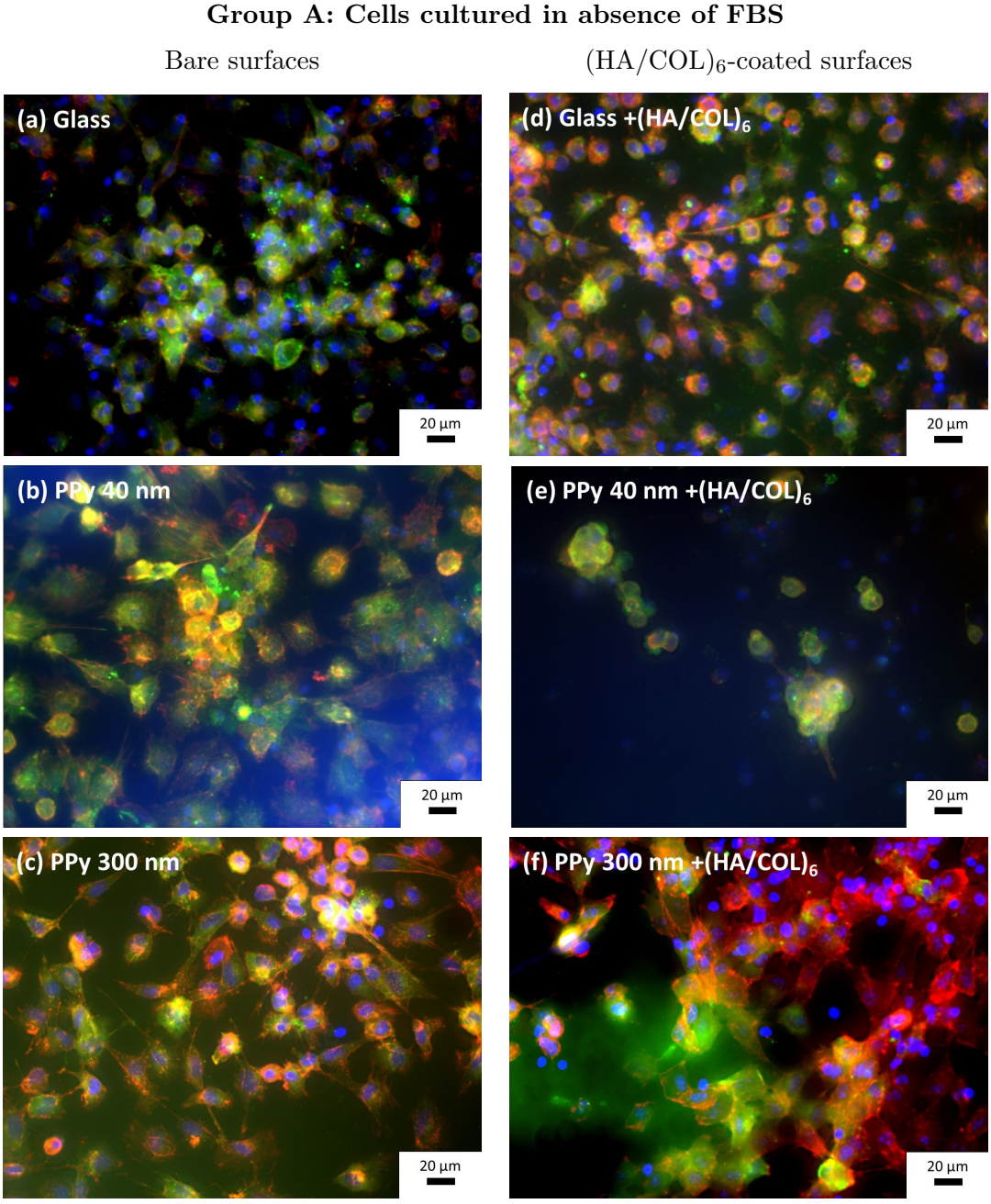


Figure 3.6: Epifluorescence images (magnification 40x) of MC3T3-E1 cells cultured for 24h in the absence of FBS on the glass substrates and PPy nanotube frameworks (group A = without FBS). Nuclei were stained in blue, actin filaments in red and focal adhesions in green.

Group B: Cells cultured in presence of FBS

Bare surfaces $(HA/COL)_6$-coated surfaces

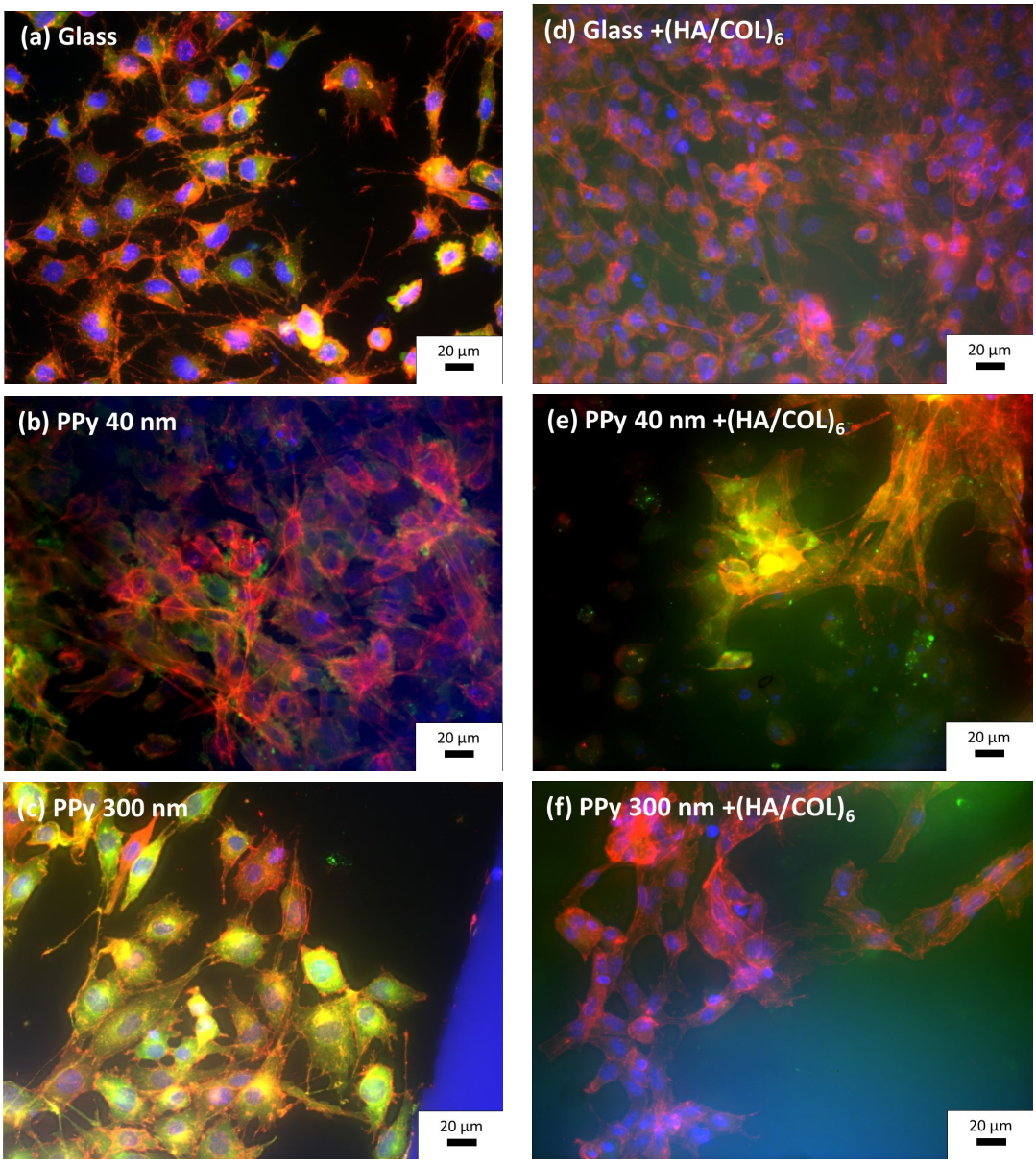


Figure 3.7: Epifluorescence images (magnification 40x) of MC3T3-E1 cells cultured for 24h in the presence of FBS on the glass substrates and PPy nanotube frameworks (group B = with FBS). Nuclei were stained in blue, actin filaments in red and focal adhesions in green.

3.1.4 Cell interactions with the PPy nanotube frameworks

The images acquired by epifluorescence microscopy allowed cell adhesion and morphology to be observed (sections 3.1.2 and 3.1.3) but did not allow the direct observation of the interactions of the cells with the PPy nanotube frameworks at the nanoscale. Therefore, two PPy samples previously imaged by epifluorescence microscopy were recovered and imaged by scanning electron microscopy (SEM). In addition, SEM images also allowed more precise observation of the cellular morphology at the nanoscale. As it yielded the best results both in terms of cell adhesion and cell morphology (sections 3.1.1, 3.1.2 and 3.1.3), the PPy 40 nm of group B (with FBS) was chosen for SEM imaging. To assess the effect of the coating, the PPy 40 nm + $(HA/COL)_6$ sample of group B was imaged as well.

3.1.4.1 Cells on non-coated PPy 40 nm

Before interpreting the SEM images, it should be reminded that the cells on the surfaces were submitted to several treatments. First, as the sample was previously imaged by epifluorescence, cells fixed on the sample were immunostained. This required the permeabilization of the cell membrane with Triton X-100 (section 2.4.4). Then, the sample was dehydrated which can induce shrinkage of the cells. Finally, the sample was sputter coated with gold to allow SEM imaging. These steps are susceptible to impact cell morphology and to introduce artifacts in the images, thus making their interpretation difficult. SEM images showing examples of artifacts produced by the pre-imaging treatments are presented in Appendix A.3

As a result of the pre-imaging treatments, the contrast between the cells and their substrate is low in some parts of the sample. Indeed, as shown in Figure 3.8, some cell membranes appear to have merged with the surface. However, despite the low contrast, the shape of the cells can still be distinguished. As already observed by epifluorescence microscopy (section 3.1.3, Figure 3.7), cells exhibit an elongated shape, thus indicating good cell spreading. Moreover, as also shown in Figure 3.8, cells have formed numerous and thin cell extensions.

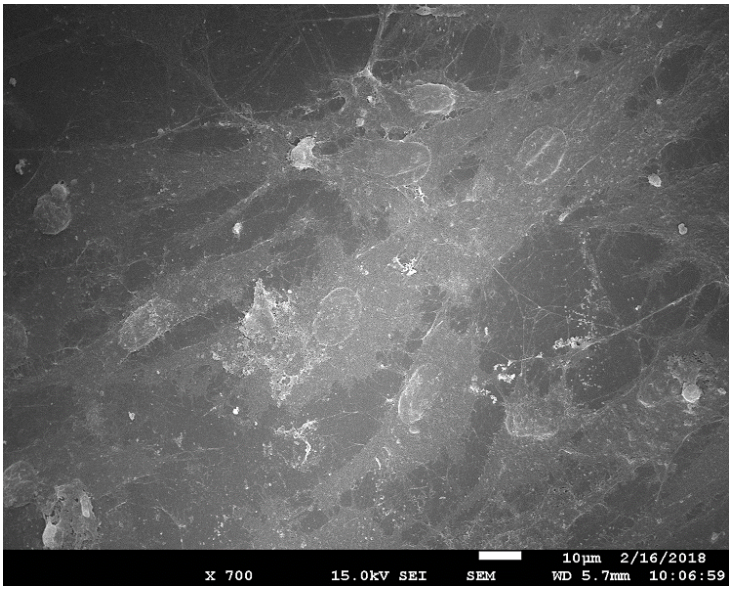
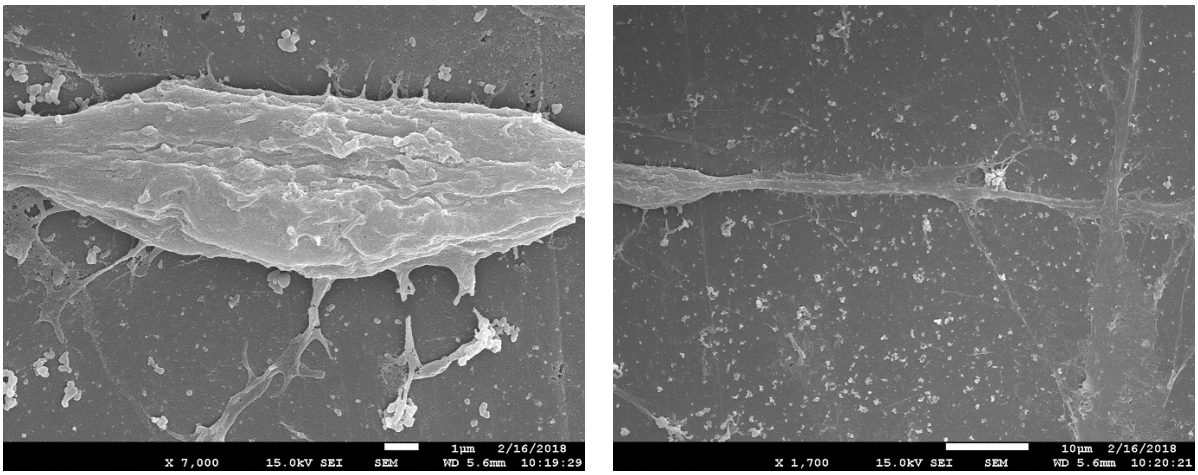


Figure 3.8: SEM image of MC3T3-E1 cells cultured for 24h in the presence of FBS on the PPy 40 nm sample (group B), previously immunostained and imaged by epifluorescence microscopy. Cells display an elongated shape and numerous thin extensions.

Figure 3.9 shows a closer view of a cell attached on the sample surface. As can be seen in Figure 3.9(a), the cell body presents an oblong shape from which numerous small pseudopodia radiate. The cell also shows a long (>40μm) rod-like appendix extending from the cell body (Fig.

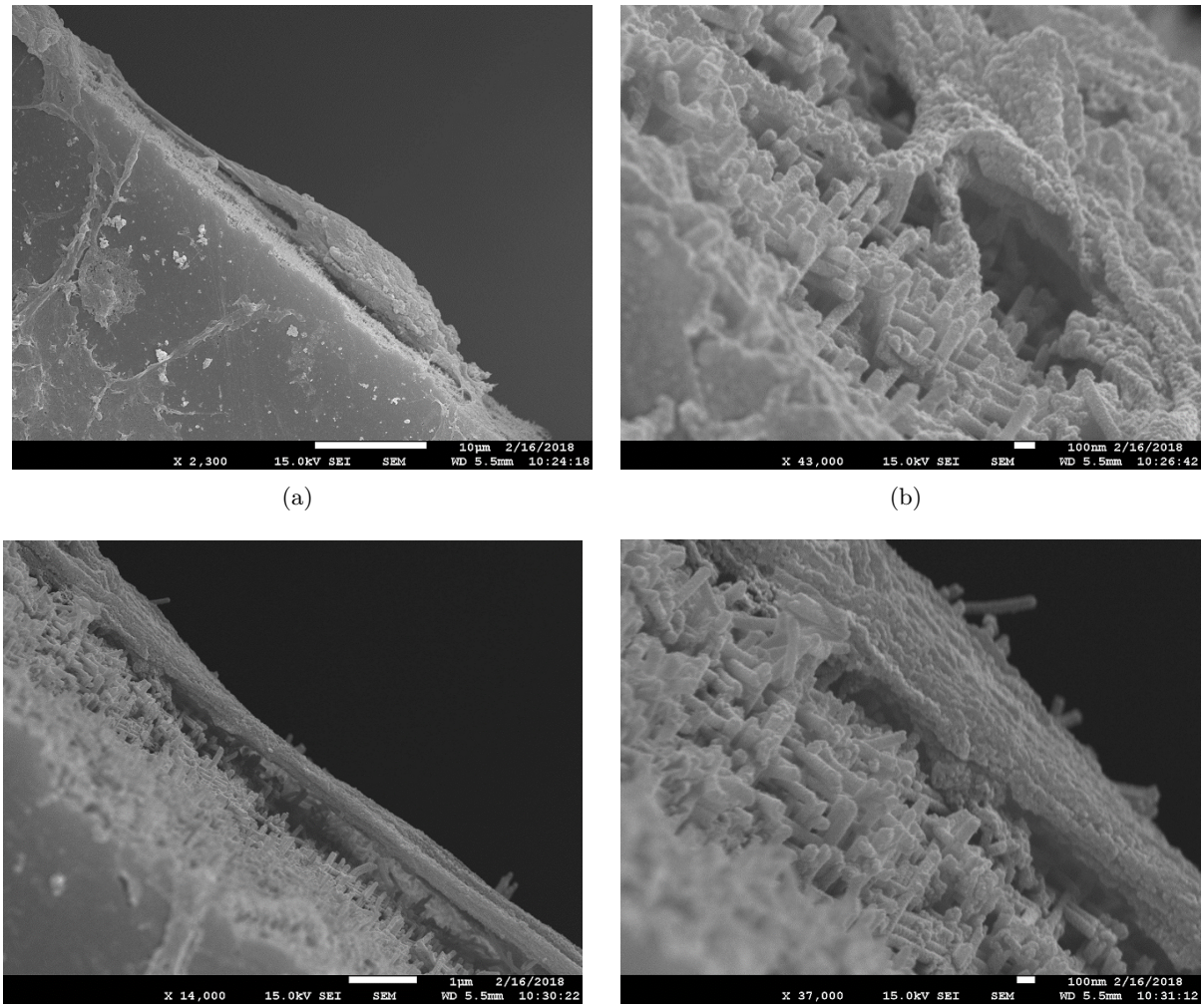
3.9(b)). Smaller and thinner extensions can be seen emerging from this main appendix. As a whole, SEM observations revealed that cells formed long cell protrusions, similarly to the example presented here. These observations further confirm the conclusion reached from epifluorescence microscopy (section 3.1.3) that the PPy 40 nm framework promotes cell spreading. However, the interactions between the cell extensions and the nanotube framework cannot be observed as the surface of the sample appears smooth. Indeed, despite a higher magnification, the heads of the nanotubes composing the framework are not visible on the image. As a result of the pre-imaging treatments, a crust has formed on the surface of the sample, thus masking the nanotubes. Two hypotheses can be formulated regarding the origin of this crust. A possible explanation is that it may be the gold layer sputter-coated just before imaging. However, this hypothesis is unlikely as only a 20 nm-thick gold layer was sputter coated on the sample, which is probably not sufficient to fully cover the substrate. It is also possible that the crust was the result from a fusion of the cellular bodies and possible ECM synthesized *de novo* by the cells caused by the pre-imaging treatments. This would explain why in some parts of the sample, cells appear almost merged with the surface (as was observed in Figure 3.8).



(a) (b)

Figure 3.9: SEM image of a MC3T3-E1 cells cultured for 24h in the presence of FBS on the surface of the bare PPy 40 nm sample (group B). (a) Cell body. The cell body exhibits an elongated shape, from which small filopodia radiate. (b) A large cell appendix extending from the cell body. The total length of the cell appendix is of more than 40 μm. Smaller cell extensions can be seen radiating from it.

The crust, however, was found to cover only the top surface of the sample, not its lateral surfaces. Indeed, as can be seen in the images of Figure 3.10, on the side of the sample, the emerging heads of the intersected PPy nanotubes can be observed. A cell can be seen attached to this side of the sample, thus allowing its interactions with the PPy nanotubes to be observed. The rough aspect of the cell membrane is a consequence of the fixation and dehydration treatment (Appendix A.3). In Figure 3.10(a), two main cell extensions can be seen attached to the sample: one cell extension on the right of the cell body and one on the left. Figure 3.10(b) is a closer view of the end of the right process. Smaller filopodia can be seen emerging from the main process to come into contact with and to attach to the heads of the PPy nanotubes. The left cell extension is about 20 μm long (Fig. 3.10(a)). As can be seen on the closer view provided by Figures 3.10(c) and (d), only the end of the cell extension actually contacts the PPy nanotubes.

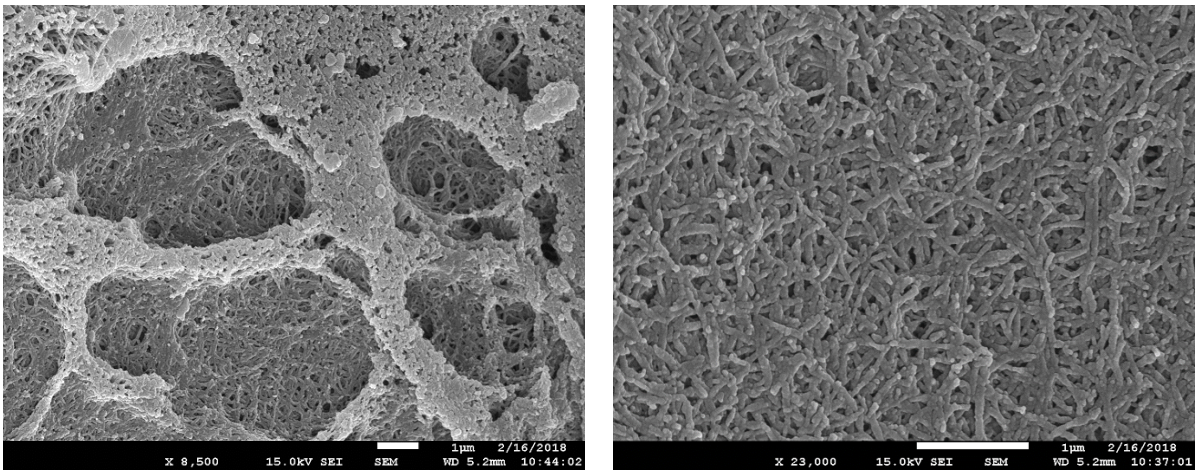


(a) (b)

(c) (d)

Figure 3.10: SEM images of a MC3T3-E1 cell on the side of the PPy 40 nm sample after 24h of culture in the presence of FBS (group B). The PPy nanotubes composing the framework are visible on the side of the sample. (a) Global view of the cell. Two main cell extensions, one on the left of the cell body and one on the right of the cell body are seen to be attached on the nanotubes (b) Closer view on the end of the right cell extension and its contact with the nanotubes. (c-d) Closer view of the left cell extension. Only the end of the cell extension (d) is in contact with the PPy nanotubes.

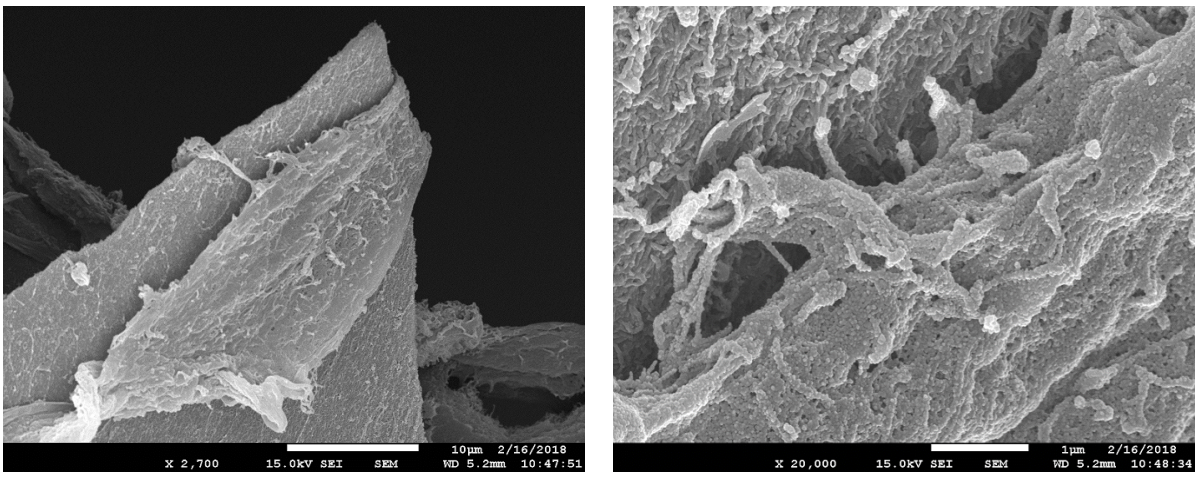
In addition to the sides of the sample, the crust was found to be interrupted in some areas of the top surface of the sample, revealing the nanotube framework underneath (Fig. 3.11). Figure 3.11(a) shows the nanotubes appearing between cell extensions (recognizable from their peculiar roughness and bursts resulting from the fixation, immunostaining and dehydration treatments). A closer view of the nanotube network is provided in Figure 3.11(b). Instead of observing the head of the nanotubes as on the side of the sample (Fig. 3.10), the nanotubes appear bent and flattened, thus indicating a collapse of the nanotube framework. However, as the nanotube framework was observed intact on the sides of the samples (Fig. 3.10), the collapse did not occur on the entirety of the sample. It is possible that the nanotube framework could not sustain forces exerted by the attached cells either during culture or upon cell dehydration, which may have generated additional forces on the nanotubes. However, it is more likely that these local collapses are a result of the pre-imaging treatments.



(a) (b)

Figure 3.11: SEM images of the top surface of the bare PPy nanotube framework with MC3T3-E1 cells after 24 hours of culture in presence of FBS (Group B). (a) The nanotubes are visible between cell extensions (with bursted membrane due to the permeabilization process) (b) Closer view of the nanotube framework. The nanotubes are bent and flattened, indicating a collapse of the nanotube framework.

Figure 3.12 shows a cell adhering to the edge of the sample. Figure 3.12(b) provides a closer view of this cell and shows multiple small cell filopodia attached to the collapsed nanotube framework underneath. This illustrates once more the interactions between the cell and the nanotopography.



(a) (b)

Figure 3.12: SEM images of a MC3T3-E1 cell cultured for 24h in the presence of FBS on the PPy 40 nm sample (group B). (a) The cell has attached on the edge of the sample (b) Multiple small cell filopodia interacting with the collapsed nanotube framework.

3.1.4.2 Cells on (HA/COL)-coated PPy 40 nm

To assess the effect of the coating, SEM images of the PPy 40 nm +$(HA/COL)_6$ sample of group B (with FBS), which was previously immunostained and imaged by fluorescence, were also acquired.

As for the PPy 40 nm sample (section 3.1.4.1), SEM images showed that the surface of the PPy 40 nm +$(HA/COL)_6$ sample was covered by a crust hiding the underlying nanotube framework. Moreover, cell observation was more difficult than for the bare PPy 40 nm sample as in most parts of the sample, cell membranes were almost entirely merged with the crust, leaving only their nuclei observable (Appendix A.3). As for the uncoated PPy 40 nm sample, the crust is probably the result of a fusion of the organic matter present on the surface of the sample (i.e. the (HA/COL)-coating, possible native ECM produced by the cells and the cells themselves) during the pre-imaging treatments. Nonetheless, in some parts of the sample, cells could still be observed as shown in Figure 3.13. As observed by epifluorescence microscopy (section 3.1.3, Fig. 3.7), cells are shown to have spread on the sample and formed multiple cell protrusions.

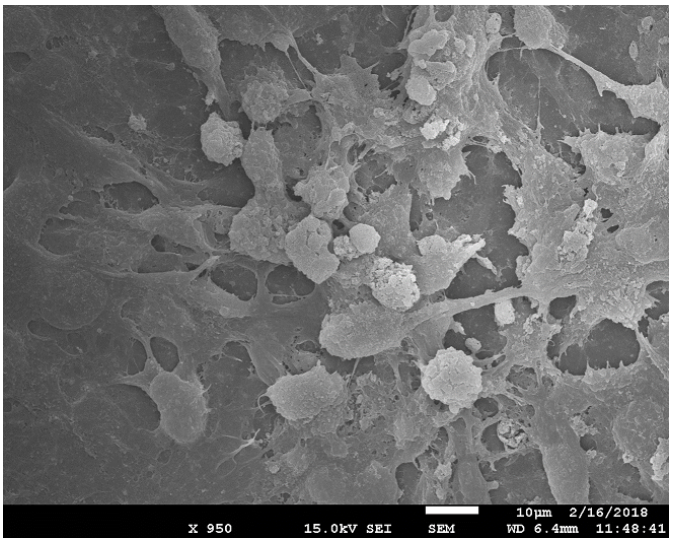
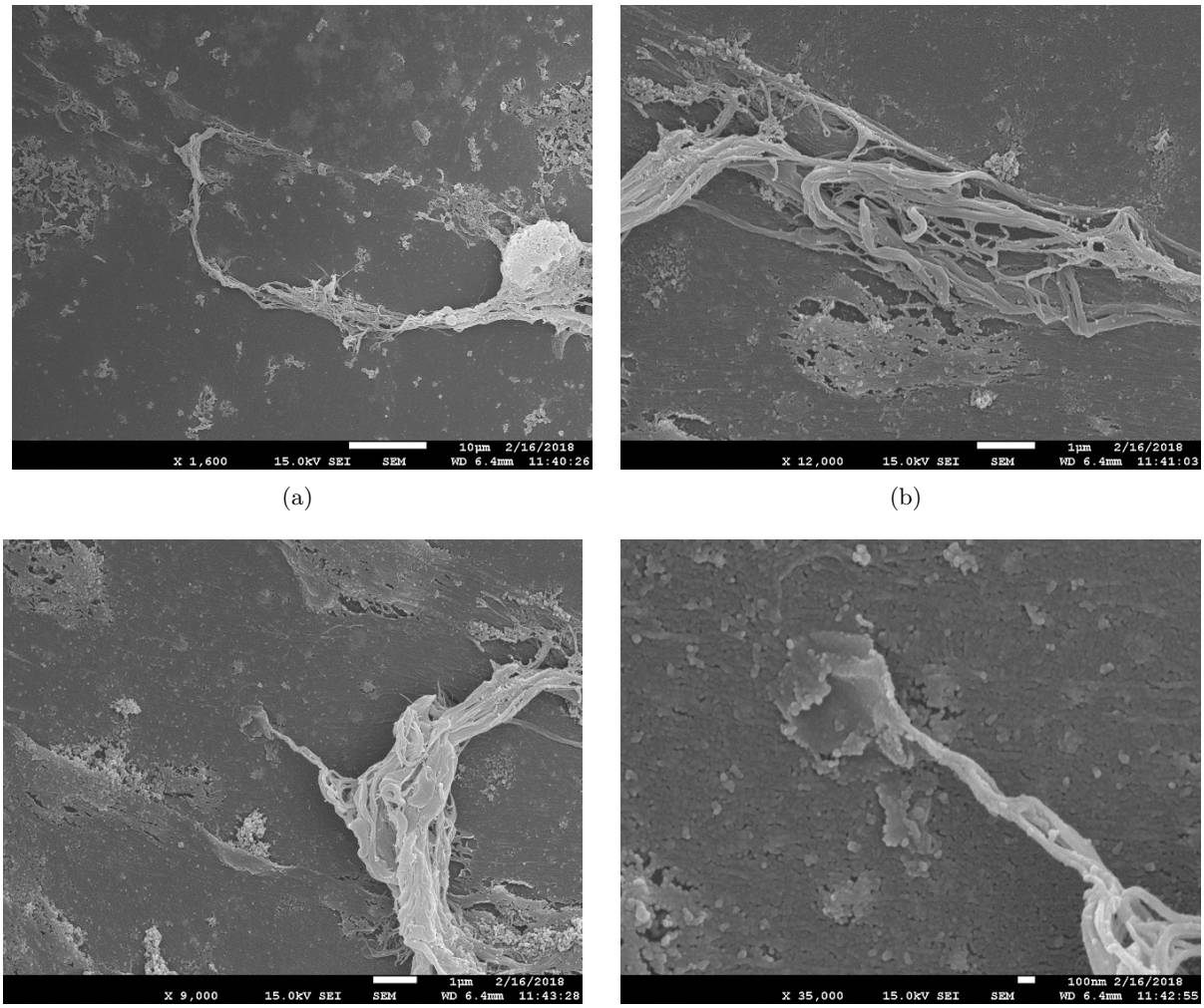


Figure 3.13: SEM image of MC3T3-E1 cells after 24h of culture on the PPy 40 nm +$(HA/COL)_6$ sample in the presence of FBS (group B), previously immunostained and imaged by epifluorescence microscopy.

Figure 3.14 shows a closer view of a cell attached on the sample which has formed a long cell extension. As shown in Figures 3.14(b-c), the cell extensions on the coated PPy 40 nm sample are more filamentous and branched than those observed on the uncoated PPy 40 nm sample (section 3.1.4.1, Fig. 3.9). This suggests that the coating may have an effect on cell morphology which could not be observed in the previous tests. However, these observations should be taken with caution considering the significant alterations that the samples' surface and cells have undergone as a result of the fixation, immunostaining and dehydration treatments (Appendix A.3).



(a) (b)

(c) (d)

Figure 3.14: SEM image of a MC3T3-E1 cell after 24h of culture on the PPy 40 nm +$(HA/COL)_6$ sample in the presence of FBS (group B). (a) The cell displays a long cell extension. (b-c-d) Closer views of the cell extension. (d) A cell extension attached to the crust.

In contrast to the uncoated PPy 40 nm, the crust covered almost the entirety of the coated PPy 40 nm sample surface, thus preventing the observation of the interactions between the cells and individual PPy nanotubes. This confirms the hypothesis that the observed crust is most probably the result of a crosslinking of organic matter from various origins, namely cell bodies, biomimetic coating and *de novo* synthesized ECM, following the pre-imaging treatments. Compared to the uncoated PPy 40 nm, holes in the crust allowing the observation of the nanotube framework underneath were less frequent and smaller for the coated PPy 40 nm sample (Fig. 3.15). In addition to the crust, a network presenting a reticulated fibrillar morphology was also observed, covering some parts of the sample surface. As shown in Figure 3.16, this fibrous network is in continuity with the crust covering the surface. A closer view of the fibrous network is shown in Figure 3.17. No similar network was observed on the uncoated PPy 40 nm sample. As seen in the literature review (section 1.3.3.6), Zhang et al. observed by AFM a fiber network on (HA/COL)-coated surfaces. The origin of this network was attributed to the assembly of the adsorbed COL molecules into fibrils during the LbL deposition process [77]. Similar networks were observed by Damien Lefèvre by SEM on non-cell-seeded (HA/COL)-coated PPy frameworks but not on non-coated PPy frameworks [89]. However, contrary to the conclusions of Zhang et al. [77], no reticulated fibrillar network was observed in the absence of any dehydration step [89]. The network was only observed after the dehydration protocol for SEM [89]. Therefore, it can

be concluded that the fibrous network on the coated PPy 40 nm results from a modification of the morphology of the (HA/COL)-coating following the dehydration treatment. Moreover, the fact that the network is in continuity with the crust (Fig. 3.16) reinforces the hypothesis formulated earlier that the crust impeding the observation of the nanotube framework is the result of a fusion of organic matter caused by the dehydration treatment. Finally, the spreading of the fiber network on the top surface indicates that the (HA/COL)-coating covers the heads of the nanotubes of the framework. The masking of the nanostructure by the coating could be a possible explanation for the poorer cell adhesion results of the coated PPy 40 nm compared to the non-coated PPy 40 nm sample (sections 3.1.1 and 3.1.2).

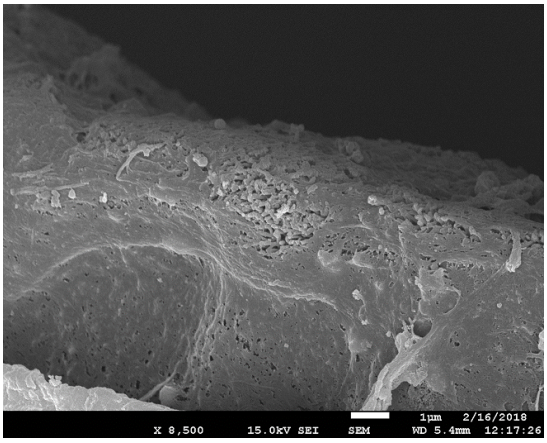


Figure 3.15: SEM image of the PPy 40 nm +$(HA/COL)_6$ with MC3T3-E1 cells after 24 hours of culture in presence of FBS (group B). The surface of the sample is covered by a crust. A hole in the crust at the edge of the sample reveals the nanotube framework underneath.

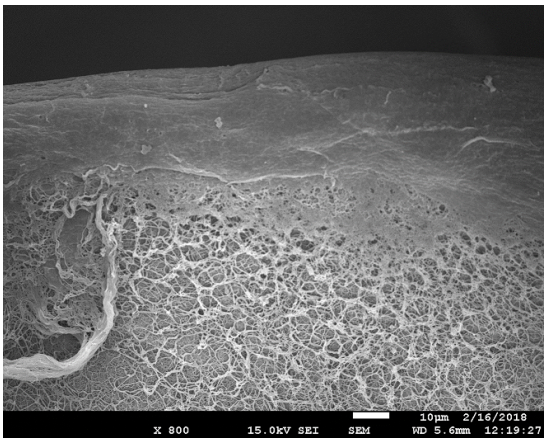
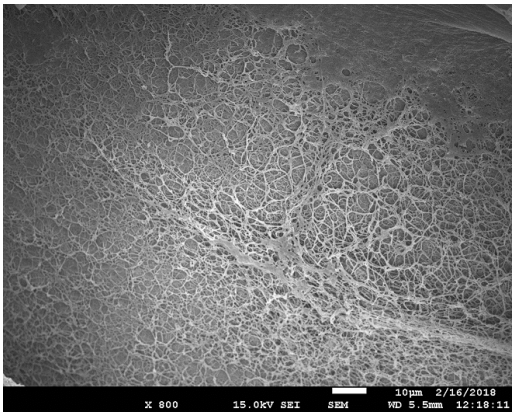
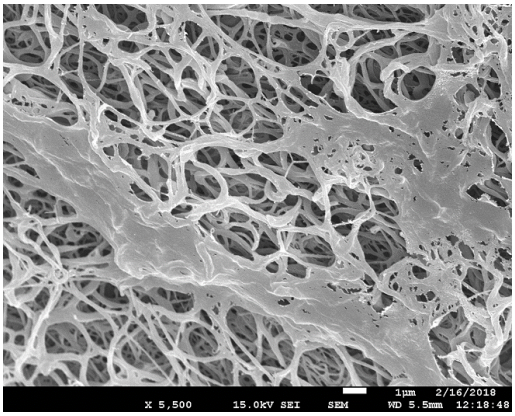


Figure 3.16: SEM image of the PPy 40 nm +$(HA/COL)_6$ sample with MC3T3-E1 cells after 24 hours of culture in presence of FBS (Group B). The crust (upper part of the image) covering the surface is in continuity with a reticulated fibrillar network (lower part of the image).



(a)



(b)

Figure 3.17: SEM images of the reticulated fibrillar network on the PPy 40 nm+$(HA/COL)_6$ sample with MC3T3-E1 cells after 24 hours of culture in presence of FBS (Group B).

3.1.5 Summary and discussion of the cell adhesion tests

The DNA quantification assay and epifluorescence images showed that the non-coated PPy nanotube frameworks enhance adhesion and spreading of MC3T3-E1 cells compared to bare glass substrates. These results are consistent with those of He et al. (2017) which showed that PPy in the form of nanowires can promote the growth and spreading of MC3T3-E1 cells [60]. A possible explanation for the increased cell adhesion on the PPy frameworks could be that the nanoscale roughness of the PPy frameworks surface contributes to mechanically maintain

the cells on the surface after their sedimentation. This would, therefore, facilitate cell anchorage compared to a smooth glass surface. As explained in the literature review (section 1.3.2), numerous studies investigating the impact of nanotopography on cell function also showed an influence of the size of the involved nanofeatures [47,63]. Similarly, the size of the PPy nanotubes composing the frameworks was shown to influence cellular attachment. The DNA quantification assay and epifluorescence images both revealed a higher density of adherent cells on the 40 nm diameter nanotube frameworks compared to the 300 nm diameter nanotube frameworks. Interactions between cells and the PPy 40 nm framework were studied by SEM. This showed that cells on the PPy 40 nm framework produced long and numerous cell extensions contacting the heads of the PPy nanotubes. However, the nanotubes framework was found to have collapsed in some areas, most probably as a result of the successive treatments prior to microscopy.

The observed effect of the LbL biomimetic (HA/COL)-coating on cell adhesion and morphology after 24 hours was found to depend on the presence of FBS in the culture medium and on the nanotopography of the underlying substrate. The coating was found to enhance adhesion of MC3T3-E1 on flat glass surfaces both in presence and absence of FBS. This is consistent with the results of Li et al. (2012) which showed that (HA/COL)-coated titanium surfaces favored adhesion and spreading of MC3T3-E1 cells [30]. However, for the PPy frameworks, the effect of the (HA/COL)-coating on cell adhesion and morphology tends to be masked in presence of FBS. Indeed, the DNA quantification assay and epifluorescence microscopy revealed that, in presence of FBS, coated PPy frameworks exhibited cell adhesion levels and cell morphologies similar to those of the non-coated frameworks of the same nanotube diameter. This effect could be the result of a homogenization of the surface of the PPy frameworks following the adsorption of a cocktail of proteins naturally present in the serum. In the absence of FBS, and, therefore, of additional cell adhesive proteins, the effect of the coating was found to depend on the diameter of the PPy nanotubes composing the framework. Indeed, the coating was found to further enhance the positive effect of the PPy nanostructure on cell adhesion for 300 nm diameter nanotubes. However, for 40 nm diameter nanotubes, the beneficial effect of the PPy nanostructure on cell adhesion was shown to be attenuated by the coating. This attenuating effect for the PPy 40 nm frameworks might be explained by a masking of the nanostructure by the coating of the PPy, as revealed by SEM images. Most probably, the different effect of the coating on PPy 40 nm compared to PPy 300 nm frameworks could be the result of a less favorable disposition of the COL and HA cell binding epitopes on nanotubes of 40 nm diameter than on nanotubes of 300 nm diameter. Indeed, as seen in the literature review (section 1.3.3), the cell response on biomimetic coatings depends not only on the presence of cell binding epitopes from ECM molecules but also on their spatial arrangement on the surface [68]. These results highlight the difficulty of distinguishing the effect of each individual parameter (nanotopography, chemical composition, etc.) on cell response because of their often synergistic and intricate outcomes. In the literature, the distinction between the individual effect of nanotopography and of surface chemistry on cell behavior is not clearly established and has been a subject of debate [4, 68, 90]. Nevertheless, despite the intricate effects of the studied parameters, the adhesion and proliferation tests showed that both bare and (HA/COL)-coated PPy frameworks induced enhanced cell adhesion and spreading compared to the bare glass control.

3.2 Cell differentiation

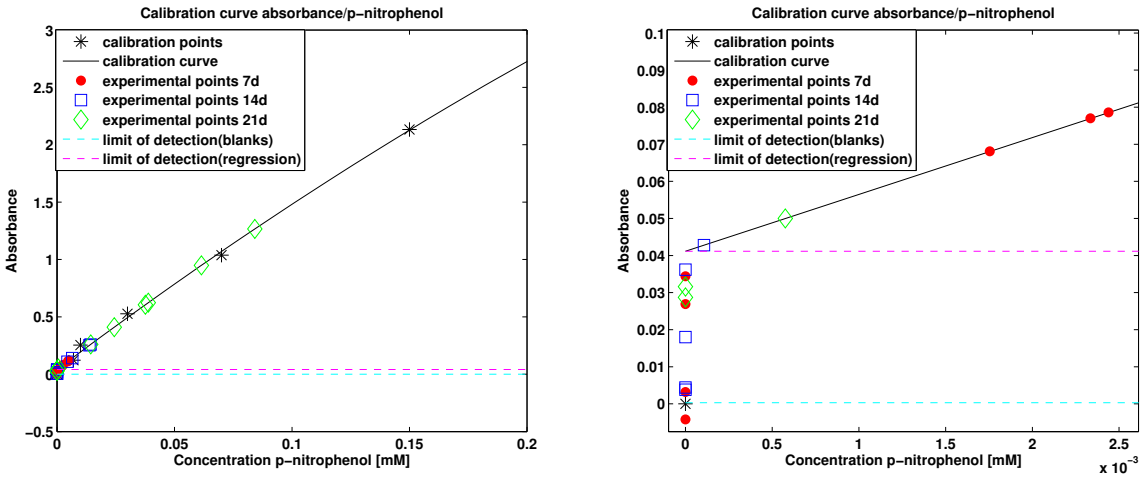
The objective of the differentiation tests was to assess the ability of the PPy framework to induce the osteoblastic differentiation of murine preosteoblastic MC3T3-E1 cells. This osteoblastic differentiation was assessed by quantifying the ALP activity of the cells cultured on the samples in osteogenic medium for 7, 14 and 21 days. A first assay was performed on non-coated samples (glass, PPy 300 nm and PPy 40 nm) to assess the effect of the PPy nanotubes frameworks

and their nanotopography on cell differentiation. A second assay was then carried out on (HA/COL)-coated samples to assess the effect of the biomimetic coating.

3.2.1 Non-coated PPy frameworks

3.2.1.1 Intracellular ALP

In order to quantify objectively the differentiation ability of the cells seeded on each substrate, the intracellular ALP activity of each sample was normalized by the number of cells adhered on the said sample. ALP activity was computed for each sample from a colorimetric assay using pNPP as substrate and cell number was computed by a fluorometric DNA quantification assay performed in parallel on the same cells. However, regarding the ALP activity, the readouts values of the p-nitrophenol absorbance were so low for the 7-day and 14-day periods that more than half of them (i.e. 10 among 18) falls below the intercept of the regression with the vertical axis and therefore cannot be assigned a p-nitrophenol concentration (Fig. 3.18). This limiting absorbance value is designated as the limit of detection of the regression. Therefore, for these absorbance values, the p-nitrophenol concentration was considered to be equal to zero and are indicated as BD (below detection limit) in the results. Complementary information about the limit of detection are presented in Appendix B.1.2.



(a) (b)

Figure 3.18: (a) Calibration curve absorbance/p-nitrophenol (black) obtained by quadratic least squares regression on the calibration data points (black crosses). The experimental data points of the samples for the 7-day differentiation period (red dots), the 14-day differentiation period (blue squares) and the 21-day differentiation period (green diamonds) are reported on the calibration curve as well. The dashed lines represent the limits of detection based on the standard deviation of the blank (light blue) and on the regression (magenta). (b) Zoom on the calibration curve.

Regarding the mean number of cells per sample, for the 7-day and 14-day periods (Fig. 3.19), it is uncertain if the difference between the glass and PPy samples is actually due to a difference in the number of cells attached to the samples or to a difference in the number of adherent cells that were successfully retrieved from the glass and PPy samples. Indeed, for those two periods, it was observed that the cells were more difficult to retrieve from the PPy samples after trypsinization than they were for the adhesion test. In contrast to what was observed during the adhesion test, the cells did not detach easily from the sample and from one another after the trypsinization. In fact, rather than being independently suspended in the trypsin solution, the cells tended to remain attached to one another forming gel-like filaments that were difficult to efficiently retrieve from the sample with a pipette. Therefore, there is a certain amount of uncertainty regarding the resulting DNA quantification and the inferred cell number. In order to overcome this issue, the cell retrieval experimental protocol was slightly modified for the

samples of the 21-day period. Instead of freezing only the cells recovered in the trypsin solution and discarding the samples which were potentially still bearing a part of the cells, the samples were centrifuged with the trypsin solution, rinsed with PBS and then frozen. In this way, cells that would not have been lysed or detached from the sample by the trypsin would still release their DNA and intracellular ALP content in the solution following the freezing and lysing steps. Therefore, for the cell number, the analysis of the results focuses on the 21-day period. For this period, the results of mean cell number per sample are consistent with the ones of cell adhesion tests both in presence or absence of FBS (section 3.1.1), i.e. the mean number of cell is higher for the PPy 40 nm samples than for the PPy 300 nm samples which in turn bears more cells than the glass samples.

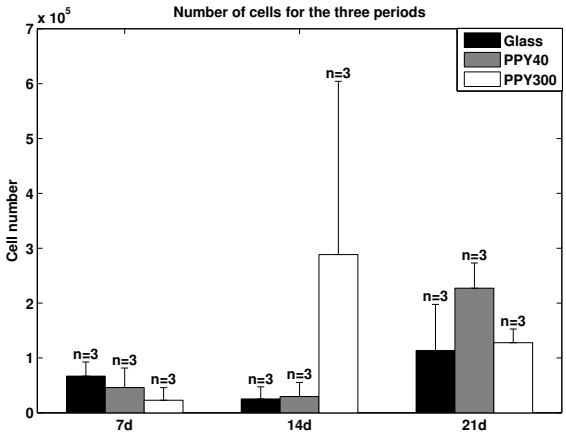


Figure 3.19: Mean cell number per sample type for the three differentiation periods. The error bars correspond to the standard error of the mean (SE). n indicates the number of samples.

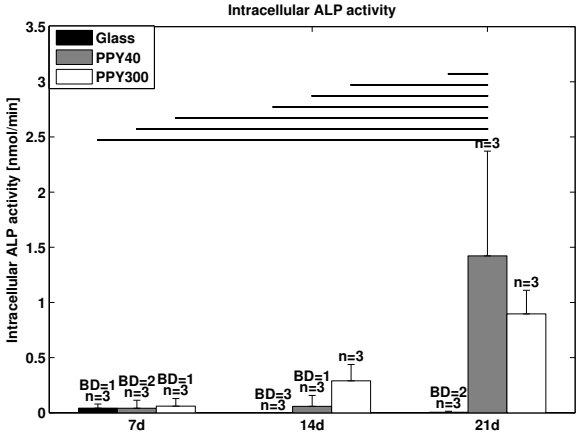


Figure 3.20: Mean intracellular ALP activity per sample for the three differentiation periods. The error bars correspond to the standard error of the mean (SE). A horizontal line above two results indicates a significant difference between those two results (p-value<0.05). n indicates the number of samples, BD indicates the number of samples below the limits of detection.

The intracellular ALP activity per sample is shown in Figure 3.20. However, the measured intracellular ALP activity for the 7 and 14 days-period may not represent the total intracellular ALP activity because of the uncertainties regarding cell retrieval. At 21 days, however, it can be seen that the tendency is the same as for the DNA quantification: best results are obtained for the PPy 40 nm samples, then for the PPy 300 nm samples and finally for the glass samples. Nonetheless, what really matters in order to assess the level of osteogenic differentiation is not the total ALP activity measured per sample, as this may simply result from a higher number of less differentiated cells, but the average ALP activity per cell on the sample as a more differentiated cell yields higher levels of ALP activity [31, 36]. In other words, what really assesses the osteogenic differentiation is the total ALP activity for each sample normalized by the number of cells on this sample. Those results of normalized ALP activity are shown in Figure 3.21.

As the normalization of the intracellular ALP activity by the cell number removes the dependency on the number of cells which were retrieved from each sample, normalized ALP activities (Fig. 3.21) can be compared across the three differentiation periods, despite the change in the cell retrieval protocol after 14 days. Indeed, the quantification of the cell number and the quantification of the intracellular ALP are made on the same cell suspension (section 2.5.1.4). Since the intracellular ALP comes only from the cells that were efficiently retrieved from the samples, normalizing the intracellular ALP by the number of cells that were retrieved from each sample gets rid of the differences that may have come from retrieving more efficiently the cells from some samples than from others. Figure 3.21 shows that after 7 days of culture in osteogenic

medium, normalized ALP intracellular activity is almost null on all three substrates with no significant difference between them. After 14 days, the PPy frameworks display detectable levels of normalized intracellular ALP activity in contrast to glass for which normalized intracellular ALP activity remained below the limit of detection (BD). Nevertheless, no significant difference was detected between the samples of the 7-day and the 14-day period. After 21 days, a significant increase in intracellular ALP activity is observed on both the PPy 300 nm and PPy 40 nm frameworks. Therefore, this suggests that the osteoblastic differentiation on the PPy frameworks started only after at least 14 days of culture in osteogenic medium. Previous studies of MC3T3-E1 cells in the literature report a start of the differentiation stage coupled with an increase in the ALP activity after around ten days of culture in osteogenic medium [31, 35]. The normalized intracellular ALP activity was slightly higher for PPy 300 nm than for PPy 40 nm but this difference is not statistically significant. However, both PPy frameworks yielded significantly higher normalized intracellular activity than bare glass, which shows a value close to zero. This shows that both PPy frameworks efficiently promote the osteoblastic differentiation of MC3T3-E1 cells, in contrast with glass.

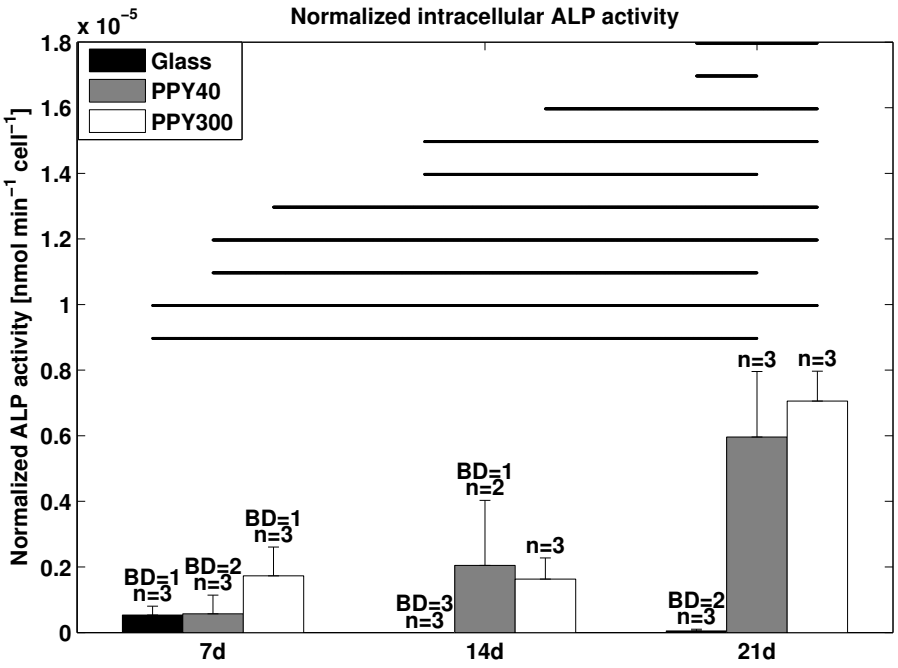
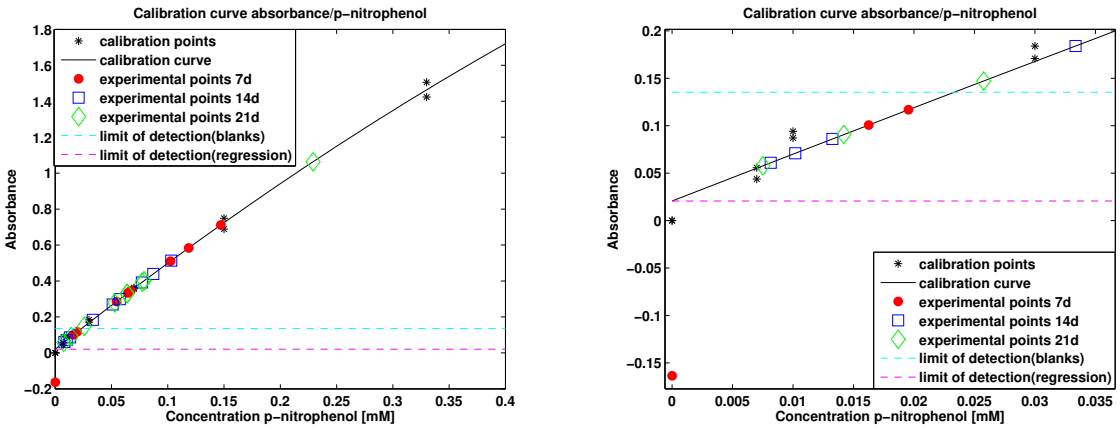


Figure 3.21: Normalized intracellular ALP activity. The error bars correspond to the standard error of the mean (SE). A horizontal line above two results indicates a significant difference between those two results (p-value<0.05). n indicates the number of samples, BD indicates the number of samples below the limits of detection.

3.2.1.2 Extracellular ALP

For the quantification of the extracellular ALP, the experimental readout of the p-nitrophenol concentration of one of the glass sample of the 7-day period falls below the limit of detection of the regression (Fig. 3.22(a)). Furthermore, as can be seen in Figure 3.22(b), some values of absorbances fall below the limit of detection based on the standard deviation of the blanks. Those values correspond to values of absorbance for the glass samples of the three periods. All values falling below those limits of detection were considered as zero p-nitrophenol concentrations and are indicated as BD in the results.



(a) (b)

Figure 3.22: (a) Calibration curve absorbance/p-nitrophenol (black) obtained by quadratic least squares regression on the calibration data points (black crosses). The experimental data points for the 7-day differentiation period (red dots), the 14-day differentiation period (blue squares) and the 21-day differentiation period (green diamonds) are reported on the calibration curve. The dashed lines represent the limits of detection based on the standard deviation of the blank (light blue) and on the regression (magenta) (b) Zoom on the calibration curve.

The data for the number of cells per sample were already presented together with the results of the intracellular ALP (Fig. 3.19). Indeed, the extracellular and the intracellular ALP activities were quantified for the same samples (section 2.5.1). As explained for the intracellular ALP, only the data of the 21-day period are deemed reliable for the number of cells per sample and their analysis has already been presented in section 3.2.1.1.

Regarding the extracellular ALP activity per sample (Fig. 3.23), it must be noticed that the culture media were changed every two or three days. In particular, they were changed two days before the end of each differentiation period. Therefore, the quantification of the extracellular ALP measured only the activity of the ALP excreted by the cells during the last two days of each period. First, it can be noticed that as a whole the extracellular ALP activity of both PPy frameworks is higher than the extracellular activity of glass for all three periods. However, the pattern observed for the extracellular activity seems to be different than for the intracellular ALP activity. Indeed, the extracellular ALP activity for the PPy 300 nm substrate decreased from the 7-day period to the 21-day period in contrast to its intracellular ALP activity (Fig. 3.20). For the three periods, the values obtained for the extracellular ALP activity were higher than those obtained for the intracellular activities. In a study on MC3T3-E1, Seo et al. also obtained higher levels of extracellular ALP activity than intracellular ALP activity after 1 and 5 days but these levels became similar after 10 days of culture. It must be noted, however, that the extracellular and intracellular ALP activities should not be compared in absolute values with the aim to find a meaning in the observed differences since the conditions of accumulation of the ALP during the culture and the conditions of the quantifications were not the same for the extracellular and intracellular ALP. Indeed, extracellular ALP activity was quantified directly in the retrieved medium whereas intracellular ALP activity was quantified from a cell suspension in cell lysis buffer (section 2.5.1.3). However, the fact that the extracellular ALP activity had already reached detectable values after 7 days, while it was only after 14 days for the intracellular ALP, suggests that the quantification of the extracellular ALP activity could potentially already provide information about the level of osteoblastic differentiation after periods of culture too short for the intracellular ALP activity to provide such information. This could also suggest that the onset of differentiation on the PPy frameworks may have occurred earlier than indicated by the intracellular ALP activity (section 3.2.1.1). However, confirming this assumption would require a better understanding of the pattern of extracellular ALP activity during osteoblastic

differentiation. In particular, this would require taking into account the mechanisms of secretion of ALP by the osteoblasts and the existence of a basal level of excreted ALP. *In vitro* studies have indicated that excreted ALP can either stay attached to the cell membrane via an anchor protein or can be released in the medium [91]. Unfortunately, the exact mechanisms of secretion of the ALP and their link with the osteoblastic differentiation seem not to be well understood yet in the literature.

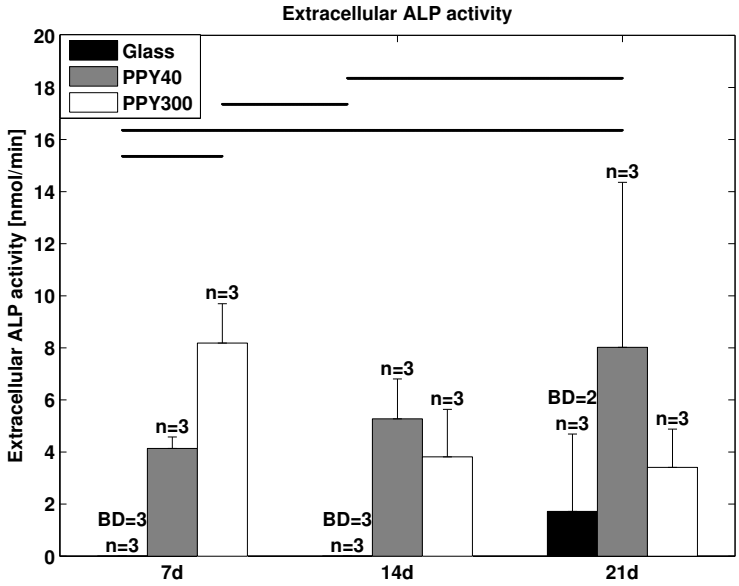
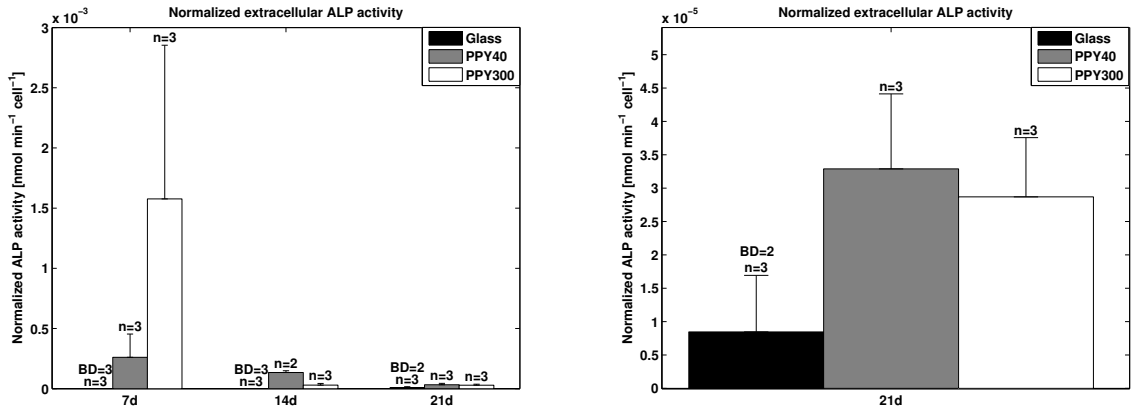


Figure 3.23: Mean extracellular ALP activity per sample for the three differentiation periods. The error bars correspond to the standard error of the mean (SE). A horizontal line above two results indicates a significant difference between those two results (p-value<0.05). n indicates the number of samples, BD indicates the samples below the limits of detection.

In order to assess the level of osteoblastic differentiation, what must be looked at is the ALP activity normalized by the number of cells. However, due to the uncertainty of the DNA quantification results for the 7-day and 14-day periods, only the 21-day period can be analyzed for the normalized extracellular ALP activity. Indeed, the reason for which the normalized ALP concentrations appear so high for the 7-day and 14-day periods (Fig. 3.24) might be due mainly to an underestimation of the cell number during the DNA quantification. This contrasts with the normalized intracellular ALP. Indeed, as explained in section 3.2.1.1, for the intracellular ALP the normalization gets rid of the dependency on the number of cells retrieved from the sample because the intracellular ALP which was quantified came from the retrieved cells only. This is different for the extracellular ALP activity which was quantified from the culture medium and therefore came not only from the cells which were efficiently retrieved but from all the cells which were present on the sample. Therefore, retrieving only a part of the cells, which is believed to be the case especially for the 7-day and the 14-day periods, leads to an overestimation of the normalized extracellular ALP activity. Therefore, looking at the 21-day period only (Fig. 3.24(b)), it can be seen that the extracellular ALP activity is higher for the PPy 40 nm samples, then for the PPy 300 nm samples and, finally, for the glass samples. However, none of these differences are significant due to the relatively high SE.



(a) (b)

Figure 3.24: (a) Normalized extracellular ALP activity. The error bars correspond to the standard error of the mean (SE). n indicates the number of samples, BD indicates the samples below the limits of detection. (b) Zoom on the normalized extracellular ALP activity for the 21-day period.

3.2.2 (HA/COL)-coated PPy frameworks

In order to assess the effect of the biomimetic (HA/COL)-coating on the osteoblastic differentiation of MC3T3-E1 cells, a second ALP assay was carried out on coated and non-coated glass and PPy 300 nm frameworks. The PPy 40 nm framework was not tested as it yielded similar results to the PPy 300 nm framework in the first ALP quantification assay on non-coated substrates (section 3.2.1). Moreover, intracellular and extracellular ALP were quantified only after 14 and 21 days of culture in osteogenic medium as the first ALP quantification assay revealed that, after 7 days, the levels of intracellular ALP activity were mostly below the limit of detection for the glass and PPy frameworks.

3.2.2.1 Intracellular ALP

The calibration curve used to convert the absorbance readouts of the samples into p-nitrophenol concentrations is shown in Figure 3.26. In contrast to the intracellular ALP assay on non-coated samples (section 3.2.1.1), only one readout of the coated glass at 14 days falls below the limit of detection (BD) and is, therefore, considered equal to zero in the analysis of the result. As for the first ALP assay, a fluorometric DNA quantification assay was performed in parallel to the ALP quantification assay in order to determine the cell number on each sample. The calibration curve used to convert the fluorescence intensity into a number of cells is shown in Figure 3.26. It can be noticed that the fluorescence readouts of one non-coated glass and one coated glass at 14 days fall above the saturation limit. The saturation limit was defined as the maximum fluorescence intensity obtained from the calibration points, i.e a fluorescence of $2.45 \cdot 10^4$ corresponding to 250 000 cells. The fluorescence values above this saturation limit were considered to correspond to 250 000 cells and are indicated as AS (above saturation) in the results.

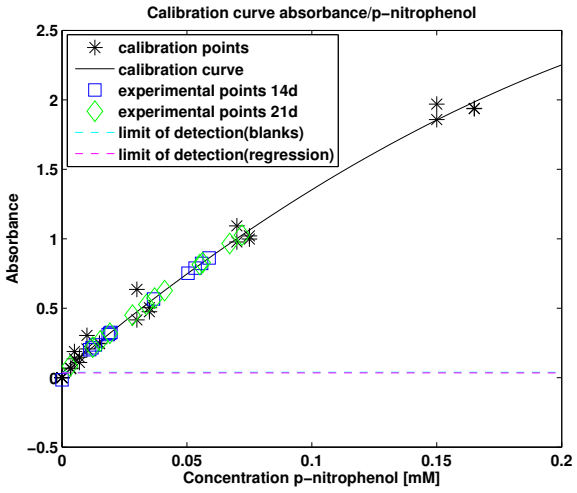


Figure 3.25: Calibration curve absorbance/p-nitrophenol (black) obtained by quadratic least squares regression on the calibration data points (black crosses). The experimental data points for the 14-day differentiation period (blue squares) and the 21-day differentiation period (green diamonds) are reported on the calibration curve. The dashed lines represent the limits of detection based on the standard deviation of the blank (light blue) and on the regression (magenta).

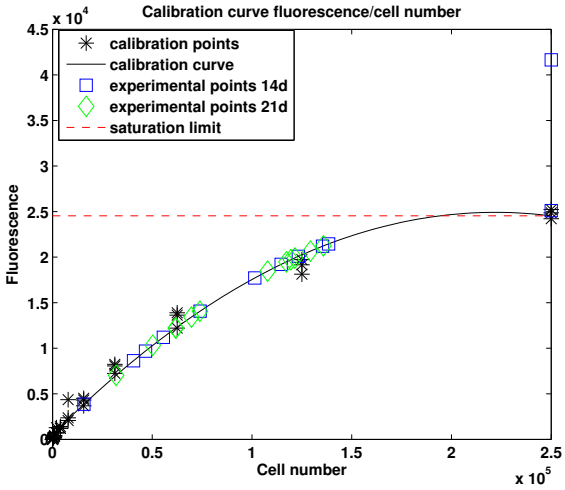


Figure 3.26: Calibration curve fluorescence intensity/cell number obtained by quadratic least square regression on the calibration data points (black crosses). The experimental data points for the 14-day diffferentiation period (blue squares) and the 21-day differentiation period (green diamonds) are reported on the calibration curve. The dashed line represents the limit of saturation of the DNA quantification tests, corresponding to 250 000 cells.

The mean cell number on each substrate after 14 days and 21 days of culture in osteogenic medium is shown in Figure 3.27. In this case, the same protocol for cell retrieval was applied for all samples. As for the 21-day period in the first assay, the samples were centrifuged with the trypsin solution, rinsed with PBS and then frozen. Furthermore, a 1-minute step of sonication was added to the experimental process to ensure a more efficient release of the DNA and intracellular ALP contents. The reported mean cell numbers are thus deemed representative of the total cell number present on each substrate for the two periods. After 14 days, bare glass shows the highest number of cells, followed by coated glass, bare PPy 300 nm and finally coated PPy 300 nm. However, none of these differences are statistically significant and the results for the same sample type are similar for the 14 and 21 days periods. This could indicate that the cells had already reached confluence after 14 days and had already left the proliferation stage to enter the differentiation stage. Indeed, according to the results of Quarles et al. [31], who studied the proliferation and differentiation stages of MC3T3-E1 cells, the beginning of the differentiation stage is coupled with the arrest of cellular proliferation. The transition between the proliferation stage and the differentiation stage for MC3T3-E1 cells was reported to occur after around ten days of culture in osteogenic medium and to be coupled with an arrest of cell proliferation and an increase in ALP activity [31, 35].

Regarding the total intracellular ALP activity per sample (Fig. 3.28), it seems that the coated and non-coated PPy 300 nm frameworks reach higher values than both coated and non-coated glass at 14 days. The two PPy frameworks display similar values after 14 and 21 days. On the other hand, the total intracellular ALP of the non-coated glass increases between 14 and 21 days, while the coated glass remains at a similar level of activity. However, none of these differences were found to be statistically significant. Furthermore, as explained in section 3.2.1.1, to assess correctly the differentiation ability of each substrate, the ALP activity normalized by cell number must be considered rather than the ALP activity per sample on its own, as differences between substrates may result from a difference in cell number.

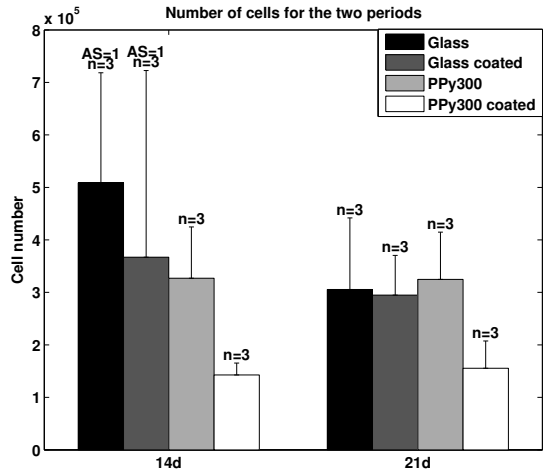


Figure 3.27: Mean cell number per sample type for the two differentiation periods. The error bars correspond to the standard error of the mean (SE). n indicates the number of samples, AS indicates the number of samples above the saturation limit (i.e 250,000 cells).

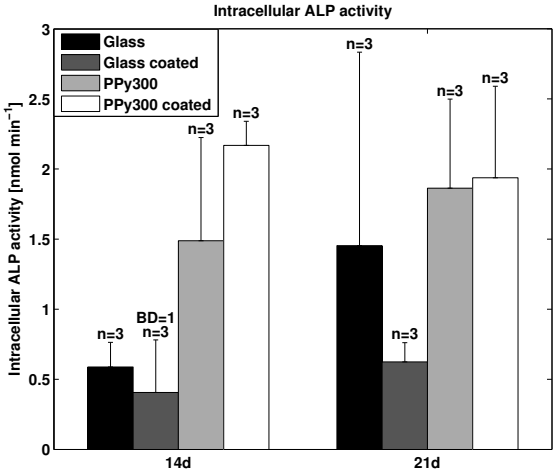


Figure 3.28: Mean intracellular ALP activity per sample for the two differentiation periods. The error bars correspond to the standard error of the mean (SE). n indicates the number of samples, BD indicates the number of samples below the limits of detection.

Normalized intracellular ALP activities for each substrate after 14 and 21 days of culture in osteogenic medium are shown in Figure 3.29. At 14 days, both coated and non-coated glass samples display relatively low levels of normalized intracellular ALP activity, with no significant difference between them. This indicates that, at 14 days, glass did not enhance osteogenic differentiation, as already observed in the first ALP assay (section 3.2.1.1), and that the (HA/COL)-coating did not further enhance this differentiation for the cells cultured on glass. At 14 days, both bare and coated PPy 300 nm substrates display increased ALP activity compared to the glass and coated glass. Furthermore, normalized intracellular ALP activity on coated PPy 300 nm is higher than on bare PPy 300 nm and significantly higher than on bare and coated glass. This indicates that the coated PPy 300 nm framework efficiently enhanced the osteoblastic differentiation of MC3T3-E1 cells after 14 days of culture in osteogenic medium. Therefore, the biomimetic (HA/COL)-coating accelerated the osteoblastic differentiation on the PPy 300 nm, as the onset of intracellular ALP production by the cells occurred earlier (i.e. after 14 days) than it did on the bare PPy framework during the first differentiation test (i.e. after 21 days) (section 3.2.1.1). Between 14 and 21 days, the normalized intracellular ALP activity of the glass and of the coated glass increased slightly but not significantly. As for 14 days, no significant difference was detected between the coated and bare glass samples at 21 days. Therefore, it seems that the (HA/COL)-coating did not improve cell differentiation on the glass substrates. For the non-coated PPy 300 nm framework, the normalized intracellular ALP activity increased slightly between 14 and 21 days to reach a value similar to the one obtained in the first ALP assay (section 3.2.1.1). For the coated PPy 300 nm framework, the normalized intracellular ALP activity after 21 days is similar to the activity observed at 14 days. This indicates that the intracellular ALP activity may have reached a saturation already at 14 days on the coated PPy 300 nm framework. Nonetheless, the normalized intracellular ALP activity on the coated PPy 300 nm is still significantly higher than coated glass, further confirming the conclusion that the (HA/COL)-coated PPy 300 nm framework enhances the osteoblastic differentiation.

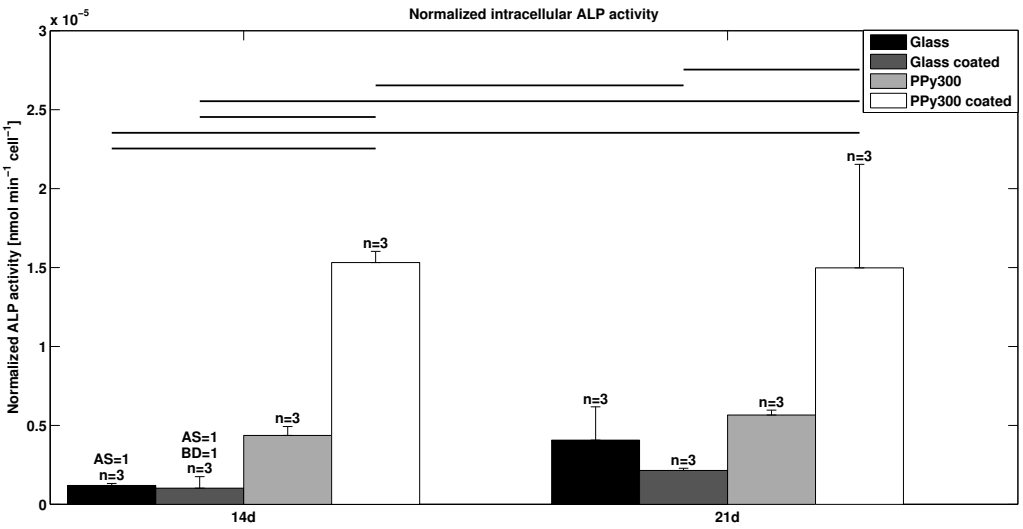


Figure 3.29: Normalized intracellular ALP activity. The error bars correspond to the standard error of the mean (SE). A horizontal line above two results indicates a significant difference between those two results (p-value<0.05). n indicates the number of samples, BD indicates the number of samples below the limits of detection for the ALP activity and AS indicates the number of samples above the saturation limit for the number of cells.

3.2.2.2 Extracellular ALP

For the quantification of the extracellular ALP for the coated samples, in contrast non-coated samples (section 3.2.1.2), all the experimental data points from the absorbance readouts of the p-nitrophenol concentration fall above the detection limits (Fig. 3.30). This quantification assay was realized on the same samples than those used for the quantification of the intracellular ALP (section 3.2.2.1). Therefore, the mean cell numbers per sample are those already presented in Figure 3.27.

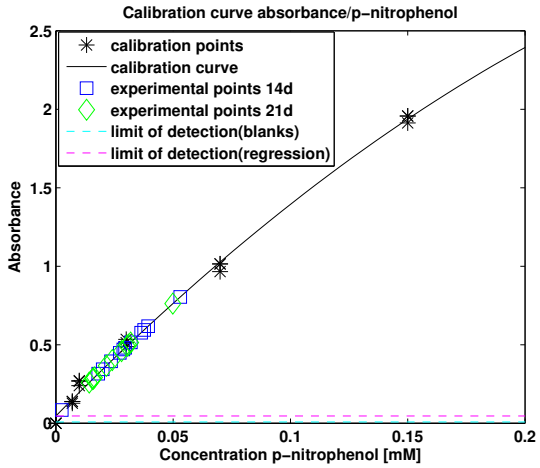


Figure 3.30: Calibration curve absorbance/p-nitrophenol (black) obtained by quadratic least squares regression on the calibration data points (black crosses). The experimental data points for the the 14-day differentiation period (blue squares) and the 21-day differentiation period (green diamonds) are reported on the calibration curve. The dashed lines represent the limits of detection based on the standard deviation of the blank (light blue) and on the regression (magenta).

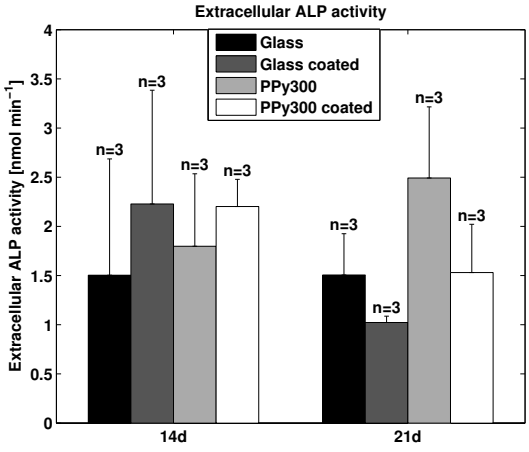


Figure 3.31: Mean extracellular ALP activity per sample for the two differentiation periods. The error bars correspond to the standard error of the mean (SE).

No significant difference appeared in the mean extracellular ALP activity for the different

samples (Fig. 3.31). The results were roughly similar across all samples and across the two periods. However, as for the intracellular ALP (section 3.2.2.1), what really assesses the level of cell differentiation is not the ALP activity but the ALP activity normalized by the number of cells (Fig. 3.32).

In contrast to the differentiation tests on the non-coated samples (section 3.2.1.2), the cells were retrieved from all samples using the same experimental process. For this reason, the normalized extracellular ALP activity of the samples can be compared across the different periods (Fig. 3.32) whereas it was not the case in the previous test (Fig. 3.24). No significant difference is observed across the samples and across the two periods. Nonetheless, regarding the effect of the (HA/COL)-coating, a similar trend than for the normalized intracellular ALP activity is observed, i.e. a beneficial effect of the coating for the PPy 300 nm and no effect on the glass substrate. The only exception to this pattern is the coated glass at 14 days, which displays higher levels of extracellular ALP activity than bare glass. However, the results of this sample are probably less reliable, considering its large SE. Observing a similar pattern for the intracellular and extracellular ALP activities is consistent with the results of Seo et al. who also observed a similar pattern for the intracellular and extracellular activities in a study on MC3T3-E1 cells [92]. Nonetheless, as a whole, the differences between samples are less pronounced for the normalized extracellular ALP than for the normalized intracellular ALP activity. Therefore, it appears that it is more difficult to draw conclusions on the level of differentiation from the normalized extracellular ALP activity for the 14 and 21 days periods. This reinforces the conclusion postulated during the first differentiation test that quantifying extracellular ALP activity might be of interest for the assessment of osteoblastic differentiation for short incubation periods (e.g. 7 days and below) but not for longer periods.

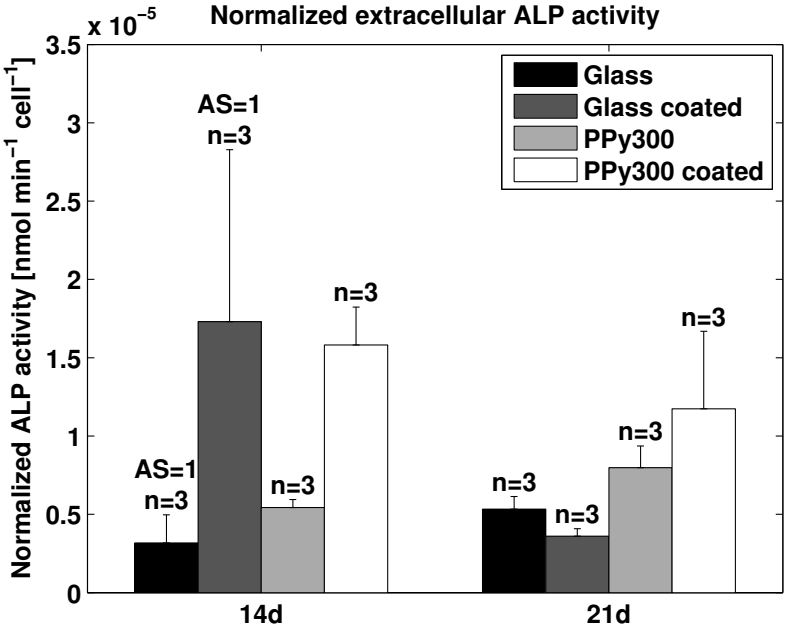


Figure 3.32: Normalized extracellular ALP activity. The error bars correspond to the standard error of the mean (SE).

3.2.3 Summary and discussion of the cell differentiation tests

A first ALP quantification assay performed on bare substrates showed that, after 21 days of culture, both the non-coated PPy 40 nm and the non-coated PPy 300 nm samples exhibited significantly higher levels of normalized intracellular ALP activity compared to bare glass samples. ALP being a marker of osteoblastic differentiation [31,36], this showed that the two PPy nanotube

frameworks significantly enhanced the osteoblastic differentiation of MC3T3-E1 cells. These results are consistent with previous results in the literature which showed that nanowires [60, 64], nanoparticles [65], nanoripples [66] and nanopores [47] increased the osteoblastic differentiation of MC3T3-E1 cells. However, the results of the ALP quantification did not allow to conclude if one of the two nanotube diameters was more beneficial for the osteoblastic differentiation as the two PPy frameworks exhibited similar levels of normalized intracellular ALP activity.

In contrast to the results of the intracellular ALP quantification, the quantification of the activity of extracellular ALP accumulated in the culture medium during the last two days of each differentiation period revealed no significant difference between the samples for the 21-day period. Despite the fact that the ALP is a secreted protein [92, 93], most studies about the differentiation of MC3T3-E1 cells assessed only the intracellular ALP activity, disregarding the extracellular activity [47,64,65,66]. Comparison between the results obtained for the extracellular and intracellular ALP activities showed, however, that whereas no significant difference could be observed between the three sample types for the 7-day and 14-day periods for the intracellular ALP because they all exhibit low or undetectable levels of activity, significant differences in extracellular ALP activities could already be observed between the samples for the 7-day period. Even if no conclusion could be drawn from the results of the normalized extracellular ALP activity for the 7-day and 14-day periods due to high variability in the normalized results, this suggests that the differentiation may start earlier than indicated by the intracellular ALP activity. However, this cannot be confirmed due to a limited understanding of the excretion mechanisms of ALP by osteoblasts. Therefore, this suggests that the onset of ALP excretion might be an interesting parameter to take into account while quantifying the differentiation ability of MC3T3-E1 cells. Furthermore, provided a better understanding of the relation between extracellular ALP and intracellular ALP, quantifying extracellular ALP activity could also allow continuous testing of cell differentiation during culture. Indeed, in contrast to the intracellular ALP, the quantification of the extracellular ALP does not require to stop the cell culture.

A second ALP quantification assay performed on (HA/COL)-coated substrates revealed that the coated PPy 300 nm framework induced significantly higher levels of normalized intracellular ALP activity compared to coated and bare glass after 14 days of culture, and thus earlier than the bare PPy frameworks as shown by the first ALP assay. Therefore, this shows that the coated PPy framework of 300 nm diameter nanotubes significantly enhances the osteoblastic differentiation of MC3T3-E1 cells. These results are consistent with those of Li et al. which showed that (HA/COL)-coatings made by Layer-by-Layer assembly could promote and accelerate osteoblastic differentiation of MC3T3-E1 cells [30]. However, the results of the second differentiation assay did not confirm those of the first assay regarding the enhancing effect of the bare PPy 300 nm nanotubes frameworks on the osteoblastic differentiation. Indeed, even if the normalized intracellular ALP activity remained slightly higher for the bare PPy 300 nm samples than for the bare glass and coated glass samples, this difference was not significant anymore in the second differentiation assay. Nonetheless, this second assay showed that the combination of the nanostructure of the PPy 300 nm framework and the biomimetic (HA/COL)-coating significantly enhanced cell differentiation compared to both the coated and the non-coated glass after 14 days. This increased differentiation ability on the coated PPy nanotubes framework compared to the coated glass is probably explained by a more favorable arrangement of the biomacromolecules of the coating and/or of the adsorbed proteins from the serum on the PPy framework than on the flat glass substrate. Indeed, it has been shown that the spatial arrangement and conformation of cell-binding proteins impacts integrin signaling pathways regulating cell functions such as differentiation [6, 68]. This result is also consistent with the results of Matthews et al. which reported an increased and earlier expression of ALP by rat preosteoblasts on 3D structured collagen substrates than on planar collagen films [72]. Finally, quantification of the extracellular

ALP activity after 14 days and 21 days of incubation in osteogenic medium revealed a similar trend than intracellular ALP quantification. The differences between samples were however no longer significant and less pronounced than for the intracellular ALP activity. These results, with those of the first differentiation assay, suggest that quantifying extracellular activity might be interesting to assess the level of differentiation for short incubation periods (i.e. 7 days or less) but less for longer periods.

In conclusion, whereas the coated glass was more beneficial than coated PPy 300 nm for cell adhesion and proliferation over 24 hours, the (HA/COL)-coated PPy 300 nm frameworks perform significantly better than coated glass in terms of osteoblastic differentiation.

3.3 Summary of the cellular tests

Table 3.3 provides a qualitative summary of the results of the cellular tests that have been performed regarding cell adhesion (assessed from the number of cells after 24 hours), spreading (assessed from epifluorescence microscopy images after 24 hours) and differentiation (assessed from ALP activity after 21 days) on glass, PPy 40 nm and PPy 300 nm substrates, both bare and (HA/COL)-coated.

Table 3.3: Qualitative summary of cell adhesion, cell spreading and cell differentation on the tested substrates. A / indicates that no test was performed on this substrate for the considered cell behavior. The qualitative scale used is $--$, $-$, $+/-$, $+$, $++$ corresponding to very low, low, neutral, high, very high, relatively to the other substrates.

		Adhesion	Spreading	Differentiation
Group A Without FBS	Glass	$--$	$-$	/
	Coated glass	$+/-$	$-$	/
	PPy 40 nm	$+/-$	$+$	/
	Coated PPy 40 nm	$-$	$-$	/
	PPy 300 nm	$-$	$+$	/
	Coated PPy 300 nm	$+/-$	$+$	/
Group B With FBS	Glass	$+/-$	$+$	$-$
	Coated glass	$++$	$+$	$-$
	PPy 40 nm	$++$	$++$	$+$
	Coated PPy 40 nm	$++$	$+$	/
	PPy 300 nm	$+$	$++$	$+$
	Coated PPy 300 nm	$+$	$+$	$++$

The summary table highlights the main trends regarding cell response on the studied substrates. First, cell adhesion and spreading seems to be correlated, as samples with low levels of cell adhesion tend to exhibit less cell spreading and vice-versa. This relation between cell spreading and cell adhesion is often observed, since a cell that does not spread by definition does not adhere well to the substrate. The main factor impacting cell adhesion and spreading was found to be the presence of FBS, as all samples exhibit increased adhesion and spreading in presence of FBS compared to without FBS. As a whole, Table 3.3 also highlights that within each group, the PPy nanotube frameworks, both coated and non-coated, enhance cell adhesion and spreading compared to bare glass, thus showing the positive effect of the nanostructure. In absence of FBS, the effect of the (HA/COL)-coating on cell adhesion and spreading is different for the PPy 40 nm and PPy 300 nm samples. For the PPy 40 nm, the coating has a detrimental effect on cell adhesion and spreading whereas it further improves them for the PPy 300 nm. However, in presence of FBS, the differences between coated and bare PPy are attenuated. Finally, in presence of FBS, the (HA/COL)-coated glass performs as well as the coated and non-coated PPy 40 nm and better than the coated and non-coated PPy 300 nm in terms of cell adhesion.

However, the coated glass does not improve osteoblastic differentiation. In contrast, the PPy frameworks enhanced osteoblastic differentiation compared to both bare and coated glass. In particular, the combination of the PPy nanostructure with the biomimetic (HA/COL)-coating proves the most efficient to promote differentiation.

Conclusion and Perspectives

The objective of this master thesis was to study the ability of nanostructured ECM-like biointerfaces to control cell behavior, in view of applications in tissue engineering and regenerative medicine. The studied biointerfaces consisted in a core self-standing framework of intersected PPy nanotubes coated with hyaluronan and collagen type I by LbL assembly. In previous research works, the elaboration process and the material characterization of these biointerfaces had already been completed by Damien Lefèvre. Therefore, this Master thesis focused on performing cellular tests on the biointerfaces in order to characterize the response of preosteoblastic cells seeded on those biointerfaces in terms of adhesion, proliferation and differentiation with regard to the specific effects of the biomimetic (HA/COL)-coating and of the PPy nanotube frameworks.

For this purpose, cellular tests were performed using preosteoblastic mouse MC3T3-E1 cells. This cell line is frequently used as an osteoblastic model for *in vitro* studies. Cell adhesion and proliferation after 24 hours of culture on the biointerfaces were assessed by means of a fluorometric DNA quantification assay and epifluorescence microscopy. The PPy nanotube frameworks, both coated and non-coated, were shown to enhance cell adhesion compared to bare glass controls. Cells on the PPy frameworks also displayed a more elongated morphology and formed more cell extensions. These results showed that the nanostructure of the PPy nanotube frameworks efficiently promotes cell attachment and spreading. In addition, the adhesion and proliferation tests highlighted an influence of the PPy nanotube diameter on cell attachment. Nanotube frameworks of smaller diameter (40 nm) yielded higher levels of cell adhesion than those of higher diameter (300 nm). The effect of the biomimetic HA/COL coating on the PPy frameworks coating proved different in presence or in absence of fetal bovine serum in the culture medium. In presence of FBS, similar cellular behaviors, in terms of adhesion and spreading, were observed on the coated and non-coated PPy frameworks of the same nanotube diameter. However, the tests performed in absence of FBS revealed an effect of the HA/COL coating on cell adhesion and morphology. Therefore, the presence of FBS was shown to mask the impact of the coating on cell adhesion, probably because of a homogenization of the surfaces of the samples following the adsorption of a mixture of proteins naturally present in the serum. The effect of the biomimetic coating observed in absence of FBS was found to depend on the nanotube diameter of the underlying PPy framework. Comparing the coated and non-coated PPy frameworks of the same nanotube diameter, the biomimetic coating was shown to enhance cell adhesion on the PPy frameworks of 300 nm diameter nanotubes and to slightly decrease it on the frameworks of 40 nm diameter nanotubes. This difference is probably the result of a less favorable spatial arrangement of the cell binding epitopes of the (HA/COL) coating on the nanotubes of 40 nm diameter.

The ability of the biointerfaces to induce differentiation of preosteoblastic MC3T3-E1 cells into mature bone cells was then assessed by a colorimetric quantification of ALP, an early marker of osteoblastic differentiation. Both intracellular and extracellular ALP activities were quantified and normalized by cell number. A first differentiation assay carried out on the non-coated PPy frameworks of 40 nm and 300 nm diameter nanotubes revealed significantly higher normalized intracellular ALP activity on both PPy frameworks than on the bare glass controls after 21 days

of culture in osteogenic medium. This showed that the PPy frameworks of intersected nanotubes significantly enhance the osteoblastic differentiation of MC3T3-E1 cells. However, in contrast to the results of the adhesion tests, intracellular ALP quantification revealed no influence of the nanotube diameter as both PPy frameworks yielded similar levels of differentiation as assessed by normalized intracellular ALP activity. A second differentiation assay was performed on coated PPy 300 nm frameworks in order to assess the effect of the (HA/COL)-coating on the osteoblastic differentiation. It was found that the coated PPy 300 nm framework significantly enhanced the level of osteoblastic differentiation compared to bare glass and coated glass substrates after 14 days of culture as assessed by normalized intracellular ALP activity. Furthermore, as ALP is a secreted protein, extracellular ALP activity was also quantified during the two differentiation assays. It was found that after 7 days of culture the extracellular ALP activity was already high enough to be detectable on the PPy nanotube frameworks which was not the case for the intracellular ALP. However, no significant difference in normalized extracellular ALP activity was found between the substrates after 14 and 21 days of culture. Therefore, these results suggest that quantifying extracellular might be interesting for assessing osteoblastic differentiation over shorter incubation times in osteogenic medium. However, interpreting extracellular ALP activity with regards to osteoblastic differentiation proves difficult without a better understanding of ALP secretion mechanisms.

The present study provided a first evaluation of the suitability of the PPy-based nanostructured ECM-like biointerfaces for bone tissue engineering applications. Adhesion, proliferation and differentiation tests on mouse MC3T3-E1 preosteoblastic cells revealed that the PPy nanotube frameworks, both coated and non-coated, effectively enhance cell attachment and osteoblastic differentiation. Therefore, the studied biointerfaces show a promising potential as a platform for the delivery of signals to cells, particularly in the frame of bone tissue engineering applications. Nonetheless, additional research should be carried out in order to gain a more thorough understanding of cellular behavior on the biointerfaces. Indeed, the differentiation tests performed in this study concerned only ALP, an early marker for osteoblastic differentiation. Therefore, the influence of the PPy nanostructure and of the biomimetic (HA/COL)-coating on osteoblastic differentiation should be further investigated by assessing other osteoblastic markers associated with later stages of differentiation, such as osteocalcin, osteopontin or collagen type I. Levels of expression of those markers could be evaluated, for instance, by RT-PCR. Moreover, even if this study showed the potential of the biointerfaces for bone tissue engineering, potential improvements could be investigated in order to increase their suitability for this targeted application. First, the mechanical strength of the PPy nanotube frameworks should be improved to ease their manipulation and prevent local collapses of the nanotubes. Since PPy is a conductive polymer, the suitability of the biointerfaces to provide electrical stimulation to the seeded cells could be worth investigating, as it has been shown by previous studies that electrical stimulation promotes osteogenesis [57, 94]. Alternatively, to further improve the biocompatibility and osteoconductivity, PPy could be replaced by hydroxyapatite in order to have a nanostructured biointerface made only of components present in native bone tissues.

Bibliography

[1] Jun Deng and Changyou Gao. An introduction to scaffolds, biomaterial surfaces, and stem cells. In Changyou Gao, editor, *Polymeric Biomaterials for Tissue Regeneration. From Surface/Interface Design to 3D Construct*, chapter 1, pages 1–39. Springer, Singapore, 2016.

[2] Daniel Howard, Lee D. Buttery, Kevin M. Shakesheff, and Scott J. Roberts. Tissue engineering: strategies, stem cells and scaffolds. *Journal of Anatomy*, 213:66–72, 2008.

[3] Fa-Ming Chen and Xiaohua Liu. Advancing biomaterials of human origin for tissue engineering. *Progress in Polymer Science*, 53:86–168, 2016.

[4] Gavin Jell, Catherina Minelli, and Molly M. Stevens. Biomaterial-related approaches: Surface structuring. In Ulrich Meyer, Thomas Meyer, Jörg Handschel, and Hans Peter Wiesmann, editors, *Fundamentals of Tissue Engineering and Regenerative Medicine*, chapter 35, pages 469–484. Springer, Berlin, 2009.

[5] Christopher Bettinger, Robert Langer, and Jeffrey T. Borenstein. Engineering substrate topography at the micro- and nanoscale to control cell function. *Angewandte Chemie International Edition*, 48:5406–5415, 2009.

[6] Klaus von der Mark, Jung Park, Sebastian Bauer, and Patrik Schmuki. Nanoscale engineering of biomimetic surfaces: cues from the extracellular matrix. *Cell and Tissue Research*, 339:131–153, 2010.

[7] Guoyou Huang, Fei Li, Xin Zhao, Yufei Ma, Yuhui Li, Min Lin, Guorui Jin, Tian Jian Lu, Guy M. Genin, and Feng Xu. Functional and biomimetic materials for engineering three-dimensional cell microenvironment. *Chemical Reviews*, 117:12764–12850, 2017.

[8] Svenja Hinderer, Shannon Lee Layland, and Katja Schenke-Layland. ECM and ECM-like materials. Biomaterials for applications in regenerative medicine and cancer therapy. *Advanced Drug Delivery Reviews*, 97:260–269, 2016.

[9] Michael Goldberg, Robert Langer, and Xinqiao Jia. Nanostructured materials for applications in drug delivery and tissue engineering. *J. Biomater. Sci. Polymer Edn*, 19(3):241–268, 2007.

[10] Charles R. Martin. Nanomaterials: A membrane-based synthetic approach. *Science*, 266(5193):1961–1966, 1994.

[11] Varvara Gribova, Rachel Auzely-Velty, and Catherine Picart. Polyelectrolyte multilayer assemblies on material surfaces: From cell adhesion to tissue engineering. *Chem. Mater.*, 24:854–869, 2012.

[12] Catherine Picart. Polyelectrolyte multilayer films: From physico-chemical properties to the control of cellular processes. *Current Medicinal Chemistry*, 15:685–697, 2008.

[13] Yiding Liu, James Goebl, and Yadong Yin. Templated synthesis of nanostructured materials. *Chem. Soc. Rev.*, 42:2610–2653, 2013.

[14] Yadian Xie, Duygu Kocaefe, Chunying Chen, and Yasar Kocaefe. Review of research on template methods in preparation of nanomaterials. *Journal of Nanomaterials*, 2016:1–10, 2016.

[15] Huamei M. Shang and Guozhong Cao. Template-based synthesis of nanorods or nanowire arrays. In Bharat Bhushan, editor, *Springer Handbook of Nanotechnology*, chapter 5, pages 161–178. Springer, Berlin, 2010.

[16] Ilkay Sisman. Template-assisted electrochemical synthesis of semiconductor nanowires. In Abbass A. Hashim, editor, *Nanowires. Implementations and Applications*, chapter 3, pages 41–58. Intech, 2011.

[17] Henri Hanot and Etienne Ferain. Industrial applications of ion track technology. *Nuclear Instruments and Methods in Physics Research B*, 267:1019–1022, 2009.

[18] Jannick Duchet, Roger Legras, and Sophie Demoustier-Champagne. Chemical synthesis of polypyrrole: structure-properties relationship. *Synthetic Metals*, 98:113–122, 1998.

[19] Jaime Martin, Marisol Martin-Gonzalez, Jose-Francisco Fernandez, and Olga Caballero-Calero. Ordered three-dimensional interconnected nanoarchitecture in anodic porous alumina. *Nature Communications*, 5:5130, 2014.

[20] Antonio Garcia-Barbera, Mario Culebras, Soledad Roig-Sanchez, Clara M. Gomez, and Andrés Cantarero. Three dimensional PEDOT nanowires network. *Synthetic Metals*, 220:208–212, 2016.

[21] Markus Rauber, Ina Alber, Sven Müller, Reinhard Neumann, Oliver Picht, Christina Roth, Alexander Schökel, Maria Eugenia Toimil-Molares, and Wolfgang Ensinger. Highly-ordered supportless three-dimensional nanowire networks with tunable complexity and interwire connectivity for device integration. *Nanoletters*, 11:2304–2310, 2011.

[22] Luc Piraux, Vlad-Andrei Antohe, Etienne Ferain, and Driss Lahem. Self-supported three-dimensionally interconnected polypyrrole nanotubes and nanowires for highly sensitive chemiresistive gas sensing. *RSC Advances*, 6:21808–21813, 2016.

[23] Joao Borges and Joao F. Mano. Molecular interactions driving the layer-by-layer assembly of multilayers. *Chem. Rev.*, 114:8883–8942, 2014.

[24] Fang-Xing Xiao, Mario Pagliaro, Yi-Jun Xu, and Bin Liu. Layer-by-layer assembly of versatile nanoarchitectures with diverse dimensionality: a new perspective for rational construction of multilayered assemblies. *Chem. Soc. Rev.*, 45:3088–3121, 2016.

[25] P. Bertrand, A. Jonas, A. Laschewsky, and R. Legras. Ultrathin polymer coatings by complexation of polyelectrolytes at interfaces: suitable materials, structure and properties. *Macromol. Rapid. Commun.*, 21:319–348, 2000.

[26] Thomas Boudou, Thomas Crouzier, Kefeng Ren, Guillaume Blin, and Catherine Picart. Multiple functionalities of polyelectrolyte multilayer films: New biomedical applications. *Adv. Mater.*, 22:441–467, 2010.

[27] Anita Shukla and Bethany Almeida. Advances in cellular and tissue engineering using layer-by-layer assembly. *WIREs Nanomed Nanobiotechnol*, 6:411–421, 2014.

[28] Kaiyong Cai, Annett Rechtenbach, Jianyuan Hao, Jorg Bossert, and Klaus D. Jandt. Polysaccharide-protein surface modification of titanium via a layer-by-layer technique: Characterization and cell behaviour aspects. *Biomaterials*, 26:5960–5971, 2005.

[29] Shanshan Guo, Xiaoying Zhu, and Xian Jun Loh. Controlling cell adhesion using layer-by-layer approaches for biomedical applications. *Material Science and Engineering C*, 70:1163–1175, 2017.

[30] Xiaojun Li, Qiaojie Luo, Ying Huang, Xiaodong Li, Feng Zhang, and Shifang Zhao. The responses of preosteoblasts to collagen and hyaluronic acid polyelectrolyte multilayer coating on titanium. *Polym. Adv. Technol.*, 23:756–764, 2012.

[31] L. Darryl Quarles, Daniel A. Yohay, Laura W. Lever, Rashmi Caton, and Richard J. Wenstrup. Distinct proliferative and differentiated stages of murine MC3T3-E1 cells in culture: An in vitro model of osteoblast development. *Journal of Bone and Mineral Research*, 7(6):683–692, 1992.

[32] Hiro-aki Kodama, Yuji Amagai, Hiroko Sudo, Shiro Kasai, and Shigehisa Yamamoto. Establishment of a clonal osteogenic cell line from newborn mouse calvaria. *Japanese Journal of Oral Biology*, 23(4):899–901, 1981.

[33] Hiroko Sudo, Hiro-Ari Kodama, Yuji Amagai, Shigehisa Yamamoto, and Shiro Kasai. In vitro differentiation and calcification in a new clonal osteogenic cell line derived from newborn mouse calvaria. *The Journal of cell biology*, 96(1):191–198, 1983.

[34] Muhammad Dain Yazid, Shahrul Hisham Zainal Ariffin, Sahidan Senafi, Mohamad Abdul Razak, and Rohaya Megat Abdul Wahab. Determination of the differentiation capacities of murines' primary mononucleated cells and MC3T3-E1 cells. *Cancer Cell International*, 10(42):1–12, 2010.

[35] Je-Yong Choi, Byung-Heon Lee, Keun-Bae Song, Rang-Woon Park, In-San Kim, Kun-Young Sohn, Joon-Seung Jo, and Hyun-Mo Ryoo. Expression patterns of bone-related proteins during osteoblastic differentiation in MC3T3-E1 cells. *Journal of cellular biochemistry*, 61(4):609–618, 1996.

[36] Yingying Zhang, He Gong, Yan Sun, Yan Huang, and Yubo Fan. Enhanced osteogenic differentiation of MC3T3-E1 cells on grid-topographic surface and evidence for involvement of YAP mediator. *Journal of Biomedical Materials Research Part A*, 104(5):1143–1152, 2016.

[37] Dian Wang, Kurt Christensen, Kanwal Chawla, Guozhi Xiao, Paul H Krebsbach, and Renny T Franceschi. Isolation and characterization of MC3T3-E1 preosteoblast subclones with distinct in vitro and in vivo differentiation/mineralization potential. *Journal of Bone and Mineral Research*, 14(6):893–903, 1999.

[38] Kristina Kapinas, Catherine B Kessler, and Anne M Delany. miR-29 suppression of osteonectin in osteoblasts: regulation during differentiation and by canonical Wnt signaling. *Journal of cellular biochemistry*, 108(1):216–224, 2009.

[39] Laurence Duplomb, Maylis Dagouassat, Philippe Jourdon, and Dominique Heymann. Concise review: embryonic stem cells: a new tool to study osteoblast and osteoclast differentiation. *Stem cells*, 25(3):544–552, 2007.

[40] Shimpei Kasagi and Wanjun Chen. TGF-beta1 on osteoimmunology and the bone component cells. *Cell & bioscience*, 3(1):4, 2013.

[41] Edel M. Hyland, Michael S. Cosgrove, Henrik Molina, Dongxia Wang, Akhilesh Pandey, Robert J. Cottee, and Jef D. Boeke. Insights into the role of histone H3 and histone H4 core modifiable residues in saccharomyces cerevisiae. *Molecular and cellular biology*, 25(22):10060–10070, 2005.

[42] Natsuno Matsui, Kosuke Nozaki, Kazuhiko Ishihara, Kimihiro Yamashita, and Akiko Nagai. Concentration-dependent effects of fibronectin adsorbed on hydroxyapatite surfaces on osteoblast adhesion. *Materials Science and Engineering: C*, 48:378–383, 2015.

[43] Stavroula Kousteni and John P Bilezikian. The cell biology of parathyroid hormone in osteoblasts. *Current osteoporosis reports*, 6(2):72–76, 2008.

[44] Ujjal K. Singha, Yu Jiang, Shibing Yu, Min Luo, Yi Lu, Jian Zhang, and Guozhi Xiao. Rapamycin inhibits osteoblast proliferation and differentiation in MC3T3-E1 cells and primary mouse bone marrow stromal cells. *Journal of cellular biochemistry*, 103(2):434–446, 2008.

[45] Megan S. Lord, Morten Foss, and Flemming Besenbacher. Influence of nanoscale surface topography on protein adsorption and cellular response. *Nano Today*, 5(1):66–78, 2010.

[46] Shelby A. Skoog, Girish Kumar, Roger J. Narayan, and Peter L. Goering. Biological responses to immobilized microscale and nanoscale surface topographies. *Pharmacology & therapeutics*, 182:33–55, 2018.

[47] Federico Mussano, Tullio Genova, Francesca Giulia Serra, Massimo Carossa, Luca Munaron, and Stefano Carossa. Nano-pore size of alumina affects osteoblastic response. *International journal of molecular sciences*, 19(2):528–539, 2018.

[48] Nathalie K. Guimard, Natalia Gomez, and Christine E. Schmidt. Conducting polymers in biomedical engineering. *Prog. Polym. Sci.*, 32:876–921, 2007.

[49] Xiaohua Yu, Xiaoyan Tang, Shalini V. Gohil, and Cato T. Laurencin. Biomaterials for bone regenerative medicine. *Adv. Healthcare Mater.*, 4(9):1268–1285, 2015.

[50] D.D Ateh, H.A. Navsaria, and P. Vadgama. Polypyrrole-based conducting polyers and interactions with biological tissues. *J. R. Soc. Interface*, 3:741–752, 2006.

[51] Richard Balint, Nigel J. Cassidy, and Sarah H. Cartmell. Conductive polymers: Towards a smart biomaterial for tissue engineering. *Acta Biomateriala*, 10:2341–2353, 2014.

[52] Rajeswari Ravichandran, Subramanian Sundarrajan, Jayarama Reddy Venugopal, Shayanti Mukherjee, and Seeram Ramakrishna. Applications of conducting polymers and their issues in biomedical engineering. *J. R. Soc. Interface*, 7:S559–S579, 2010.

[53] J. Y. Wong, R. Langer, and D. E. Ingber. Electrically conducting polymers can noninvasively control shape and growth of mammalian cells. *Proc. Natl. Acad. Sci. USA*, 91:3201–3204, 1994.

[54] Xioadong Wang, Xioasong Gu, Chunwai Yuan, Shujian Chen, Peiyun Zhang, Tianyi Zhang, Jian Yao, Fen Chen, and Gang Chen. Evaluation of biocompatibility of polypyrrole in vitro and in vivo. *Journal of Biomedical Material Research A*, 68(3):411–422, 2004.

[55] Harold Castano, Edgar A. O'Rear, Peter S. McFetridge, and Vassilios I. Sikavitsas. Polypyrrole thin films formed by admicellar polymerization support the osteogenic differentiation of mesenchymal stem cells. *Macromol. Biosci.*, 4:785–794, 2004.

[56] Chuan Li, Yi-Ting Hsu, and Wei-Wen Hu. The regulation of osteogenesis using electroactive polypyrrole films. *Polymers*, 8:258–269, 2016.

[57] Wei-Wen Hu, Yi-Ting Hsu, Yu-Che Cheng, Chuan Li, Ruoh-Chyu Ruaan, Chih-Cheng Chien, Chih-Ang Chung, and Chia-Wen Tsao. Electrical stimulation to promote osteogenesis using conductive polypyrrole films. *Material Science and Engineering C*, 37:28–36, 2014.

[58] Judith Serra Moreno, Stefania Panero, Stefano Materazzi, Andrea Martinelli, Maria Giovanna Sabbieti, Dimitrios Agas, and Giovanni Materazzi. Polypyrrole-polysaccharide thin films characteristics: Electrosynthesis and biological properties. *Journal of Biomedical Materials Research Part A*, 88(3):832–840, 2009.

[59] E. De Giglio, L. Sabbatini, S. Colucci, and G. Zambonin. Synthesis, analytical characterization, and osteoblast adhesion properties on RGD-grafted polypyrrole coatings on titanium substrates. *Journal of Biomaterials Science, Polymer Edition*, 11(10):1073–1083, 2000.

[60] Yuan He, Shihui Wang, Jing Mu, Lingfeng Dai, Zhong Zhang, Yanan Sun, Wei Shi, and Dongtao Ge. Synthesis of polypyrrole nanowires with positive effect on MC3T3-E1 cell functions through electrical stimulation. *Materials Science and Engineering: C*, 71:43–50, 2017.

[61] Sander Dobbenga, Lidy E. Fratila-Apachitei, and Amir A. Zadpoor. Nanopattern-induced osteogenic differentiation of stem cells: a systematic review. *Acta Biomateriala*, 46:3–14, 2016.

[62] Jung Yul Lim, Andrea D. Dreiss, Zhiyi Zhou, Joshua C. Hansen, Christopher A. Siedlecki, Robert W. Hengstebeck, Juan Cheng, Nicholas Winograd, and Henry J. Donahue. The regulation of integrin-mediated osteoblast focal adhesion and focal adhesion kinase expression by nanoscale topography. *Biomaterials*, 28(10):1787–1797, 2007.

[63] Anand S. Badami, Michelle R. Kreke, M. Shane Thompson, Judy S. Riffle, and Aaron S. Goldstein. Effect of fiber diameter on spreading, proliferation, and differentiation of osteoblastic cells on electrospun poly (lactic acid) substrates. *Biomaterials*, 27(4):596–606, 2006.

[64] Pan-pan Ming, Shui-yi Shao, Jing Qiu, Jie Yang, Ying-juan Yu, Jia-xi Chen, Wen-qing Zhu, and Chun-bo Tang. Superiority of calcium-containing nanowires modified titanium surface compared with SLA titanium surface in biological behavior of osteoblasts: A pilot study. *Applied Surface Science*, 416:790–797, 2017.

[65] Elnaz Tamjid, Arash Simchi, John W.C. Dunlop, Peter Fratzl, Reza Bagheri, and Manouchehr Vossoughi. Tissue growth into three-dimensional composite scaffolds with controlled microfeatures and nanotopographical surfaces. *Journal of Biomedical Materials Research Part A*, 101(10):2796–2807, 2013.

[66] Peng Chen, Masayoshi Miyake, Masahiro Tsukamoto, Yusuke Tsutsumi, and Takao Hanawa. Response of preosteoblasts to titanium with periodic micro/nanometer scale grooves produced by femtosecond laser irradiation. *Journal of Biomedical Materials Research Part A*, 105(12):3456–3464, 2017.

[67] Maria B. Rahmany and Mark Van Dyke. Biomimetic approaches to modulate cellular adhesion in biomaterials. *Acta Biomateriala*, 9(3):5431–5437, 2013.

[68] Klaus von der Mark and Jung Park. Engineering biocompatible implant surfaces. part II: Cellular recognition of biomaterial surfaces: Lessons from cell-matrix interactions. *Progress in Materials Science*, 58:327–381, 2013.

[69] Lilia Araida Hidalgo-Bastida and Sarah H. Cartmell. Mesenchymal stem cells, osteoblasts and extracellular matrix proteins: enhancing cell adhesion and differentiation for bone tissue engineering. *Tissue Engineering Part B*, 16(4):405–412, 2010.

[70] U. Geissler, U. Hempel, C. Wolf, D. Scharnweber, H. Worch, and K.-W. Wenzel. Collagen type I-coating of Ti6A15V promotes adhesion of osteoblasts. *J Biomed Mater Res*, 51(4):752–760, 2000.

[71] Juliette van den Dolder and John A. Jansen. The response of osteoblast-like cells towards collagen type I coating immobilized by p-nitrophenylchloroformate. *J Biomed Mater Res A*, 83A(3):712–719, 2007.

[72] Brya G. Matthews, Dorit Naot, Karen E. Callon, David S. Musson, Rachel Locklin, Philippa A. Hulley, Andrew Grey, and Jillian Cornish. Enhanced osteoblastogenesis in three-dimensional collagen gels. *BoneKEY Reports*, 3:560, 2014.

[73] Hyun Suk Seo, Byung Hoon Kim, and Yeong Mu Ko. Fabrication of anodized titanium with immobilization of hyaluronic acid to improve biological performance. *Progress in Organic Coatings*, 69(1):38–44, 2010.

[74] Sankalp Agarwal, Mathieu Riffault, David Hoey, Brendan Duffy, James Curtin, and Swarna Jaiswal. Biomimetic hyaluronic acid-lysozyme composite coating on AZ31 Mg alloy with combined antibacterial and osteoinductive activities. *ACS Biomaterials Science & Engineering*, 3(12):3244–3253, 2017.

[75] Smitha Mathews, Ramesh Bhonde, Pawan Kumar Gupta, and Satish Totey. A novel tripolymer coating demonstrating the synergistic effect of chitosan, collagen type 1 and hyaluronic acid on osteogenic differentiation of human bone marrow derived mesenchymal stem cells. *Biochemical and biophysical research communications*, 414(1):270–276, 2011.

[76] Poh-Hui Chua, Koon-Gee Neoh, En-Tang Kang, and Wilson Wang. Surface functionalization of titanium with hyaluronic acid/chitosan polyelectrolyte multilayers and RGD for promoting osteoblast functions and inhibiting bacterial adhesion. *Biomaterials*, 29(10):1412–1421, 2008.

[77] Jun Zhang, Bernard Senger, Dominique Vautier, Catherine Picart, Pierre Schaaf, Jean-Claude Voegel, and Philippe Lavalle. Natural polyelectrolyte films based on layer-by-layer deposition of collagen and hyaluronic acid. *Biomaterials*, 26:3353–3361, 2005.

[78] Fabien Gaudière, Sandrine Morin-Grognet, Laurent Bidault, Pierre Lembré, Emmanuel Pauthe, Jean-Pierre Vannier, Hassan Atmani, Guy Ladam, and Béatrice Labat. Genipin-cross-linked layer-by-layer assemblies : Biocompatible microenvironments to direct bone cell fate. *Biomacromolecules*, 15(5):1602–1611, 2014.

[79] Thermo Scientific. Crosslinking reagent technical handbook. `https://tools.thermofisher.com/content/sfs/brochures/1602163-Crosslinking-Reagents-Handbook.pdf`, 2012. Accessed: 2018-04-25.

[80] Molecular Probes. CyQUANT cell proliferation assay kit. `https://www.thermofisher.com/order/catalog/product/C7026`, 2006. Accessed: 2018-04-27.

[81] ThermoFisher Scientific. CyQUANT cell proliferation assays. `https://www.thermofisher.com/be/en/home/brands/molecular-probes/key-molecular-probes-products/cyquant-cell-proliferation-assays.html#cyquant`. Accessed: 2018-04-27.

[82] Rob L. Dean. Kinetic studies with alkaline phosphatase in the presence and absence of inhibitors and divalent cations. *Biochemistry and molecular biology education*, 30(6):401–407, 2002.

[83] G-Bioscience. Phosphatase assay. `https://www.gbiosciences.com/Bioassays/Phosphatase-Assay`. Accessed: 2018-05-01.

[84] M. J. Cooke, S.R. Phillips, D. S.H. Shah, D. Athey, J.H. Lakey, and S.A. Przyborski. Enhanced cell attachment using a novel cell culture surface presenting functional domains from extracellular matrix proteins. *Cytotechnology*, 56:71–79, 2008.

[85] G. Gronowicz and M.B. McCarthy. Response of human osteoblasts to implant materials: Integrin-mediated adhesion. *Journal of Orthopaedic Research*, 14:878–887, 1996.

[86] Deepak M. Kalaskar, Sophie Demoustier-Champagne, and Christine C. Dupont-Gillain. Interaction of preosteoblasts with surface-immobilized collagen-based nanotubes. *Colloids and Surfaces B: Biointerfaces*, 111:134–141, 2013.

[87] Jennie P. Mather and Penelope E. Roberts. *Introduction to Cell and Tissue Culture: Theory and Technique*. Introductory Cell and Molecular Biology Techniques. Springer US, 2007. `https://books.google.be/books?id=Cla-N2x4cRQC`. Accessed: 2018-05-26.

[88] J.A. Ryan. Evolution of cell culture surfaces. *BioFiles*, 3(8):71–79, 2008. `https://www.sigmaaldrich.com/technical-documents/articles/biofiles/evolution-of-cell.html`. Accessed: 2018-05-26.

[89] Damien Lefèvre. PhD thesis meeting powerpoint presentation, 2017.

[90] Colin A. Scotchford. Cell response to surface chemistry in biomaterials. In Lucy Di Silvio, editor, *Cellular response to biomaterials*, chapter 18, pages 462–478. Elsevier Science, 2008.

[91] D.J. Anh, H.P. Dimai, S.L. Hall, and J.R. Farley. Skeletal alkaline phosphatase activity is primarily released from human osteoblasts in an insoluble form, and the net release is inhibited by calcium and skeletal growth factors. *Calcified Tissue International*, 62:332–340, 1998.

[92] Hyun-Ju Seo, Young-Eun Cho, Taewan Kim, Hong-In Shin, and In-Sook Kwun. Zinc may increase bone formation through stimulating cell proliferation, alkaline phosphatase activity and collagen synthesis in osteoblastic MC3T3-E1 cells. *Nutrition research and practice*, 4(5):356–361, 2010.

[93] Jiancheng Yang, Jian Zhang, Chong Ding, Dandan Dong, and Peng Shang. Regulation of osteoblast differentiation and iron content in MC3T3-E1 cells by static magnetic field with different intensities. *Biological trace element research*, 184(1):214–225, 2018.

[94] Zongguang Liu, Lingqing Dong, Liming Wang, Xiaozhao Wang, Kui Cheng, Zhongkuan Luo, and Wenjian Weng. Mediation of cellular osteogenic differentiation through daily stimulation time based on polypyrrole planar electrodes. *Scientific Reports*, 7:17926, 2017.

[95] Gary L. Long and James D. Winefordner. Limit of detection. A closer look at the IUPAC definition. *Analytical Chemistry*, 55(7):712A–724A, 1983.

[96] David A. Armbruster and Terry Pry. Limit of blank, limit of detection and limit of quantitation. *The Clinical Biochemist Reviews*, 29(Suppl 1):S49–S52, 2008.

Appendix A

Complementary information on the cell adhesion and proliferation tests

A.1 Calibration curves of the DNA quantification assay

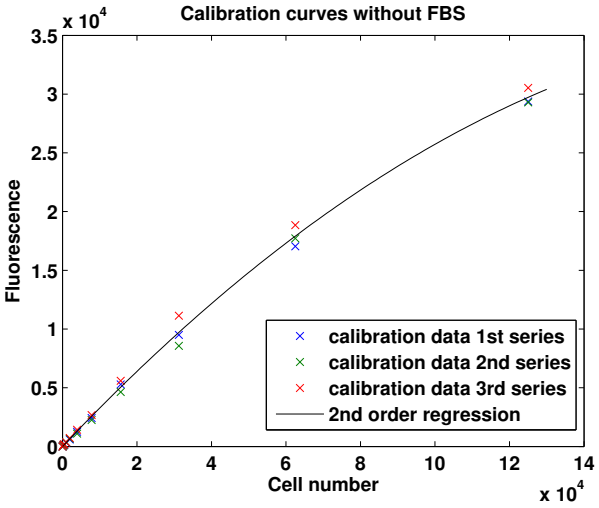


Figure A.1: Fluorescence/cell number calibration curve (black) describing the relationship between the cell number in the cellular suspension and the readout fluorescence in absence of FBS. The curve is obtained by performing a quadratic least squares regression on the experimental calibration data series obtained from reference cellular suspension of known cell density.

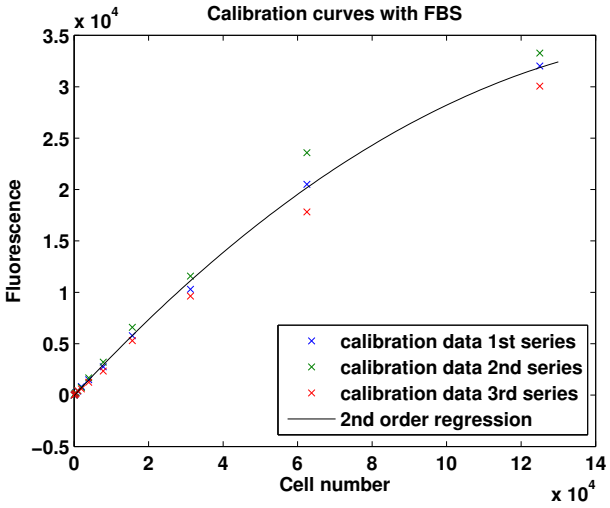


Figure A.2: Fluorescence/cell number calibration curve (black) describing the relationship between the cell number in the cellular suspension and the readout fluorescence in presence of FBS. The curve is obtained by performing a quadratic least squares regression on the experimental calibration data series obtained from reference cellular suspension of known cell density.

A.2 Detailed results of DNA quantification assay

Table A.1: Number of adherent cells per sample determined by the DNA quantification assay after 24h of culture on the samples.

Initial seeding density = $5 \cdot 10^5$ cells/sample				
	Group A Without FBS		Group B With FBS	
samples	Mean cell number	SEM	Mean cell number	SEM
Glass	$0.54 \cdot 10^4$	$0.1 \cdot 10^4$	$1.75 \cdot 10^4$	$1.07 \cdot 10^4$
Coated glass	$1.58 \cdot 10^4$	$0.45 \cdot 10^4$	$5.08 \cdot 10^4$	$0.84 \cdot 10^4$
PPy 40nm	$1.07 \cdot 10^4$	$0.11 \cdot 10^4$	$6.38 \cdot 10^4$	$1.62 \cdot 10^4$
Coated PPy 40nm	$0.73 \cdot 10^4$	$0.13 \cdot 10^4$	$5.25 \cdot 10^4$	$1.65 \cdot 10^4$
PPy 300nm	$0.83 \cdot 10^4$	$0.19 \cdot 10^4$	$3.17 \cdot 10^4$	$0.46 \cdot 10^4$
Coated PPy 300nm	$1.47 \cdot 10^4$	$0.08 \cdot 10^4$	$3.02 \cdot 10^4$	$0.06 \cdot 10^4$

A.3 SEM image artifacts

In this section, examples of artifacts resulting from the fixation, immunostaining and dehydration treatments (sections 2.4.4 and 2.4.5) observed by SEM are presented for the PPy 40 nm and PPy 40 nm +$(HA/COL)_6$ samples with MC3T3-E1 cells after 24 hours of culture in presence of FBS.

A.3.1 Non coated PPy 40 nm

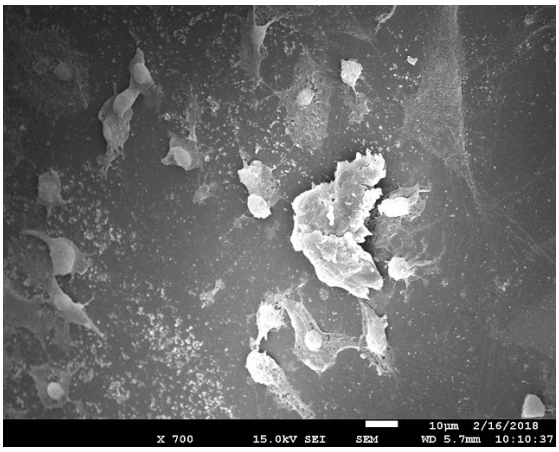


Figure A.3: SEM image of MC3T3-E1 cells on the PPy 40 nm sample from group B (with FSB). Due to the pre-imaging treatments (fixation, immunostaining and dehydration) cell membranes appear almost merged with a crust recovering the surface of the sample. As a result, the contrast between the cells and their substrate is weak, with only the cells nuclei standing out.

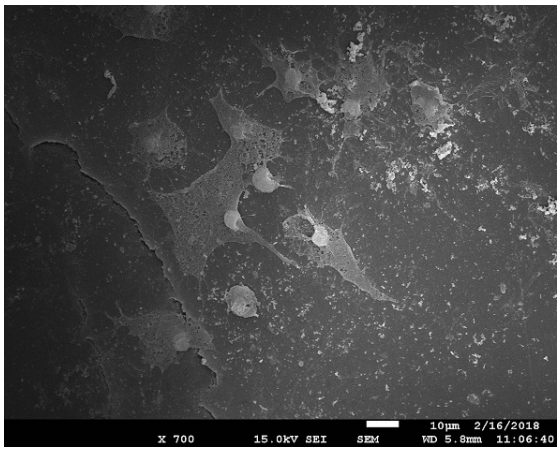
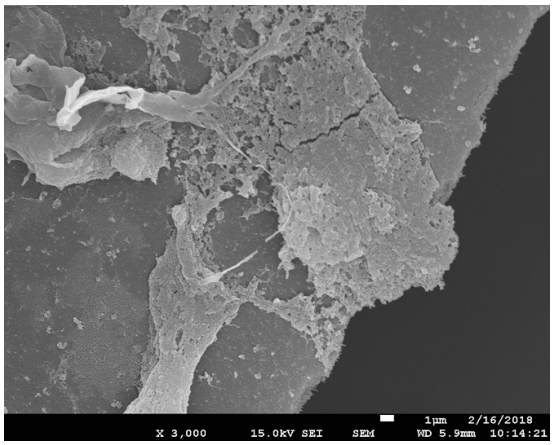
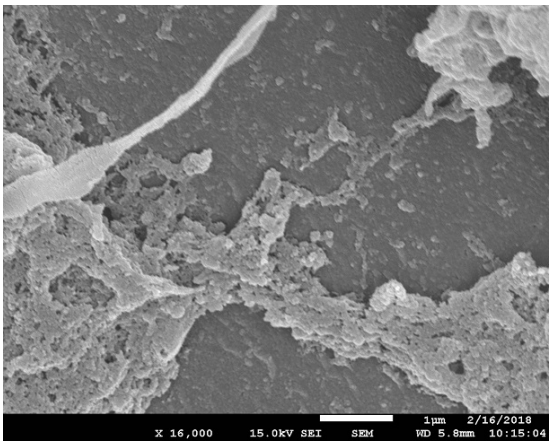


Figure A.4: SEM image of MC3T3-E1 cells on the PPy 40 nm sample from group B (with FSB). Due to the pre-imaging treatments (fixation, immunostaining and dehydration) cell membranes appear almost merged with a crust recovering the surface of the sample. As a result, the contrast between the cells and the surface is weak, with only the cells nuclei standing out. Some cell membranes also appear burst as a result of the permeabilization with Triton X-100 prior to immunostaining.



(a)



(b)

Figure A.5: SEM image of the remnants of MC3T3-E1 cells on the PPy 40 nm sample of group B (with FBS). (a) The pre-imaging treatments damaged the cell membranes. As illustrated here, cells membrane observed by SEM appear rough and burst. (b) Closer view of the cell membrane, showing the particular roughness resulting from the pre-imaging treatments.

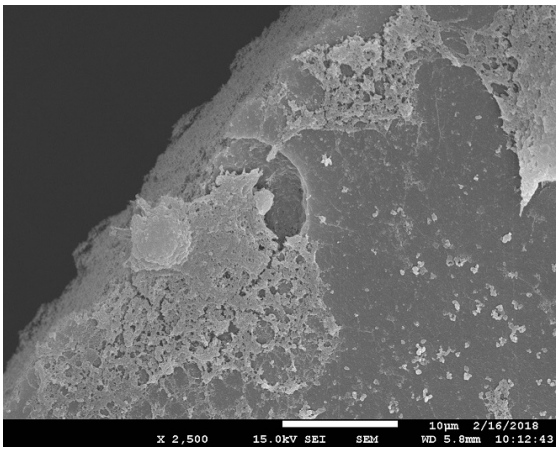


Figure A.6: SEM image of the remnants of MC3T3-E1 cells at the edge of the PPy 40 nm sample of group B (with FBS). Cell membranes display the particular rough and burst aspect resulting from the pre-imaging treatment. The damaged cell membrane is also shown to merge with the crust covering the top surface of the sample. The nanotube framework can be seen on the lateral face of the sample, which is free of the crust.

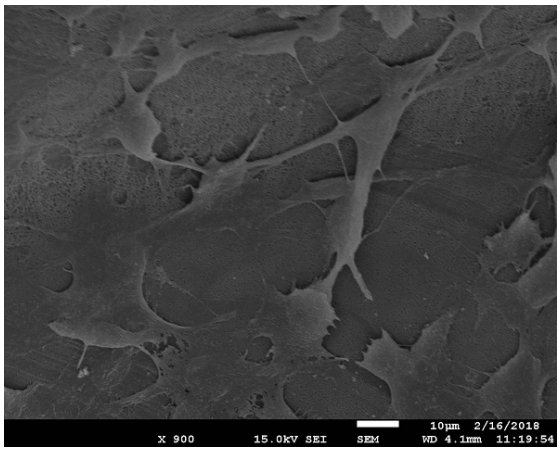


Figure A.7: SEM image of MC3T3-E1 cells at the edge of the PPy 40 nm sample of group B (with FBS). Cells were shown to be reticulated in some areas of the sample and appear to merge with the crust covering the top surface of the sample. The crust and this reticulation are probably the result of a fusion of the organic matter present on the surface of the sample caused by the dehydration treatment. In the top part of the image, the crust is shown to be interrupted, thus revealing the PPy nanotube framework underneath.

A.3.2 Coated PPy 40 nm

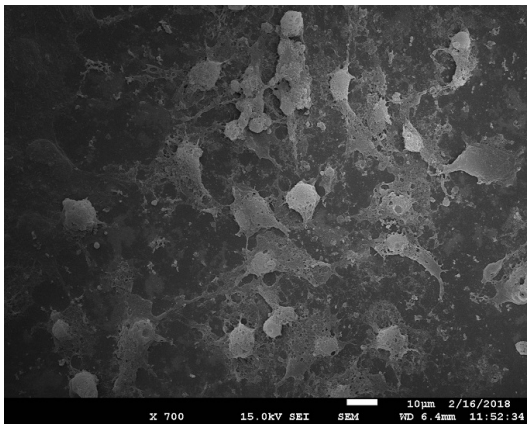


Figure A.8: SEM image of MC3T3-E1 cells on the PPy 40 nm +$(HA/COL)_6$ sample from group B (with FSB). As on the non-coated sample, cells membranes tend to merge with a crust covering the surface, resulting in a weak contrast. They also present the particular rough aspect observed on the non-coated sample.

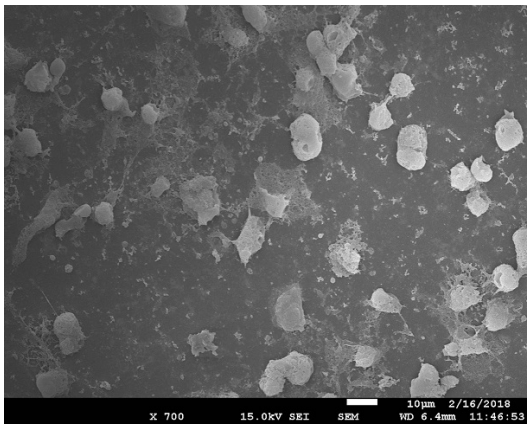


Figure A.9: SEM image of the remnants MC3T3-E1 cells on the PPy 40 nm +$(HA/COL)_6$ sample from group B (with FSB). As a result of the pre-imaging treatments, cell membranes tend to be merged with the surface, leaving only their nuclei observable.

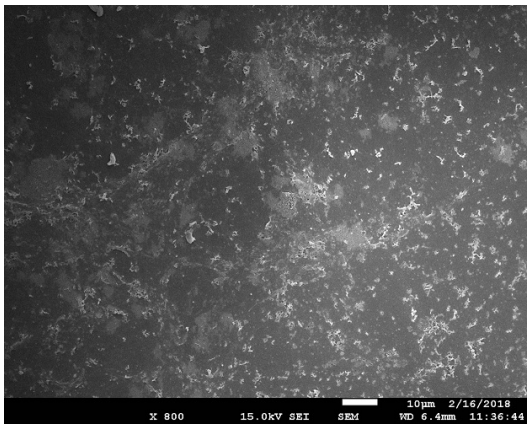


Figure A.10: SEM image of the remnants MC3T3-E1 cells on the PPy 40 nm +$(HA/COL)_6$ sample from group B (with FSB). In some parts of the sample, fusion of the cells with the crust covering the surface is almost complete, leaving only remnants of their membrane (recognizable at their particular rough aspect) observable. For this reason, cell observation on the coated sample proved more difficult than on the non-coated sample.

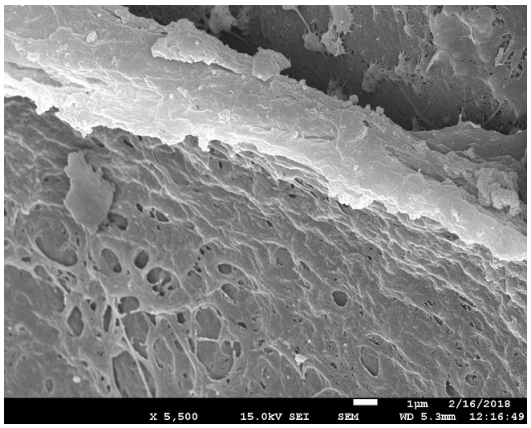
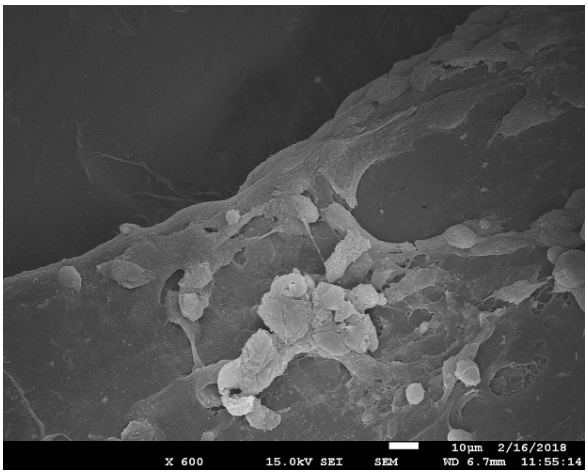
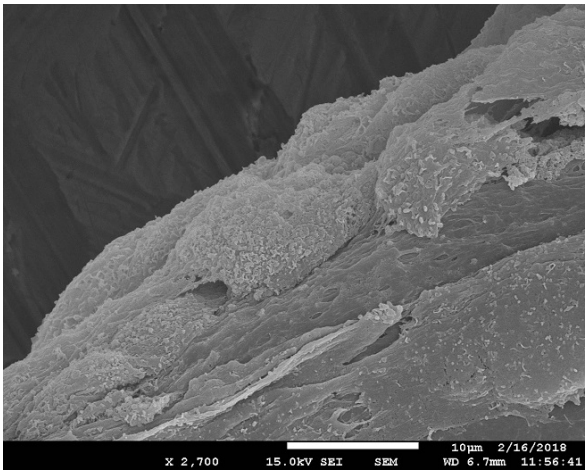


Figure A.11: SEM image of the crust covering the PPy 40 nm + $(HA/COL)_6$ sample from group B (with FBS). The surface of the sample is covered by a crust preventing the observation of the underlying nanotube framework. Cells and fibers can be seen reticulated with this crust. The reticulated fibers are the result of a modification of the (HA/COL) coating morphology caused by the dehydration treatment.



(a)



(b)

Figure A.12: SEM image of MC3T3-E1 cells on the PPy 40 nm +$(HA/COL)_6$ sample from group B (with FSB). As observed on the non-coated sample, cells were shown to be reticulated in some areas of the sample and appear to merge with the crust covering the top surface of the sample.

Appendix B

Complementary information on the cell differentiation tests

B.1 Non-coated PPy frameworks

B.1.1 Calibration curve for the DNA quantification

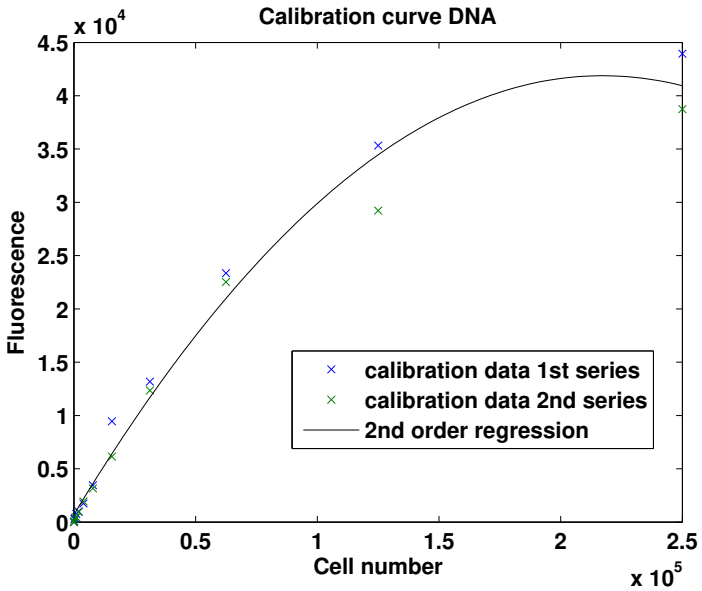


Figure B.1: Fluorescence/cell number calibration curve (black) describing the relationship between the cell number in the cellular suspension and the readout fluorescence. The curve is obtained by performing a quadratic least squares regression on the experimental calibration data series obtained from reference cellular suspension of known cell density.

B.1.2 Information about the calibration curves for the intracellular ALP quantification

For both the intracellular and extracellular ALP quantifications, absorbance readouts for each sample were performed as described in section 2.5.1.3. To those absorbance readouts, the absorbance value of the blanks was subtracted so that the resulting difference in absorbance was due to the concentration of p-nitrophenol. The relationship between the absorbance values and the p-nitrophenol concentration was determined based on the elaborated calibration curves (section 2.5.1.3). Two limits of detection were computed for this quantification of the ALP concentration: the limit of detection based on the blanks and the limit of detection based on the second order regression of the calibration values. The limit of detection based on the blanks was

computed as three times the standard deviation of the absorbance values of the blanks. This limit of detection is such that an absorbance value equal to this limit has only 0.13% chance to be due to random noise instead of being due to an actual p-nitrophenol concentration [95, 96]. The second limit of detection that was computed is based on the second order regression of the calibration data point. This second limit of detection is equal to the absorbance value corresponding to a zero p-nitrophenol concentration according to the second order regression. Absorbance values below those limits were considered as corresponding to a zero p-nitrophenol concentration. Tables B.1 and B.2 show the number of samples below those two detection limits.

Table B.1: Number of samples below the detection limits for the quantification of the intracellular ALP

Limit of detection of the blanks: absorbance=2.9999e-04		
Limit of detection of the regression: absorbance=0.0412		
First non-zero calibration data point: absorbance=0.1225		
Sample	Number of samples below the limit of detection of the blanks	Number of samples below the limit of detection of the regression
Glass 7D	0	1
PPy 40nm 7D	0	2
PPy 300nm 7D	1	1
Glass 14D	0	3
PPy 40nm 14D	0	1
PPy 300nm 14D	0	0
Glass 21D	0	2
PPy 40nm 21D	0	0
PPy 300nm 21D	0	0

Table B.2: Number of samples below the detection limits for the quantification of the extracellular ALP

Limit of detection of the blanks: absorbance= 0.1353		
Limit of detection of the regression: absorbance=0.0207		
First non-zero calibration data point: absorbance=0.0438		
Sample	Number of samples below the limit of detection of the blanks	Number of samples below the limit of detection of the regression
Glass 7D	3	1
PPy 40nm 7D	0	0
PPy 300nm 7D	0	0
Glass 14D	3	0
PPy 40nm 14D	0	0
PPy 300nm 14D	0	0
Glass 21D	2	0
PPy 40nm 21D	0	0
PPy 300nm 21D	0	0

Rue Archimède, 1 bte L6.11.01, 1348 Louvain-la-Neuve **www.uclouvain.be/epl**

